Iowa State University
Digital Repository

Retrospective Theses and Dissertations

Iowa State University Capstones, Theses and Dissertations

1982

Effect of nonuniformity in temperature distribution on the performance of a stripe-geometry double-heterostructure laser

Gi Young Lee
Iowa State University

Follow this and additional works at: https://lib.dr.iastate.edu/rtd

Part of the Electrical and Electronics Commons

Recommended Citation
Lee, Gi Young, "Effect of nonuniformity in temperature distribution on the performance of a stripe-geometry double-heterostructure laser " (1982). *Retrospective Theses and Dissertations*. 7051.
https://lib.dr.iastate.edu/rtd/7051

This Dissertation is brought to you for free and open access by the Iowa State University Capstones, Theses and Dissertations at Iowa State University Digital Repository. It has been accepted for inclusion in Retrospective Theses and Dissertations by an authorized administrator of Iowa State University Digital Repository. For more information, please contact digirep@iastate.edu.

المنارة للاستشارات

www.manaraa.com

INFORMATION TO USERS

This was produced from a copy of a document sent to us for microfilming. While the most advanced technological means to photograph and reproduce this document have been used, the quality is heavily dependent upon the quality of the material submitted.

The following explanation of techniques is provided to help you understand markings or notations which may appear on this reproduction.

1. The sign or "target" for pages apparently lacking from the document photographed is "Missing Page(s)". If it was possible to obtain the missing page(s) or section, they are spliced into the film along with adjacent pages. This may have necessitated cutting through an image and duplicating adjacent pages to assure you of complete continuity.

2. When an image on the film is obliterated with a round black mark it is an indication that the film inspector noticed either blurred copy because of movement during exposure, or duplicate copy. Unless we meant to delete copyrighted materials that should not have been filmed, you will find a good image of the page in the adjacent frame. If copyrighted materials were deleted you will find a target note listing the pages in the adjacent frame.

3. When a map, drawing or chart, etc., is part of the material being photographed the photographer has followed a definite method in "sectioning" the material. It is customary to begin filming at the upper left hand corner of a large sheet and to continue from left to right in equal sections with small overlaps. If necessary, sectioning is continued again—beginning below the first row and continuing on until complete.

4. For any illustrations that cannot be reproduced satisfactorily by xerography, photographic prints can be purchased at additional cost and tipped into your xerographic copy. Requests can be made to our Dissertations Customer Services Department.

5. Some pages in any document may have indistinct print. In all cases we have filmed the best available copy.

University Microfilms International
300 N. ZEEB RD., ANN ARBOR, MI 48106

8221199

Lee, Gi Young

EFFECT OF NONUNIFORMITY IN TEMPERATURE DISTRIBUTION ON THE PERFORMANCE OF A STRIPE-GEOMETRY DOUBLE-HETEROSTRUCTURE LASER

Iowa State University PH.D. 1982

University
Microfilms
International 300 N. Zeeb Road, Ann Arbor, MI 48106

Effect of nonuniformity in temperature distribution on the performance of a stripe-geometry double-heterostructure laser

by

Gi Young Lee

A Dissertation Submitted to the
Graduate Faculty in Partial Fulfillment of the
Requirements for the Degree of
DOCTOR OF PHILOSOPHY
Major: Electrical Engineering

Approved:

Signature was redacted for privacy.

In Charge of Major Work

Signature was redacted for privacy.

For the Major Department

Signature was redacted for privacy.

For the Graduate College

Iowa State University
Ames, Iowa

1982

TABLE OF CONTENTS

		Page
I.	INTRODUCTION	1
	A. Review of the Semiconductor Injection Laser	3
	1. Principle of operation	3
	2. Structure of the device	7
	3. Previous work on thermal property of the device	15
	B. Statement of the Problem	19
II.	THE MODEL	24
	A. Lateral Current Spreading and Electron Diffusion	24
	1. Lateral current spreading	24
	2. Electron out-diffusion in the active layer	30
	B. Thermal Distribution in the Laser	35
	1. Coordinate system and assumptions	35
	2. Solution of the heat equation	38
	3. Determination of the Fourier coefficients	39
	4. Thermal resistance and temperature distribution	44
	C. Wave Equation in the Laser Cavity	49
	1. Dielectric constant variation in the lateral direction	50
	2. Parabolic approximation	53
	3. Effective index approximation	54
	4. Solution of the wave equation	64
	5. Mode gain, near- and far-field pattern	66

Page

III. RESULTS AND DISCUSSION 72

A. Junction Temperature Effects on the Performance of the Laser 72

1. Effect on waveguiding 72

2. Effect on threshold current 86

3. Effect on spectrum shift 93

4. Limitation of the model 97

B. Reduction of Junction Temperature Rise 98

1. Effect of each layer thickness 98

2. Effect of strip width and laser cavity length 104

3. Other thermal design considerations 109

IV. CONCLUDING REMARKS 111

A. Suggestion for Further Study 112

V. REFERENCES 114

VI. ACKNOWLEDGMENTS 120

VII. APPENDIX 121

A. Solution for Current Spreading 121

B. Ambipolar Diffusion Constant 122

C. Hermite-Gaussian Solution 123

I. INTRODUCTION

One of the major achievements in modern data transmission has been the development of fiber optical communication systems which transmit information through encoded light beams propagated in hair-thin glass fibers [1]. Essentially this high data capacity technique has been made possible by two separate technological breakthroughs.

The first was the invention, in the early 1970s, of low attenuation optical fibers below 5 dB/km. Recent laboratory results have yielded signal attenuation as low as 0.2 dB/km at 1.55 μm in single-mode fibers. Systems operating at 1.3 μm have transmitted data at 140 Mbit/sec for up to 30 km without repeaters [2].

The second breakthrough was the development of semiconductor light sources including light emitting diodes (LEDs) and injection lasers. Semiconductor injection lasers are ideal for many optical fiber systems, especially for high capacity data channels or long distance transmission applications, because their narrower spectral width reduces the effect of the intrinsic chromatic dispersion in the fiber so that the data channel capacity can be enhanced. Also, these lasers efficiently couple more power into the fibers because of their high-radiance emission patterns.

In many environmental temperature ranges, however, semiconductor lasers are not applicable because their emission threshold is intrinsically temperature sensitive [3-6]. To compensate for the temperature effect, it is necessary to employ circuitry which automatically adjusts

the driving current. At present, this leads to a shorter device lifetime at higher operating temperature [7,8].

Another important aspect of laser thermal properties is an internal temperature rise caused by the diode driving current. The nature of heat dissipation in the laser diode is two-dimensional [9-13]. For continuous-wave operation, undesirable emission spectrum and mode shift [14-18], and an increase in threshold current [19-22] were observed experimentally by different research groups.

The purpose of this work is, therefore, to quantitatively investigate internal heating and its effect on the performance of conventional stripe-geometry double-heterostructure (DH) lasers. The effect on the waveguiding parameters and radiation patterns by the lateral gradient of the temperature distribution will be discussed by means of a mathematical model. Also studied will be the threshold current increase and the emission wavelength shift caused by a rise in temperature for CW operation.

In order to illustrate the nature of the problem under investigation, a brief review of semiconductor injection lasers and related background materials is presented in section I(A). The problem and the approaches for solution are described in section I(B). The mathematical model is discussed in detail in section II, including the solutions for current spreading, electron concentration, heat diffusion and wave equation. A computer program based on these solutions is used to create a number of curves for studying the effect of temperature rise. The results, in comparison to existing experimental data, are analyzed and discussed in section III.

A. Review of the Semiconductor Injection Laser

The possibility of light amplification through the stimulated recombination of carriers injected across a p-n junction was first predicted by Basov et al. [23] in 1961, and the actual lasing action was achieved by several research groups [24-26] in 1962. These early injection lasers were generally rectangular chips of GaAs containing a p-n junction perpendicular to two polished or cleaved ends of the chip [27]. At this developmental stage, lasers were operated with a short pulse and very high diode current densities at an extremely low temperature. Since then, the invention of heterostructures and the development of direct-band-gap semiconductor materials and fabrication techniques have improved both the efficiency of the device and the confinement of injected carriers and optical field in a narrow region of the device to such a degree that it is now possible to operate continuous wave injection lasers at room temperature with a threshold current density lower than 700 A/cm^2.

1. Principle of operation

The electroluminescent diode is basically a device in which electrons and holes are injected into the p- and n-type regions, respectively, by the application of a forward bias V, as shown in Fig. 1.1 [28,29].

To reach a lasing action, stimulated emission should be achieved by carrier population inversion, a condition whereby the upper of two electronic levels separated in energy by $\Delta E = E_2 - E_1$ has a higher probability of being occupied by an electron than the lower level.

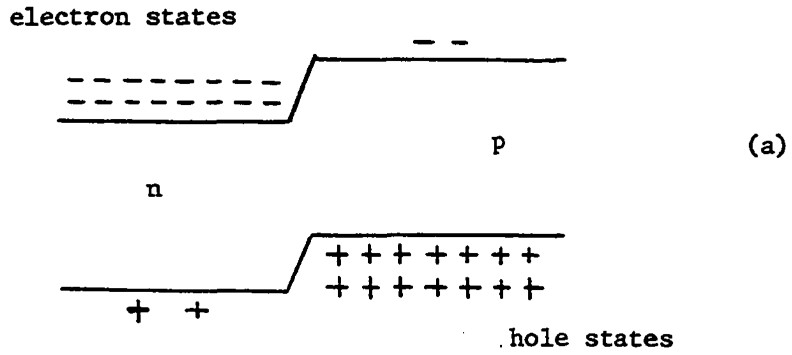

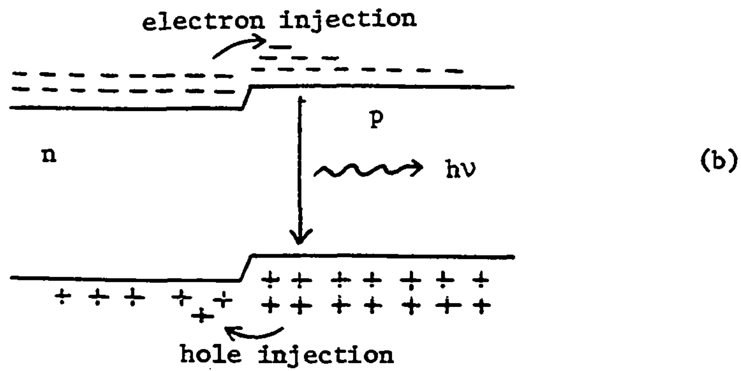

(a) zero bias - no injection
(b) forward bias - carrier injection and radiative recombination

Fig. 1.1. Electroluminescent p-n junction operation

Then the probability of a photon with energy $h\nu \approx \Delta E$ inducing a downward electron transition will exceed the probability for an upward transition, or photon absorption. Light amplification becomes possible, therefore, when an incident photon stimulates the emission of a second photon with energy approximately equal to the energy separation of the electronic levels.

Population inversion in a semiconductor is illustrated in Figure 1.2, which shows the electron energy as a function of the density of states in an undoped semiconductor at sufficiently low temperature for the conduction band to be empty of electrons. When electrons are excited, they fill the lower energy states of the conduction band to F_c, the quasi-Fermi level for electrons. An equal density of holes is generated to conserve the charge neutrality in the material, and thus the states in the valence band to F_v are empty of electrons.

Photons with energy greater than E_g but less than $F_c - F_v$ cannot be absorbed since the conduction band states are occupied, but these photons can induce downward electron transitions from the filled conduction band states into the empty valence states. With increasing temperature, a redistribution of the electrons and holes occurs, but the basic conditions for stimulated emission remain defined as above in terms of the separation of the quasi-Fermi levels, $F_c - F_v > h\nu$. The threshold condition for lasing is that the gain equals the optical losses in the cavity at radiation photon energy.

A unique feature of the laser diode, not present in other laser types, is the ability to obtain stimulated emission by minority carrier injection using a p-n junction or heterojunction. The efficient

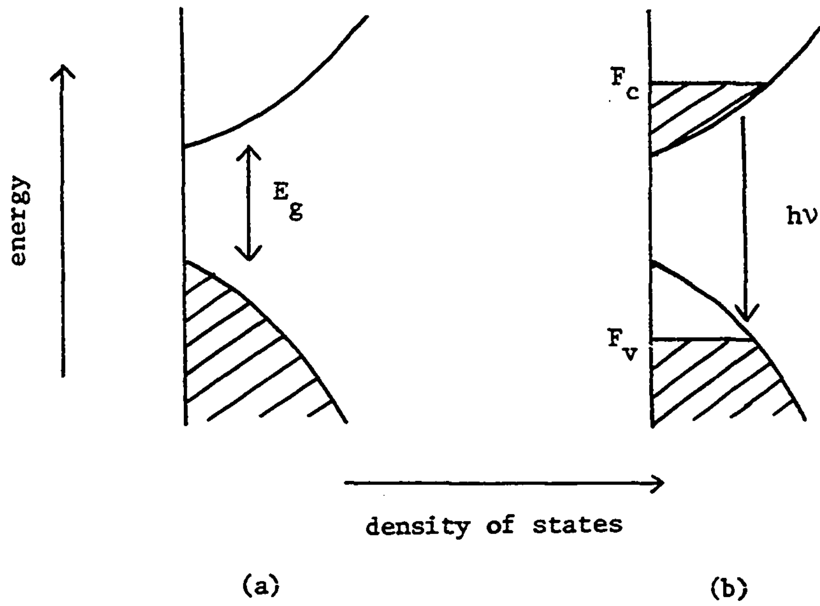

(a) in equilibrium at $T = 0\ ^oK$
(b) under high excitation

Fig. 1.2. Electron energy as a function of the density of states in an intrinsic direct bandgap semiconductor

operation of a laser diode requires effective carrier and radiation confinement at the vicinity of the junction. The detailed structures for such an efficient confinement are further discussed in the following section.

2. Structure of the device

As mentioned earlier, the homostructure laser requires a very high current density through the p-n junction in order to reach the threshold lasing condition because the recombination region is too wide as a result of minority carrier diffusion. In addition, since the optical field exists in an inefficient waveguide of uncertain origin, the efficiency with which injected electrons are utilized for lasing transition is low.

In a typical GaAs laser diode, the injected carrier density necessary to reach lasing threshold is about 10^{18} cm^{-3} [28,30,31] at room temperature. Minimizing the threshold current density requires restricting the width of the recombination region d by placing a potential barrier for minority carriers at a distance less than the diffusion length from the p-n junction. Also, the optical field intensity is guided by a built-in slab waveguide resulting from the difference in the dielectric constants of the heterostructure materials.

These multilayered heterojunctions, which were first introduced by Kroemer [32] in 1963, later allowed a revolutionary improvement in carrier and optical confinement perpendicular to the junction planes. In the late 1960s, Hayashi et al. [33], Panish et al. [34], and Kressel and Nelson [35] began research on GaAs/AlGaAs heterojunction lasers

which resulted in significant reduction of threshold current density, and eventually produced lasers capable of operating continuously at room temperature.

In discussing heterojunctions, it is convenient to designate the narrower energy gap layers by their conductivity type as n or p, and to designate the wider energy gap layers as N or P. These designations will be used throughout this work.

In a typical DH (double-heterostructure) laser, carriers and wave-guide have the same boundaries on both sides of the recombination region. A schematic energy band diagram and the refractive index structure for such a device are shown in Figure 1.3. The DH laser made of GaAs-$Al_xGa_{1-x}As$ or $Al_xGa_{1-x}As$ - $Al_yGa_{1-y}As$ is presently one of the most advanced heterostructure lasers being developed for use in optical communication systems. With this structure it is possible to emit a wavelength in the range of 0.78-0.9 μm, depending on the mole fraction of AlAs in the active layer. The energy bandgap of $Al_xGa_{1-x}As$ is shown in Figure 1.4. A GaAs system grown by liquid phase epitaxy (LPE) was the first junction laser capable of CW operation at room temperature [36]. The layer structure is either N-p-P or N-n-P, thus forming a symmetrical slab waveguide where $\bar{n}_2 = \bar{n}_3 < \bar{n}_1$.

One of the difficulties in fabricating a heterostructure laser is lattice constant matching at the heteroboundaries. The lattice discontinuities at the boundaries result in a number of nonradiative recombination centers which trap minority carriers otherwise available for stimulated emission.

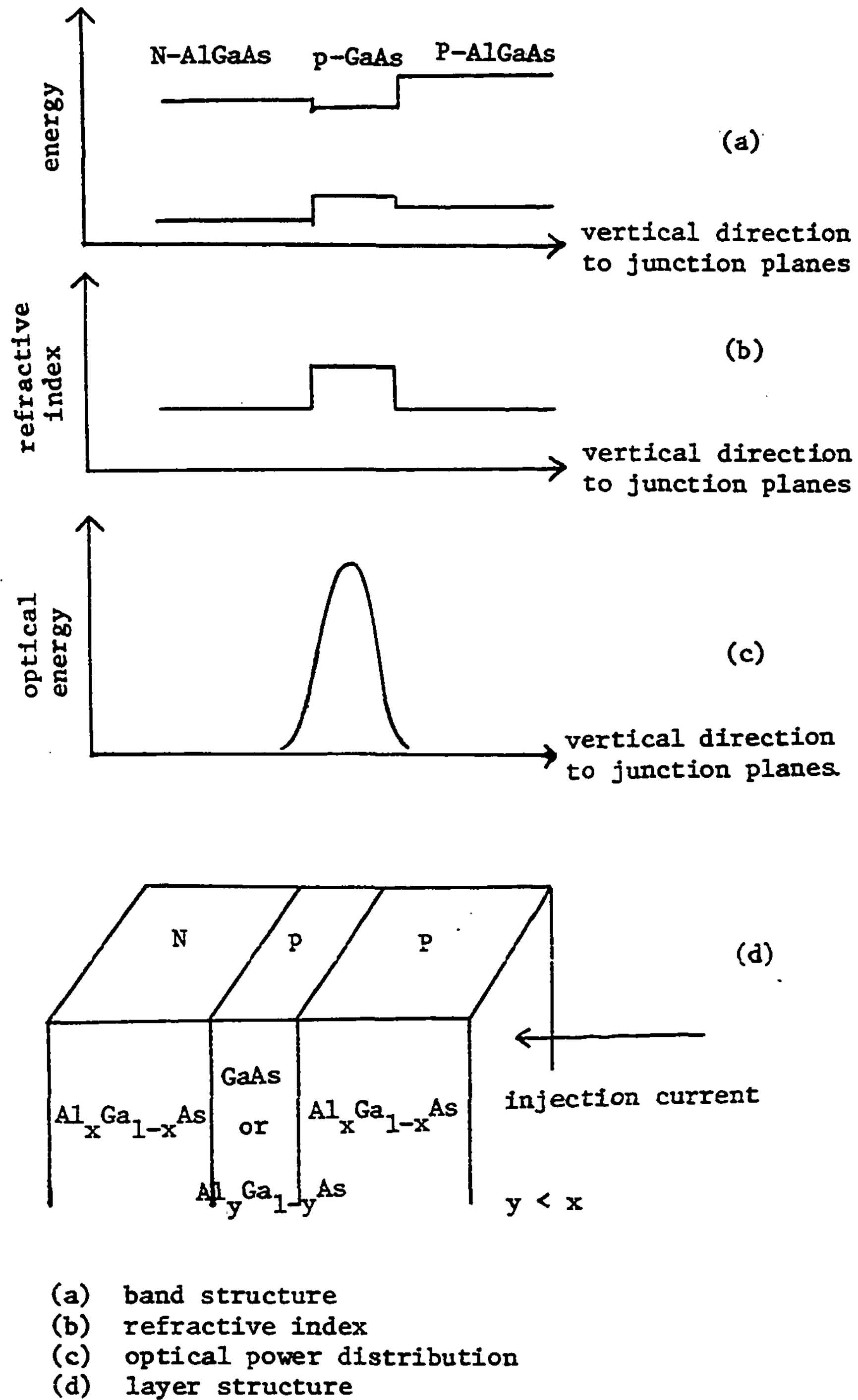

(a) band structure
(b) refractive index
(c) optical power distribution
(d) layer structure

Fig. 1.3. Schematic representation of a broad-area DH laser

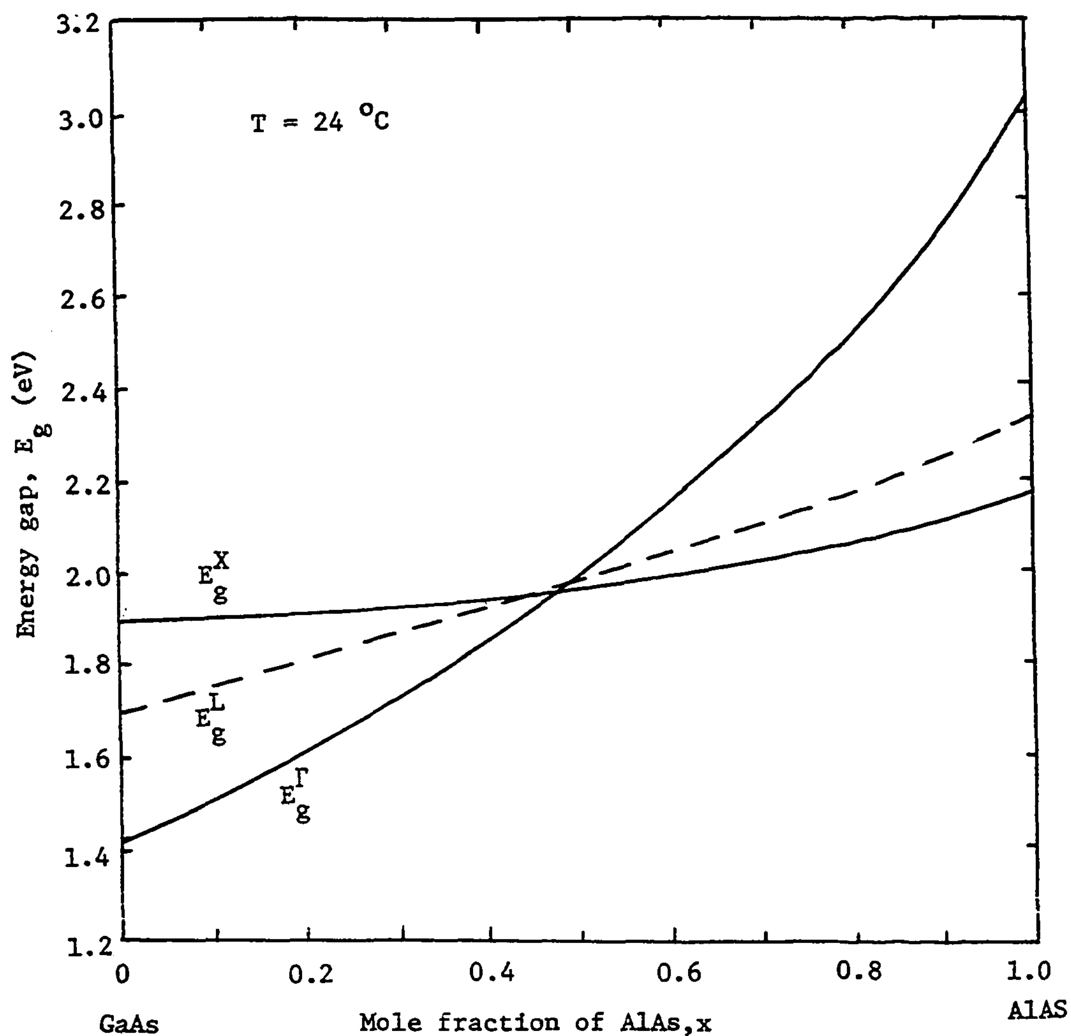

Fig. 1.4. The compositional dependence of the E_g^{Γ} direct energy gap and the E_g^X and E_g^L indirect energy gaps for $Al_xGa_{1-x}As$. The composition region between $0.4 < x < 0.5$ is somewhat uncertain. From [37]

So far, many different III-V compound semiconductor materials have been developed for longer wavelength injection lasers [38]. Ternary semiconductor alloys have been widely used in various device applications because of their ability to adjust the energy gap. With the exception of the GaAs-$Al_xGa_{1-x}As$ system, however, the changing lattice constant with composition in the ternary alloys makes it impossible to obtain the required performance or to fabricate the desired structures at a particular wavelength or bandgap energy.

A fourth element could be added to a ternary alloy to minimize lattice mismatch while maintaining the desired bandgap. InGaAsP/InP is the most promising quaternary compound for both lasers and LEDs at 1.3 μm, the minimum optical loss and chromatic dispersion region for modern high-silica fibers, but the strong inherent temperature dependence of InGaAsP/InP lasers appears to rule out their use at the elevated ambient temperatures at which many land-based communication systems must operate [2]. Kressel and Butler [29] as well as Casey and Panish [39], provide a well-summarized review on these III-V compound materials and fabrication techniques, including a discussion of the AlGaAsSb/AlGaSb system.

In addition to vertical confinement with these heterostructures, it is also important in many laser applications that the current flow be restricted laterally to a narrow stripe along the length of the laser. This modification drastically reduces the total driving current for threshold. Lasers with the lateral confinement feature are called stripe-geometry lasers.

There are a number of different ways to realize these stripe-geometry structures at the present time [39,40]. Depending on the lateral waveguiding mechanism, they may be classified into two different groups: conventional gain-guiding lasers and index-guiding lasers.

Proton-bombarded [41] or oxygen-implanted [42] stripe lasers fall into the former category. In this type of structure, regions of high resistivity are created in the p- and P-layers either by proton-bombardment or by oxygen-implantation, both of which define the boundaries of the stripe. A schematic of a proton-bombarded stripe laser is given in Figure 1.5. The driving current flows into the active layer only through the untreated region under the p-contact. However, the optical property of the bombarded region can be restored by an annealing process in order to prevent any increase in the optical loss for guided modes.

Contact-stripe lasers [43] also fall into the gain-guiding laser category. As shown in Figure 1.6, an SiO_2 layer is deposited to create an insulating barrier, and the stripe window is then opened up by a photolithographic process. The p-side contact is normally evaporated without alloying in order to avoid the strain which is particularly deleterious to GaAs/AlGaAs laser diode life. In this structure, the top p-layers are relatively low doped ($\sim 5 \times 10^{17}$ cm^{-3}) in order to reduce lateral current spreading. Lateral current spreading will be further discussed in section II(A).

The second group of stripe-geometry lasers--or index-guiding lasers--includes buried-heterostructure (BH) [44,45], double-diffused stripe (DDS) [46], channeled substrate planar (CSP) [47] lasers, etc. These structures contain inbuilt refractive index steps which provide waveguiding

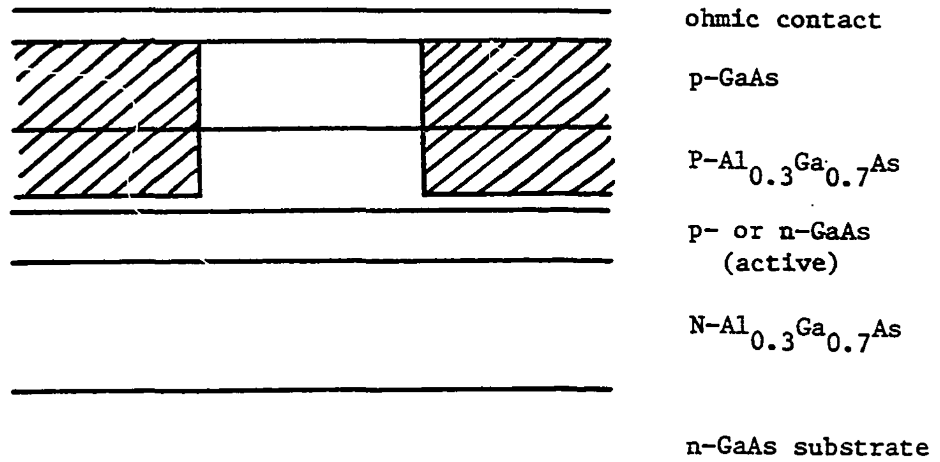

Fig. 1.5. Epitaxial layer structure of a shallow proton-bombarded stripe laser

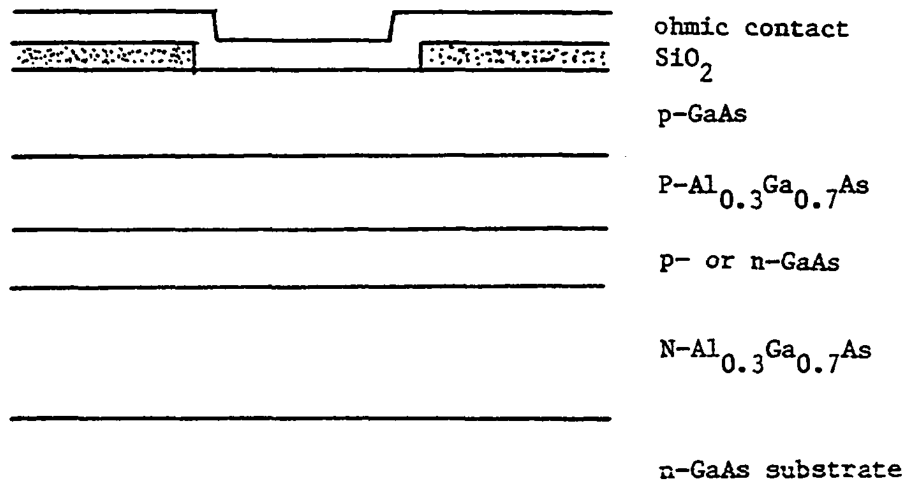

Fig. 1.6. Layer structure of a contact-stripe laser

in the lateral direction. These index-guiding lasers generally offer superior linearity in light output vs. current characteristics over conventional gain-guiding lasers [48].

Waveguiding in the dielectric slab-waveguide structure is extensively studied by Marcuse [49]. Guiding in a perpendicular direction to the junction planes is dictated by the refractive index steps of the heterostructure. In gain-guiding lasers, optical confinement in the lateral direction is primarily the result of dielectric constant variation caused by gain distribution in the active region. Dyment [43] and Yonezu et al. [50] observed that the radiation patterns of such lasers can be described by Hermite-Gaussian functions. The field intensity patterns will be further discussed in section II(C).

3. Previous work on thermal property of the device

As mentioned earlier, two different aspects of the laser thermal property have been investigated by various research groups. The first is the sensitivity of laser characteristics at different heat sink temperatures. Goodwin et al. [3], Hwang et al. [4], Hayakawa et al. [6], Yonezu et al. [20], experimentally observed the increase of the threshold current and decrease of the differential quantum efficiency with increasing heat sink temperature for GaAs/AlGaAs DH lasers. Asada et al. [5] and Yano et al. [22] also reported even more severe dependence of the laser parameters on ambient temperature for InGaAsP/InP lasers.

The pulsed threshold current for a well-confined DH laser at the heat sink temperature T_h is empirically expressed as

$$I_{th}^{P}\ (T_h) = I_{th}^{P}\ (300°K)\ \exp\left(\frac{T_h - 300°K}{T_o}\right) \tag{1.1}$$

where

I_{th}^{P} is the threshold current for pulsed operation,

T_o is the characteristic temperature of the laser diode.

The characteristic temperature T_o depends strongly on the active and inactive layer materials. Goodwin et al. [3] suggested that electron leakage current at the heteroboundary was mostly responsible for the threshold current increase. For strongly confined $Al_xGa_{1-x}As/Al_yGa_{1-y}As$ DH lasers with substantial heterojunction step heights, $\Delta x = y - x$, the characteristic temperature lies in the range of 120-165°K. For weakly confined lasers, however, the threshold current was found to increase at a faster than exponential rate, with a tendency for runaway increase with temperature. For typical InGaAsP/InP DH lasers, the characteristic temperature fell between 40-80°K, which is much lower than that for GaAs/AlGaAs systems. Therefore, the device sensitivity to ambient temperature is far more serious in these lasers [22].

A second aspect of concern is the effect of internal heating. For a well-fabricated GaAs/AlGaAs DH laser, a forward voltage of 1.6 V and a driving current in the range of ~100 mA are necessary to achieve the threshold condition. This means that ~160 mW of power flows into the device to produce less than a few mW of optical energy. For CW operation, therefore, a large portion of input energy is unavoidably converted into internal heating which effectively increases the device's operating temperature.

According to Pankove [51], the power dissipated internally consists of:

(i) the fraction of the power supplied to the p-n junction which is not converted into radiation, i.e., nonradiative recombination,

(ii) joule losses of I^2r for each layer,

(iii) the fraction of the radiation which does not leave the laser. A fraction of the spontaneous emission is absorbed as heat at the substrate and capping layers.

The power dissipation by (i) and (iii) is accounted for by the differentiol quantum efficiency η_d. Hence, the total power dissipated in the device P_d is

$$P_d = \begin{cases} (I\,V_j + I^2 r_s)\chi & \text{for } I \le I_{th} \\ [I_{th}V_j + (I - I_{th})(1 - \eta_d)V_j + I^2 r_s]\chi & \text{for } I > I_{th} \end{cases} \quad (1.2)$$

Here

V_j is the junction voltage,

I is the diode current,

I_{th} is the threshold current,

r_s is the series resistance of the diode,

χ is the duty cycle.

The joule loss term, I^2r_s, is usually very small when compared to other heat sources because modern laser diodes have extremely thin layer structures. The series resistance r_s is commonly lower than 2 ohms, and sometimes as low as 0.05 ohms.

The temperature rise in the device can be expressed as

$$\Delta T(x,y,z) = R_t(x,y,z)\ P_d \tag{1.3}$$

where

$\Delta T(x,y,z)$ is the local temperature rise from the heat sink temperature,

$R_t(x,y,z)$ is the thermal resistance at the location.

The thermal resistance R_t is defined as that quantity which, when multiplied by the dissipated power P_d, yields the temperature at the point indicated in (1.3).

The thermal resistance of lasers has been considered theoretically by Garel-Jones and Dyment [21] who used a one-dimensional model for heat flow applicable to oxide stripe-geometries and etched mesa structures. Joyce and Dixon [9] developed a Fourier-series model applicable to proton-bombarded lasers, mainly taking into account heat generated within the active region. Kobayashi and Furukawa [10], and more recently Newman et al. [12] and Duda et al. [13], considered other heat sources at various locations including the joule losses at each layer and heat absorbed from spontaneous emission.

Paoli [15] developed a technique for thermal resistance measurement using a null measurement of the exact wavelength of a single Fabry-Perot mode. With this method, average temperature rise in the active region by the CW driving current was accurately measured (~ <0.2°C resolution). Ito and Kimura [52] used this technique to study the transient thermal properties of laser diodes.

The work of Kobayashi and Iwane [11] represents the only experimental report on lateral distribution of junction temperature. They used a thermal plotter to directly measure temperature at the facet surface. Because of the thermal plotter's poor resolution, the data is not as reliable as it should be.

B. Statement of the Problem

The performance of a semiconductor laser can be characterized in terms of the emission wavelength, threshold current density, quantum efficiencies, radiation pattern, device lifetime, and the linearity of the current-light output characteristics. These parameters strongly depend on the material, structure, and the fabrication process used for the laser.

As discussed earlier, the thermal property of the laser also affects these important physical quantities significantly. In many applications, the fluctuation of the emission characteristics and the increase in threshold current make the laser very difficult to use, if not impossible.

A natural question arises about whether the thermal effect may be substantially reduced by proper designing of the laser structure. The answer is not readily available because previous work on laser thermal properties has generally been qualitative in nature and also because thermal resistance was considered only as a problem isolated from other laser characteristics.

This thesis has two aims. One is to develop a quantitative laser model for studying the internal heating effects on the mode characteristics, threshold current, and emission spectrum in a conventional

gain-guiding stripe-geometry DH laser; the other is using this model to establish a design principle of the laser structure in order to minimize such undesirable effects.

The basic problem involves several subproblems, as shown in Figure 1.7. First, the electron concentration in the active layer is determined by solving the continuity equation. If appropriate, lateral current spreading should be taken into account in the continuity equation.

For CW operation, the static thermal distribution caused by the driving current is solved by the heat diffusion equation with properly assumed boundary conditions. Two things can be determined from this solution: the average temperature rise in the active region from the heat sink temperature and the lateral thermal distribution in the active region.

The nonuniform dielectric constant can thus be obtained from the electron concentration and the temperature distribution solved for in these subproblems. The next step is to solve the wave equation in the resulting inhomogeneous slab waveguide illustrated in Figure 1.8. Since the exact solution is not available in this complicated structure, two steps of approximation are necessary to make the problem workable. The first step is to approximate the distributions of gain constant and refractive index in waveguiding layers with parabolic functions. Because it is difficult to match the boundary conditions at active and inactive layer boundaries, an effective dielectric constant is defined for the three layer waveguide.

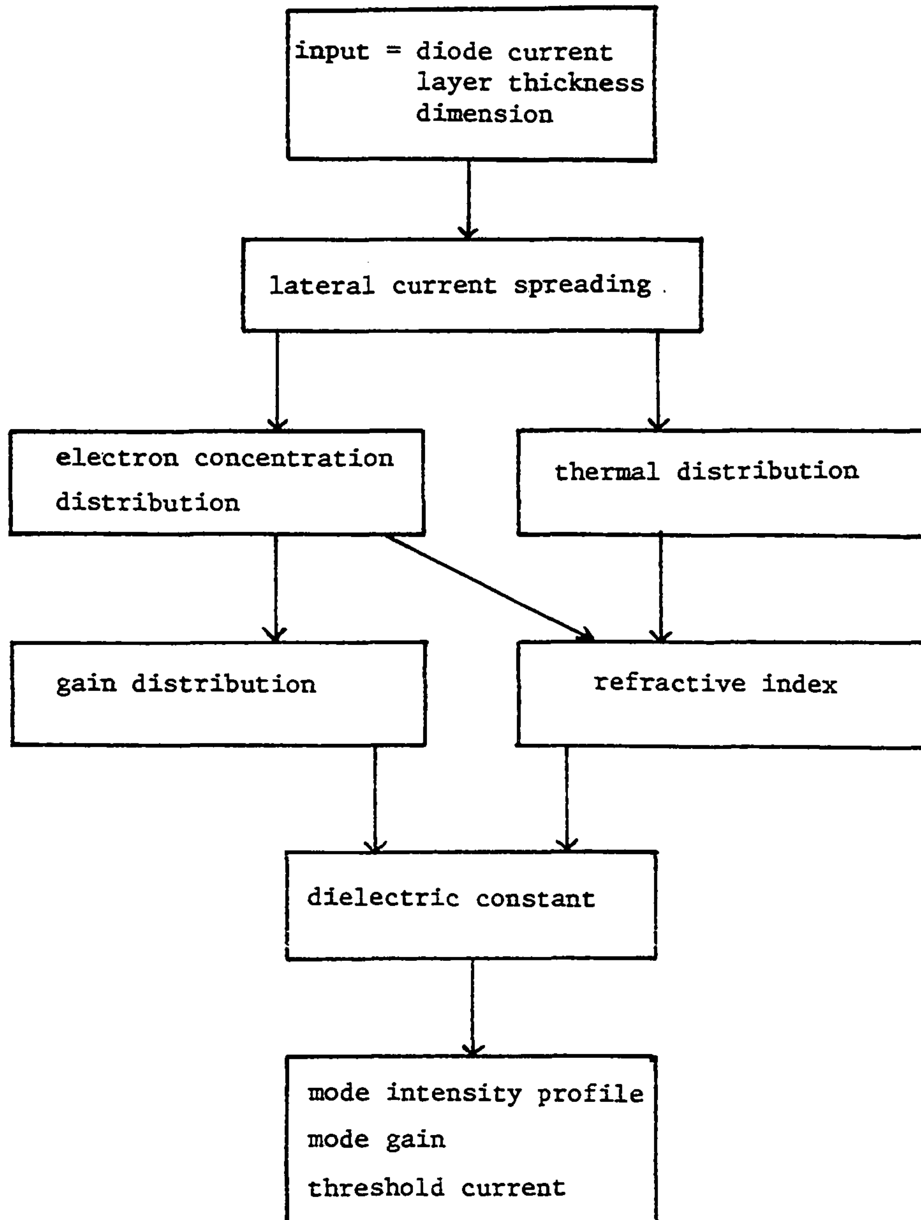

Fig. 1.7. Schematic representation of the laser model

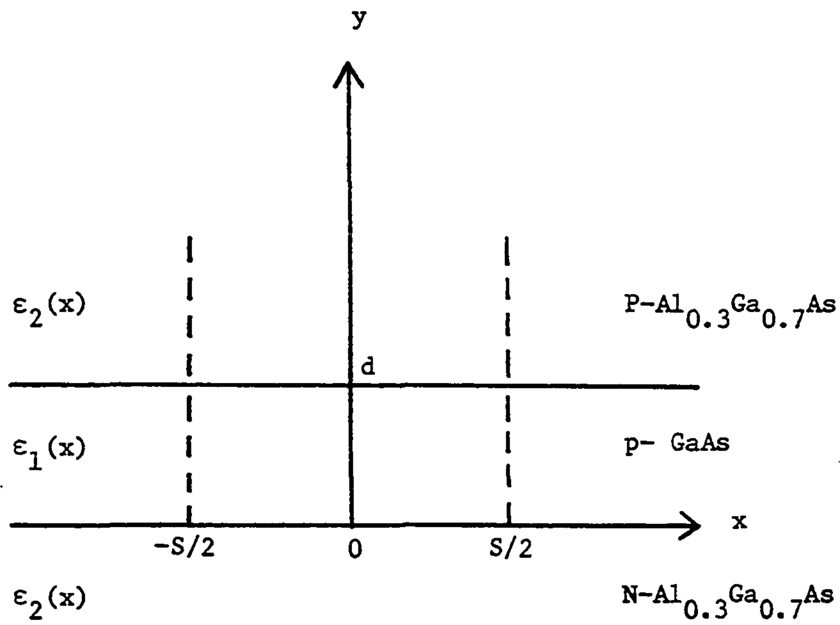

Fig. 1.8. Coordinate system for the dielectric slab waveguide

The guided mode patterns can be determined, then, with the aid of eigenfunctions of the boundary value problem under consideration. The results of these subproblems are compared with available experimental reports to ensure the accuracy of the model.

The model is used to investigate the thermal effects on some of the device parameters. The effect on the modeguiding characteristics is discussed in terms of focusing or defocusing by the refractive index profile. The increase of threshold current and spectrum shift caused by junction heating is also discussed.

The model is also used to establish a guideline for reducing such undesirable thermal effects on device characteristics. The effects of layer thicknesses and the dimensions of the laser are rigorously investigated.

II. THE MODEL

In this section, the subproblems of the laser model are discussed. The laser structure shown in Figure 2.1 is assumed to be perfectly fabricated so that no local heating exists. It is also assumed that the laser is symmetrical to the y-axis. The coordinate system shown in Figure 1.8 will be used throughout this work, except in the case of the heat equation which requires a more complex system. It is further assumed that there is no variation of current density, electron concentration, temperature, and optical intensity in the z direction.

A. Lateral Current Spreading and Electron Diffusion

1. Lateral current spreading

In a broad-area laser, current flow is one dimensional and current density in the active region is uniformly distributed. In many stripe-geometry lasers, however, current flow is two dimensional because the majority carrier drift current in the p- and P-layers spreads laterally, as shown in Figure 2.2. In well-fabricated proton-bombarded lasers, current spreading is minimal because the resistivity of the bombarded area is very high. However, current spreading is significant in contact-stripe [53] and conventional planar-stripe [50] lasers, thereby increasing their threshold current density in comparison to broad-area contact lasers fabricated from the same material when the strip width is reduced below 20 μm. Its effect becomes particularly severe for strips narrower than 10 μm.

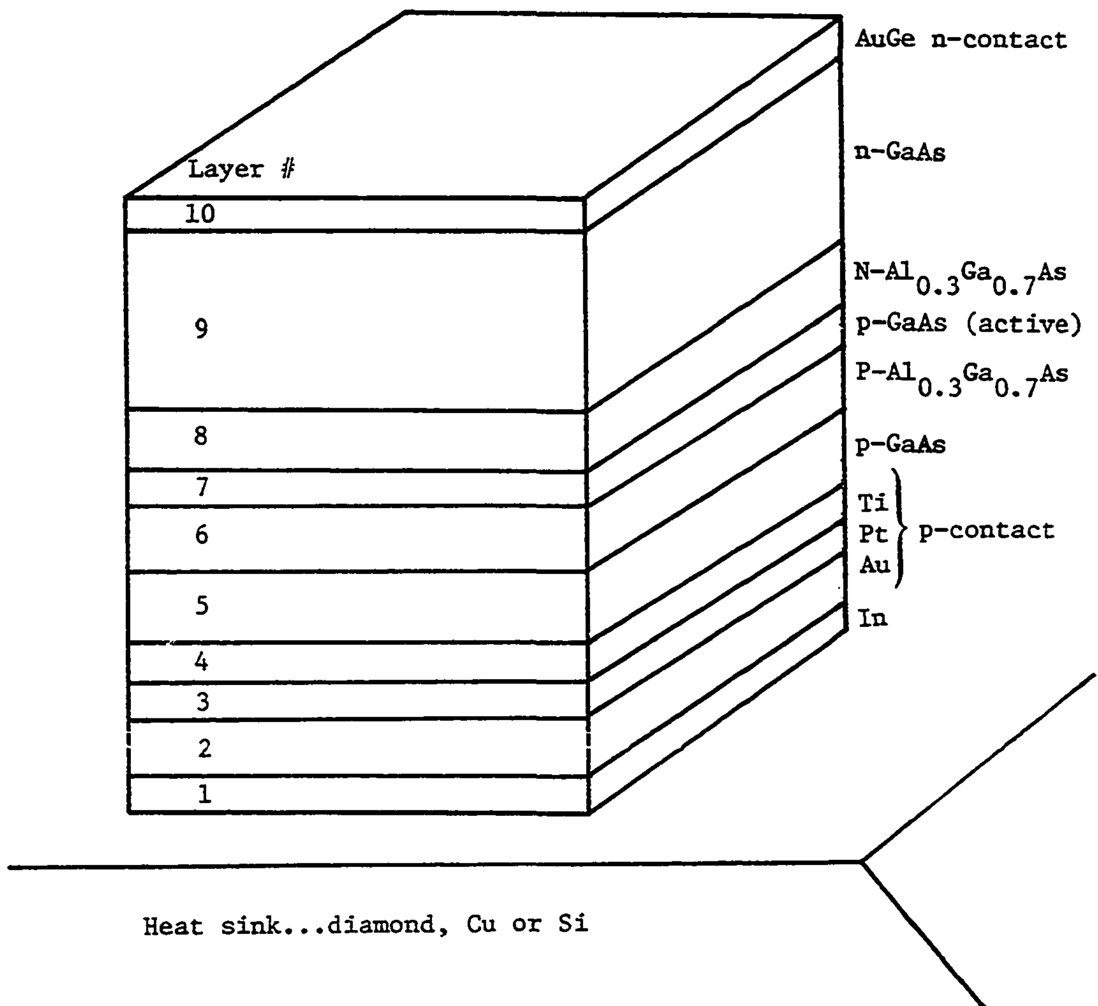

Fig. 2.1. Complete structure of a DH laser mounted on a heat sink

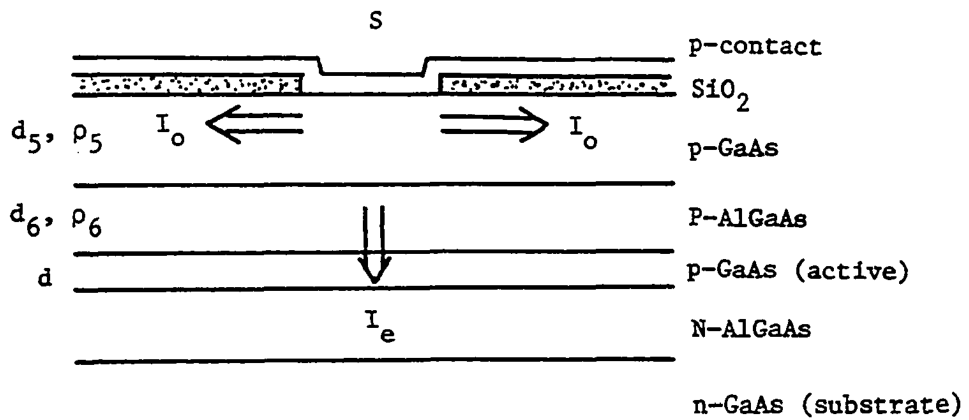

(a)

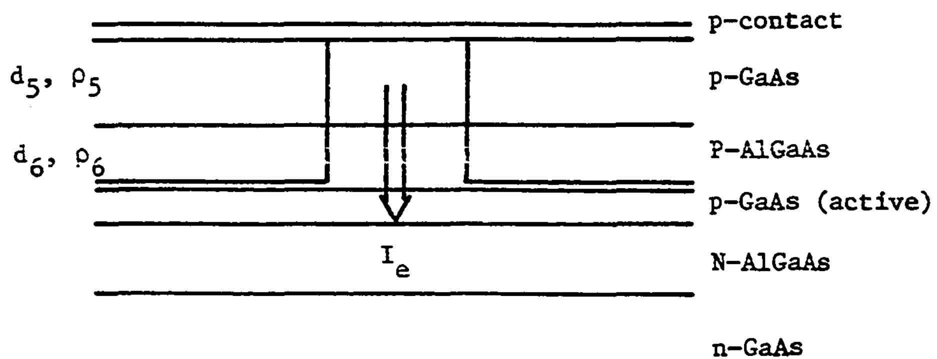

(b)

Fig. 2.2. Schematic representation of current spreading in stripe-geometry lasers. (a) contact-stripe (b) proton-bombarded. The spreading is not significant in a well fabricated proton-bombarded DH laser

In the approaches taken by Yonezu et al. [50] and Tsang [53], the total injection current I is considered as the sum of the uniform current under the stripe I_e and the spreading current I_o flowing out to the $\pm x$ direction, as indicated in Figure 2.2.

$$I = I_e + 2I_o \tag{2.1}$$

The spreading current I_o is determined by solving Equation (2.2). The current across the junction between x and x + dx can be expressed as $-dI_x$,

$$-dI_x = L \cdot J_s \cdot [\exp(\beta V_x) - 1]\ dx \tag{2.2}$$

where J_s is saturation current density, $\beta = q/nkT$, and V_x is the junction voltage at x. The terms q, n, k, and T represent the electron charge, a constant normally equal to 2, Boltzmann's constant, and absolute temperature, respectively.

Solving (2.2) yields [50], as further discussed in Appendix (A),

$$I_o = (2LI_e/\beta R_s S)^{1/2} \tag{2.3}$$

$$R_s = \left(\frac{d_5}{\rho_5} + \frac{d_6}{\rho_6}\right)^{-1} \tag{2.4}$$

where R_s is the composite sheet resistance of the p- and P-layers in x direction, amd S and L are stripe width and laser cavity length, respectively.

The current flowing across the junction under the stripe can be considered uniform. That is,

$$J_y(x) = J_e \equiv I_e/SL \qquad \text{for} \qquad |x| \le \frac{S}{2} \tag{2.5}$$

Outside the stripe region, however, a potential drop in x direction exists in the p- and P-layers because of finite sheet resistance R_s. As a result of (2.2), the distribution of the current density flowing across the junction for the region is given by

$$J_y(x) = I_o \left[\ell_o L \left(1 + \frac{|x| - S/2}{\ell_o} \right)^2 \right]^{-1} \quad \text{for } |x| \ge \frac{S}{2} \tag{2.6}$$

where

$$\ell_o = 2L/\beta R_s I_o \tag{2.7a}$$

$$= (2/\beta R_s J_e)^{1/2} \tag{2.7b}$$

The condition $J_y(\pm\frac{1}{2}S) = J_e$ for (2.6) is applied to derive (2.7b) from (2.7a).

Through the use of (2.1) and (2.3), the current density at the p-contact can be expressed as

$$J \equiv I/SL = J_e + (8\, J_e/\beta R_s S^2)^{1/2} \tag{2.8}$$

Solving (2.8) for J_e gives

$$J_e = J + 4/\beta R_s S^2 - [(J + 4/\beta R_s S^2)^2 - J^2]^{1/2} \tag{2.9}$$

Hence, the current density arriving at the active layer can be calculated by (2.5), (2.6), and (2.9), with the knowledge of sheet resistance R_s. Figure 2.3 illustrates the lateral current spreading for several R_s

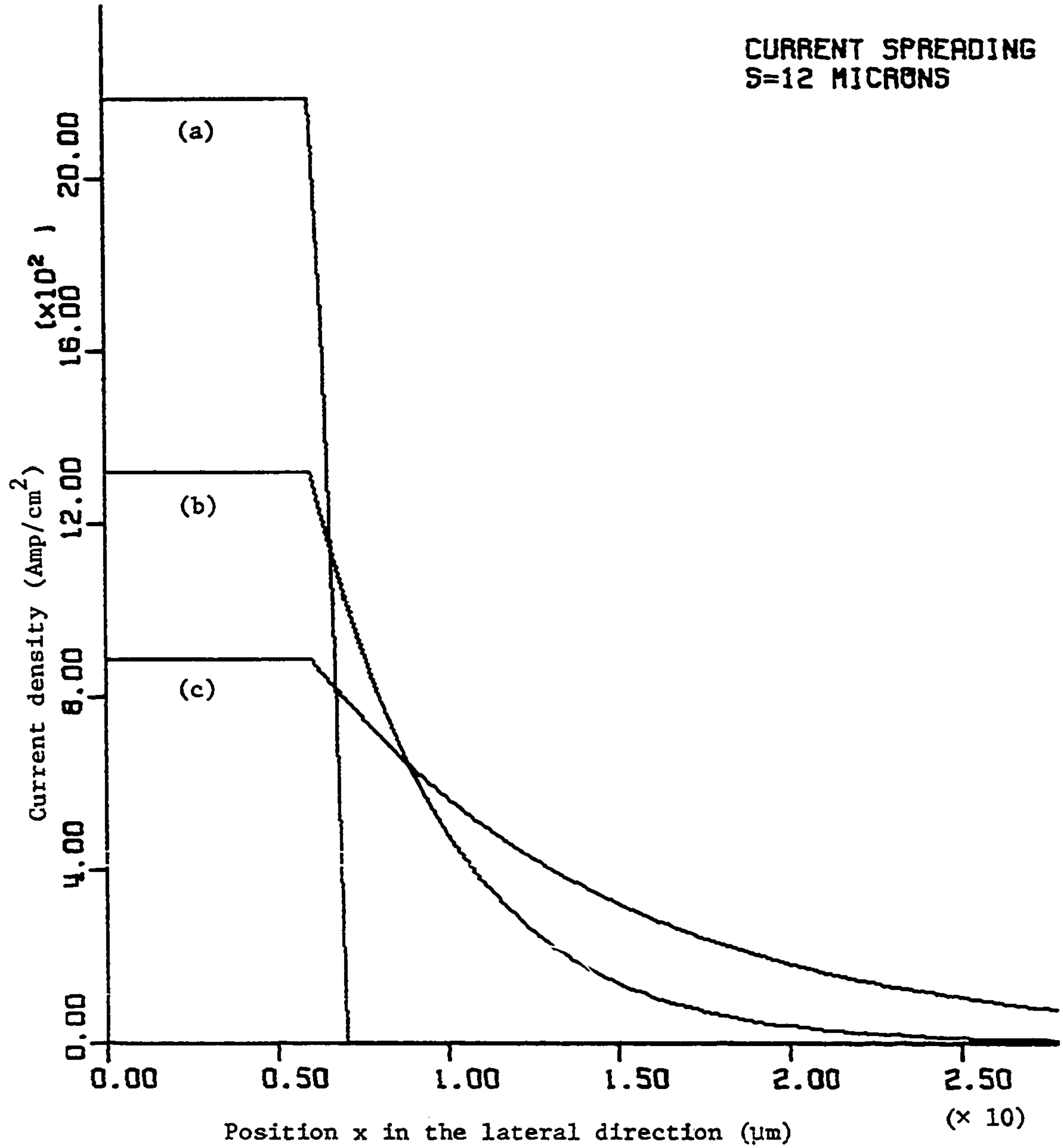

Fig. 2.3. The calculated current distribution flowing into the active region for different composite sheet resistances. (a) $R_s = 10^7\ \Omega$ (b) $R_s = 500\ \Omega$ (c) $R_s = 150\ \Omega$

In stea[illegible]

where L_a [illegible]

(2.5) ar[illegible]

Sin[illegible]

necessar[illegible]

exponent[illegible]

Since th[illegible]

to I_o,

Thus, ξ [illegible]

Equ[illegible]

values. For a well-fabricated, proton-bombarded laser, R_s is extremely high ($\sim 10^7 \Omega$), and current spreading is negligible.

2. Electron out-diffusion in the active layer

For uniform planar structured lasers, the current density given by (2.5) and (2.6) flows into the active layer. A significant amount of carrier diffusion occurs toward the edges of the laser cavity. Because the active layer is usually very thin in comparison to the width of the stripe, and also because of the energy barrier at the p-P heterojunction [30,54], it is safe to assume that the electron concentration is uniform in y direction.

The active layer is typically either undoped or very lightly doped so that the electron and hole concentration are almost equivalent at a high injection level. Therefore, the nature of the carrier out-diffusion is ambipolar diffusion. The ambipolar diffusion constant for $p \simeq n$ is reduced to [55]

$$D_a \simeq 2D_p \tag{2.10}$$

where D_p is the hole diffusion constant. The derivation of (2.10) is summarized in Appendix (B).

At or below threshold condition, where hole burning by stimulated emission is negligible, the electron concentration in the active layer can be found by solving the continuity equation (2.11).

$$D_a \nabla^2 n - \frac{\partial n}{\partial t} + \frac{J_y(x)}{qd} - \frac{n}{\tau_n} = 0 \tag{2.11}$$

In steady-state, $\frac{\partial n}{\partial t} = 0$ with $\frac{\partial}{\partial y} = \frac{\partial}{\partial z} = 0$, (2.11) reduces to

$$\frac{d^2 n}{dx^2} - \frac{n}{L_a^2} = - \frac{J_y(x)}{D_a \, qd} \qquad (2.12)$$

where $L_a = (D_a \tau_n)^{1/2}$ is the ambipolar diffusion length. Substituting (2.5) and (2.6) into (2.12) yields

$$\frac{d^2 n}{dx^2} - \frac{n}{L_a^2} = - \frac{J_e}{D_a \, qd} \qquad |x| \leq \frac{S}{2} \qquad (2.13a)$$

$$= - \frac{J_e}{D_a \, qd} \left(1 + \frac{|x| - S/2}{\ell_o}\right)^{-2} \qquad |x| > \frac{S}{2} \qquad (2.13b)$$

Since Equation (2.13b) does not have a simple solution, it is necessary to approximate the right hand side of the equation with an exponential function. Let

$$J_e \left(1 + \frac{|x| - S/2}{\ell_o}\right)^{-2} \simeq J_e \exp\left[-\xi(|x| - \frac{S}{2})\right] \qquad (2.14)$$

Since the total spreading current from $x = \frac{S}{2}$ to $x = \infty$ should be equal to I_o,

$$L \int_{S/2}^{\infty} J_e \exp\left[-\xi(x - S/2)\right] dx \equiv I_o \qquad (2.15)$$

Thus, $\xi = 1/\ell_o$.

Equation (2.13) is approximated as,

$$\frac{d^2n}{dx^2} - \frac{n}{L_a^2} = -\frac{J_e}{D_a\, qd} \qquad |x| \le \frac{S}{2} \qquad (2.16a)$$

$$= -\frac{J_e}{D_a\, qd} \exp\left(-\frac{|x| - S/2}{\ell_o}\right) \qquad |x| > \frac{S}{2} \qquad (2.16b)$$

Solving (2.16a) with the boundary condition that the electron concentration is symmetrical about $x = 0$ gives

$$n(x) = 2B \cosh\left(\frac{x}{L_a}\right) + \frac{J_e L_a^2}{D_a\, qd} \qquad (2.17)$$

Also, the solution of (2.16b) with $n(\infty) = 0$ yields

$$n(x) = C \exp\left(-\frac{|x| - S/2}{L_a}\right) + \frac{\ell_o^2 L_a^2}{\ell_o^2 - L_a^2} \frac{J_e}{D_a\, qd} \exp\left(-\frac{|x| - S/2}{\ell_o}\right) \qquad (2.18)$$

The continuity of the electron concentration and gradient at $x = \pm\frac{S}{2}$ yields

$$2B \cosh\left(\frac{S}{2L_a}\right) + \frac{J_e}{D_a\, qd} L_a^2 = C + \frac{\ell_o^2 L_a^2}{\ell_o^2 - L_a^2} \frac{J_e}{D_a\, qd} \qquad (2.19)$$

and

$$\frac{2B}{L_a} \sinh\left(\frac{S}{2L_a}\right) = -\frac{C}{L_a} + \frac{\ell_o^2 L_a^2}{\ell_o^2 - L_a^2} \frac{J_e}{D_a\, qd}\left(\frac{-1}{\ell_o}\right) \qquad (2.20)$$

Solving (2.19) and (2.20) for B and C results in

$$B = \frac{1}{2}\zeta\left(-\frac{L_a}{\ell_o + L_a}\right)\exp\left(-\frac{S}{2L_a}\right) \tag{2.21}$$

$$C = \frac{1}{2}\zeta\left(-\frac{L_a}{\ell_o + L_a}\right)\left[1 + \exp\left(-\frac{S}{L_a}\right)\right] + \zeta - \frac{\ell_o^{\,2}}{\ell_o^{\,2} - L_a^{\,2}}\zeta \tag{2.22}$$

where

$$\zeta = \frac{J_e L_a^{\,2}}{D_a\, qd} \tag{2.23}$$

Substituting (2.21) and (2.22) into (2.17) and (2.18), the electron concentration in the active layer is written as

$$n(x) = \zeta\left(-\frac{L_a}{\ell_o + L_a}\right)\exp\left(-\frac{S}{2L_a}\right)\cosh\left(\frac{x}{L_a}\right) + \zeta \quad \text{for } 0 \le x \le S/2 \tag{2.24a}$$

and

$$n(x) = \zeta\left\{\frac{1}{2}\left(-\frac{L_a}{\ell_o + L_a}\right)\left[1 + \exp\left(-\frac{S}{L_a}\right)\right] - \frac{L_a^{\,2}}{\ell_o^{\,2} - L_a^{\,2}}\right\}\exp\left(-\frac{x - S/2}{L_a}\right) + \frac{\ell_o}{\ell_o^{\,2} - L_a^{\,2}}\zeta\exp\left(-\frac{x - S/2}{\ell_o}\right) \quad \text{for } x > S/2 \tag{2.24b}$$

The calculated electron concentration distribution is shown in Figure 2.4. Experimental values reported for diffusion length L_a and electron relaxation time τ_n are 3.0 ~ 3.6 μm and 2.8 ~ 3.3 nsec, respectively. As a

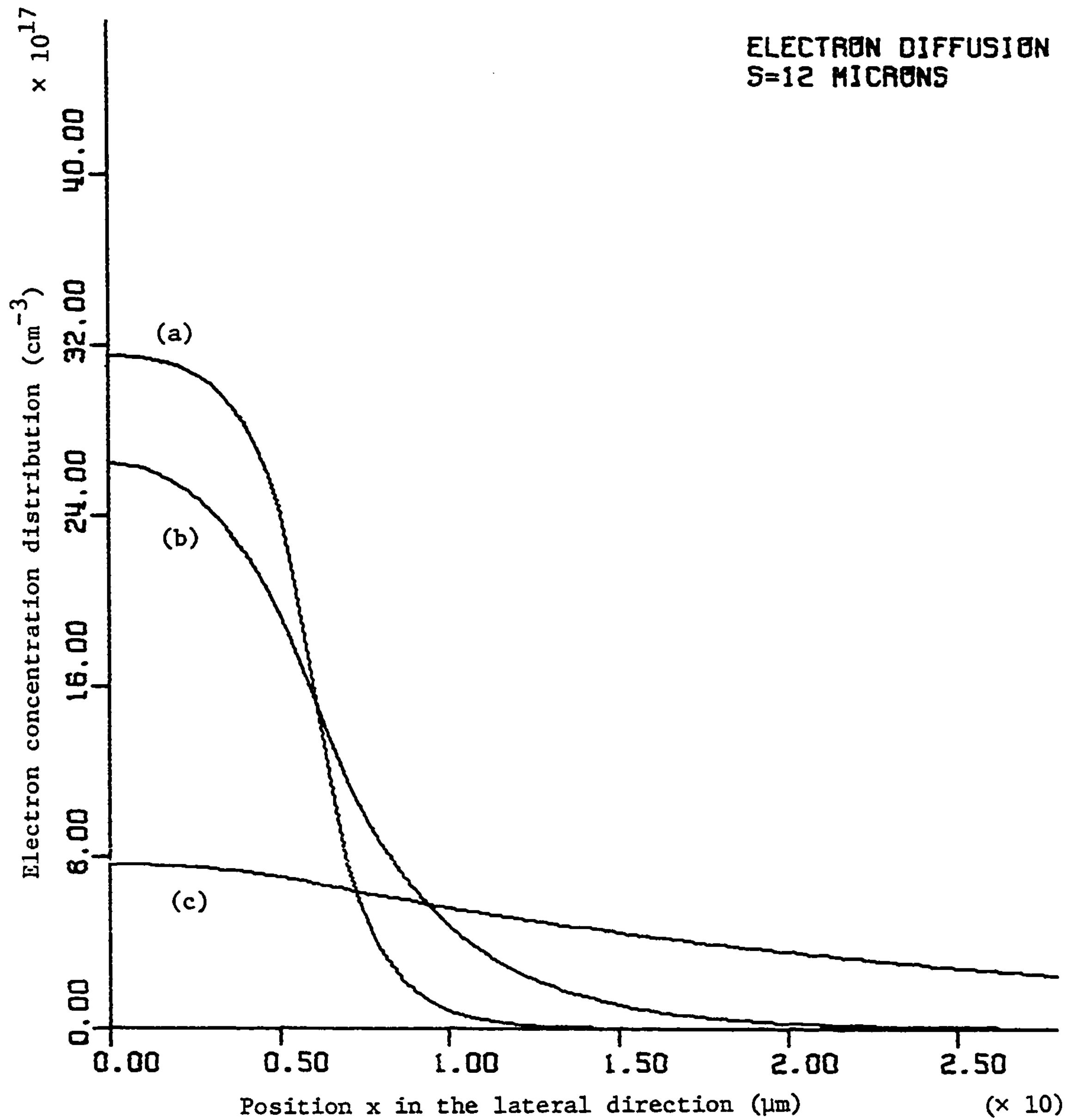

Fig. 2.4. The electron concentration profiles for different diffusion lengths (a) L_a = 1.7 μm (b) L_a = 3.4 μm (c) L_a = 6.8 μm $R_s = 10^7$ Ω is used

result, curve (b) in Figure 2.4 shows a good agreement with intensity profile of the spontaneous emission measured by Hakki [31].

B. Thermal Distribution in the Laser

1. Coordinate system and assumptions

To solve the heat equation in a multi-layer structure as shown in Figure 2.1, the coordinate system illustrated in Figure 2.5 was used. The thermal conductivities and dimensions of interest are summarized in Table 2.1.

The following assumptions were made for the heat equation:

(i) heating is mainly the result of nonradiative recombination in the active layer under the stripe. Heating is uniformly generated in the thin box-shaped region.

(ii) the thermal conductivities of each layer are constant in the layer

(iii) heat dissipation through the back side of the substrate and the sides of the diode is negligible. That is,

$$\frac{\partial T}{\partial \vec{n}} = 0 \qquad \text{at the top and sides} \tag{2.25}$$

where $\vec{n}$ is the normal vector corresponding to the top and the sides of the laser. The heat sink is ideal such that the temperature is constant at the interface. Or,

$$T = T_h \qquad \text{at the heat sink} \tag{2.26}$$

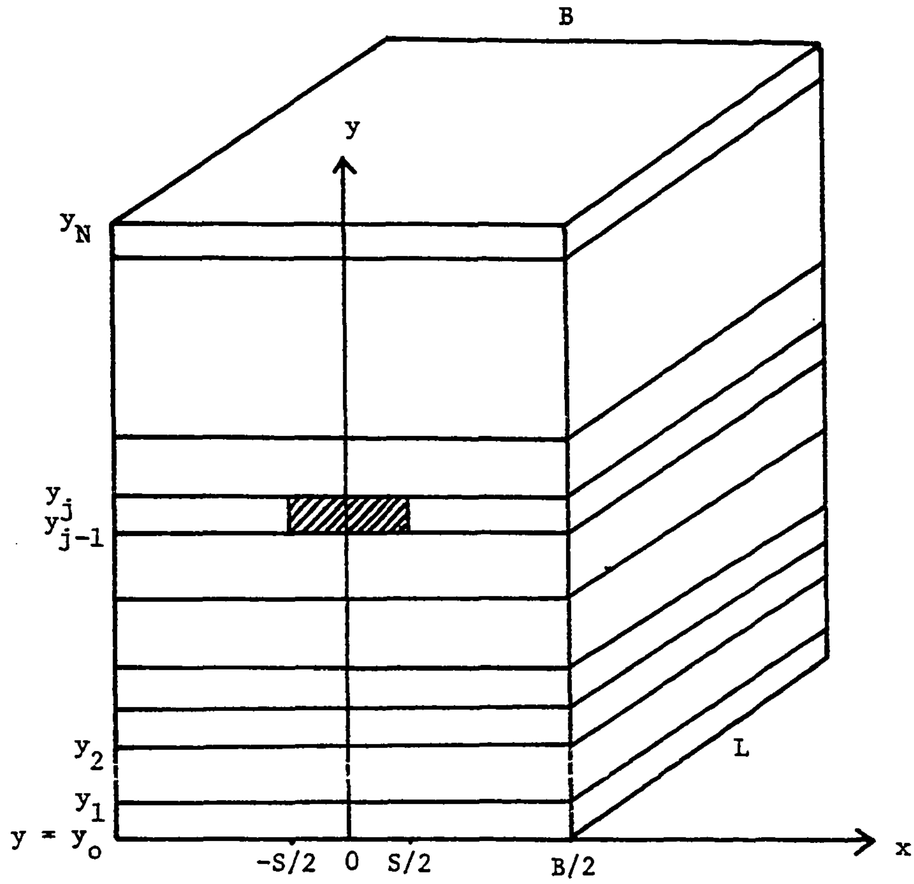

Fig. 2.5. Coordinate system used for heat equation

Table 2.1. Typical layer structure for modern stripe geometry GaAs/AlGaAs DH laser

Layer Number	Description	Composition	Typical Thickness (μm)	Thermal Conductivity (W/cm-°K)
1	Bonding	In	1 ~ 10	0.87
2	Solder contact	Au	0.1 ~ 10	3.18
3	p-contact	Pt	0.1	0.80
4	p-contact	Ti	0.1	0.22
5	Capping	p-GaAs	1 ~ 3	0.45
6	P-inactive	P-$Al_{0.3}Ga_{0.7}As$	0.8 ~ 2	0.14
7	Active	p-GaAs	0.1 ~ 0.3	0.45
8	N-inactive	N-$Al_{0.3}Ga_{0.7}As$	1 ~ 3	0.14
9	Substrate	n-GaAs	100	0.45
10	n-contact	GeAu	0.4 ~ 2	1.50

For convenience, $T_h = 0$ will be used to solve the heat equation.

2. Solution of the heat equation

In this section, the heat equation (2.27) is solved with the standard separation of variables technique. For steady-state condition, with the assumptions listed above, the heat equation becomes

$$\sigma\nabla^2 T = -Q_v \tag{2.27}$$

where σ, T and Q_v represent thermal conductivity, temperature, and the heat generated at the location. To solve (2.27), it is necessary to consider the homogeneous equation

$$\sigma_i \nabla^2 T_i = 0 \tag{2.28}$$

$$i = 1, 2, \ldots 10$$

where σ_i and T_i correspond to the thermal conductivity and temperature distribution at the ith layer. Given the assumption that $\partial T_i/\partial z = 0$, the variables can be separated such that

$$T_i(x,y) = X_i(x)\, Y_i(y) \tag{2.29}$$

Substituting (2.29) into (2.28) yields

$$X_i''\, Y_i + X_i\, Y_i'' = 0 \tag{2.30}$$

or

$$\frac{X_i''}{X_i} = -\frac{Y_i''}{Y_i} = -k^2 \tag{2.31}$$

Because of the symmetry, and also because of the boundary condition that $\partial T_i/\partial x = 0$ at $x = \pm B/2$, the functions of $X_i(x)$ and $Y_i(y)$ can be given as

$$X_i(x) = \cos(k_n x) \tag{2.32}$$

and

$$Y_i(y) = \cosh[k_n(y - y_{i-1})] \text{ or } \sinh[k_n(y - y_{i-1})] \tag{2.33}$$

respectively. Here $k_n = 2n\pi/B$ where n is an integer n = 1, 2, 3....

Thus, the complete solution for (2.28) yields

$$T_i(x,y) = \alpha_{i,0} + \beta_{i,0}(y - y_{i-1}) + \sum_{n=1}^{\infty} \{\alpha_{i,n} \cosh[k_n(y - y_i)] + \beta_{i,n} \sinh[k_n(y - y_i)]\} \cos(k_n x) \tag{2.34}$$

3. Determination of the Fourier coefficients

The coefficient α's and β's in (2.34) should be determined with assumed boundary conditions and the condition for the continuity of temperature and heat flow at each layer boundary. These are

$$T(x, y = y_o) = 0 \tag{2.35}$$

$$\frac{\partial T}{\partial y}(x, y = y_{10}) = 0 \tag{2.36}$$

$$T_i(y_i) = T_{i+1}(y_i) \tag{2.37}$$

$$\sigma_i \frac{\partial T_i(y_i)}{\partial y} = \sigma_{i+1} \frac{\partial T_{i+1}(y_i)}{\partial y} \qquad \text{for } i \neq j \tag{2.38}$$

$$\sigma_i \frac{\partial T_i(y_i)}{\partial y} = \sigma_{i+1} \frac{\partial T_{i+1}}{\partial y}(y_i) + Q \qquad \text{for } i = j \tag{2.39}$$

For the GaAs/AlGaAs laser model, $j = 7$ and $N = 10$. In Equation (2.39) Q is the intensity of the heat source in W/cm^2. For convenience, it is assumed that diode input power is P_d in the unit of W, i.e., $Q = P_d/SL$ for $|x| \leq S/2$ and $Q = 0$ elsewhere.

With Equations (2.35)-(2.39), the coefficients can be calculated. First consider

$$T_i(x,y_i) = \alpha_{i,0} + \beta_{i,o}(y_i - y_{i-1}) + \sum_{n=1}^{\infty} \{\alpha_{i,n} \cosh[k_n(y_i - y_{i-1})] + \beta_{i,n} \sinh[k_n(y_i - y_{i-1})]\} \cos(k_n x) \tag{2.40}$$

and

$$T_{i+1}(x,y_i) = \alpha_{i+1,0} + \sum_{n=1}^{\infty} \alpha_{i+1,n} \cos(k_n x) \tag{2.41}$$

Equating (2.40) and (2.41) according to (2.37) results in

$$\alpha_{i,0} + \beta_{i,0}\, d_i = \alpha_{i+1,0} \tag{2.42}$$

$$\alpha_{i,n} \cosh(k_n d_i) + \beta_{i,n} \sinh(k_n d_i) = \alpha_{i+1,n} \qquad \text{for } n \geq 1 \tag{2.43}$$

where $d_i = y_i - y_{i-1}$ is the thickness of the ith layer.

Next, consider the continuity of heat flow for the case of $i \neq j$.

$$\sigma_i \frac{\partial T_i}{\partial y}\bigg|_{y=y_i} = \sigma_i\beta_{i,0} + \sum_{n=1}^{\infty} [\sigma_i\alpha_{i,n}k_n \sinh(k_n d_i) + \sigma_i\beta_{i,n} k_n \cosh(k_n d_i)] \cos(k_n x) \tag{2.44}$$

$$\sigma_{i+1} \frac{\partial T_{i+1}}{\partial y}\bigg|_{y=y_i} = \sigma_{i+1}\beta_{i+1,0} + \sum_{n=1}^{\infty} \sigma_{i+1}\beta_{i+1,n} k_n \cos(k_n x) \tag{2.45}$$

Equating (2.44) and (2.45) yields, for $i \neq j$,

$$\sigma_i \beta_{i,0} = \sigma_{i+1} \beta_{i+1,0} \tag{2.46}$$

$$\sigma_i[\alpha_{i,n} \sinh(k_n d_i) + \beta_{i,n} \cosh(k_n d_i)] = \sigma_{i+1} \beta_{i+1,n} \quad n \geq 1 \tag{2.47}$$

For $i = 7$, the heat source intensity is represented as a Fourier series such that

$$Q = \begin{cases} P_d/SL & |x| \leq \frac{S}{2} \\ 0 & \frac{B}{2} \geq |x| > \frac{S}{2} \end{cases} \tag{2.48}$$

becomes

$$Q = \frac{P_d}{SL}\frac{S}{B} + \frac{4P_d}{SLB}\sum_{n=1}^{\infty} \frac{\sin(k_n S/2)}{k_n} \cos(k_n x) \text{ for } 0 \leq |x| \leq \frac{B}{2} \tag{2.49}$$

Using (2.39) and (2.49), for $i = j$

$$\sigma_i \beta_{i,0} = \sigma_{i+1} \beta_{i+1,0} + \frac{P_d}{LB} \tag{2.50}$$

$$\sigma_i [\alpha_{i,n}\, k_n \sinh(k_n\, d_i) + \beta_{i,n}\, k_n \cosh(k_n\, d_i)]$$

$$= \sigma_{i+1}\, \beta_{i+1,n}\, k_n + \frac{4P_d}{SLB} \frac{\sin(k_n S/2)}{k_n} \quad \text{for } n \geq 1 \tag{2.51}$$

Also, from the boundary conditions (2.35)

$$\alpha_{1,n} = 0 \qquad \text{for } n \geq 0 \tag{2.52}$$

The boundary condition (2.36)

$$\frac{\partial T_N}{\partial y} (x,\, y_N) = \beta_{N,0} + \sum_{n=1}^{\infty} [\alpha_{N,n}\, k_n \sinh(k_n\, d_N)$$

$$+ \beta_{N,n}\, k_n \cosh(k_n\, d_N)] \cos(k_n x) = 0 \quad \text{for all } x \tag{2.53}$$

reduces to

$$\beta_{N,0} = 0 \tag{2.54}$$

$$\alpha_{N,n} \sinh(k_n\, d_N) + \beta_{N,n} \cosh(k_n\, d_N) = 0 \quad \text{for } n \geq 1 \tag{2.55}$$

Using the Equations (2.42), (2.43), (2.46), (2.47), (2.50), (2.51), (2.52), and (2.55), it is possible to determine the Fourier coefficients.

First, (2.46), (2.50), and (2.54) yield

$$\beta_{N,0} = 0 \tag{2.54}$$

$$\beta_{i,0} = \begin{cases} \dfrac{P_d}{\sigma_i \; BL} & \text{for } 1 \le i \le j \qquad (2.56a) \\ 0 & \text{for } j < i \le N \qquad (2.56b) \end{cases}$$

From (2.42), (2.52), and (2.56),

$$\alpha_{i,0} = \frac{P_d}{BL} \sum_{m=1}^{\min(i-1,j)} \frac{d_m}{\sigma_m} \qquad (2.57)$$

Define $\gamma_{N,n}$ using (2.55), where $\gamma_{i,n} \equiv \beta_{i,n}/\alpha_{i,n}$

$$\gamma_{N,n} \equiv \frac{\beta_{N,n}}{\alpha_{N,n}} = -\tanh(k_n \; d_N) \qquad (2.58)$$

Substituting i = 1 into (2.47) gives

$$\beta_{2,n} \, \sigma_2 = \sigma_1[\alpha_{1,n} \sinh(k_n \; d_1) + \beta_{1,n} \cosh(k_n \; d_1)] \qquad (2.59)$$

Also, from (2.43),

$$\alpha_{2,n} = \alpha_{1,n} \cosh(k_n \; d_1) + \beta_{1,n} \sinh(k_n \; d_1) \qquad (2.60)$$

where $\alpha_{1,n} = 0$ in (2.59) and (2.60) because of (2.52). Dividing (2.59) by (2.60) yields

$$\gamma_{2,n} = \frac{\sigma_1}{\sigma_2} \coth(k_n \; d_1) \qquad (2.61)$$

Similarly, dividing (2.47) by (2.43) results in

$$\gamma_{i+1,n} = \frac{\sigma_i[\tanh(k_n \; d_i) + \gamma_{i,n}]}{\sigma_{i+1}[1 + \gamma_{i,n} \tanh(k_n \; d_i)]} \qquad (2.62)$$

Using (2.61) and (2.62), it is possible to determine from $\gamma_{2,n}$ up to $\gamma_{i-1,n}$. In the same way, $\gamma_{N,n}$ to $\gamma_{j,n}$ are found.

To find the coefficients $\alpha_{i,n}$, first rewrite Equation (2.51).

$$\sigma_i \; \alpha_{j,n}[\sinh(k_n \, d_j) + \gamma_{j,n} \cosh(k_n \, d_j)]$$

$$= \sigma_{j+1} \; \beta_{j+1,n} + \frac{4P_d}{SLB} \frac{\sin(k_n S/2)}{k_n^{\;2}} \tag{2.63}$$

Subtracting $\sigma_j \times$ (2.43) from (2.63) yields

$$\alpha_{j,n}[(\sigma_j - \sigma_j \gamma_{j,n}) \sinh(k_n \, d_j) + (\sigma_j \gamma_{j,n} - \sigma_j) \cosh(k_n \, d_j)]$$

$$= \alpha_{j+1,n}(\sigma_{j+1}\beta_{j+1,n} - \sigma_j) + \frac{4P_d}{SLB} \frac{\sin(k_n S/2)}{k_n^{\;2}} \tag{2.64}$$

Now, substitute $\alpha_{j+1,n}$ in (2.64) by (2.43) and solve for $\alpha_{j,n}$.

$$\alpha_{j,n} = \frac{4P_d \sin(k_n S/2)/SLB \; k_n^{\;2}}{(\sigma_j - \sigma_{j+1}\gamma_{j,n}\gamma_{j+1,n}) \sinh(k_n \, d_j) + (\sigma_j\gamma_{j,n} - \sigma_{j+1}\gamma_{j+1,n}) \cosh(k_n \, d_j)} \tag{2.65}$$

The remaining $\alpha_{i,n}$ are determined from (2.43) and (2.65).

4. Thermal resistance and temperature distribution

Because the heat equation (2.27) is a linear differential equation, it need not be solved for each driving current level. Therefore, it is convenient to define the thermal resistance of the laser as mentioned in Equation (1.3). The thermal resistance can be determined by

simply substituting $P_d = 1$ into the equations for Fourier coefficients. A typical solution is shown in Figures 2.6-2.8.

Two physical quantities are of interest here. One is the lateral temperature distribution in the active layer, and the other is average temperature rise in the active region. Therefore, define

$$R_1(x, y=y_j) = T_j(x, y=y_j)/P_d \tag{2.66}$$

and

$$R_2 = \frac{1}{S} \int_{-S/2}^{S/2} T_j(x, y=y_j)dx \tag{2.67}$$

For purposes of simplicity, R_2 was used as (2.67), to study the junction heating effects instead of a volume averaged temperature. R_1 is used to investigate the lateral thermal guiding effects. As discussed in Equation (1.2), P_d is considered substantial only for CW operation ($\chi = 1$) or heavy duty cycle pulsed operation. If the duty cycle χ is lower than 10^{-2}, the heat generated by the driving current is negligible.

The average junction temperature rise for CW operation ΔT_j according to (1.2), (1.3), and (2.67) is defined as

$$\Delta T_j = R_2 P_d \tag{2.68}$$

For the special case of threshold input it is

$$\begin{aligned} \Delta T_j^{th} &= R_2 P_d (I = I_{th}) \\ &= R_2 I_{th} V_j + R_2 I_{th}^2 r_s \end{aligned} \tag{2.69}$$

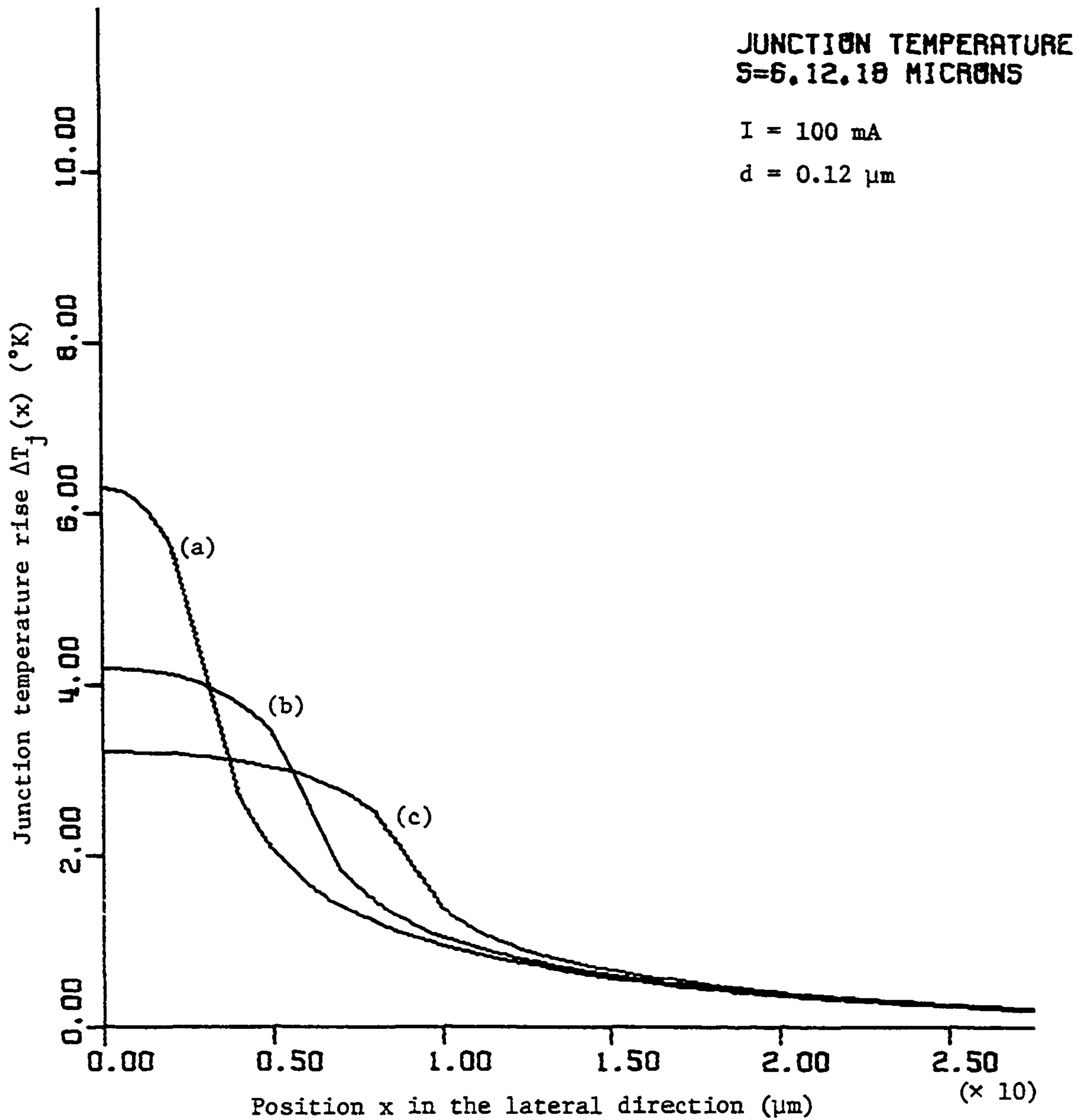

Fig. 2.6. Lateral thermal distribution for different stripe widths. (a) S = 6 μm (b) S = 12 μm (c) S = 18 μm

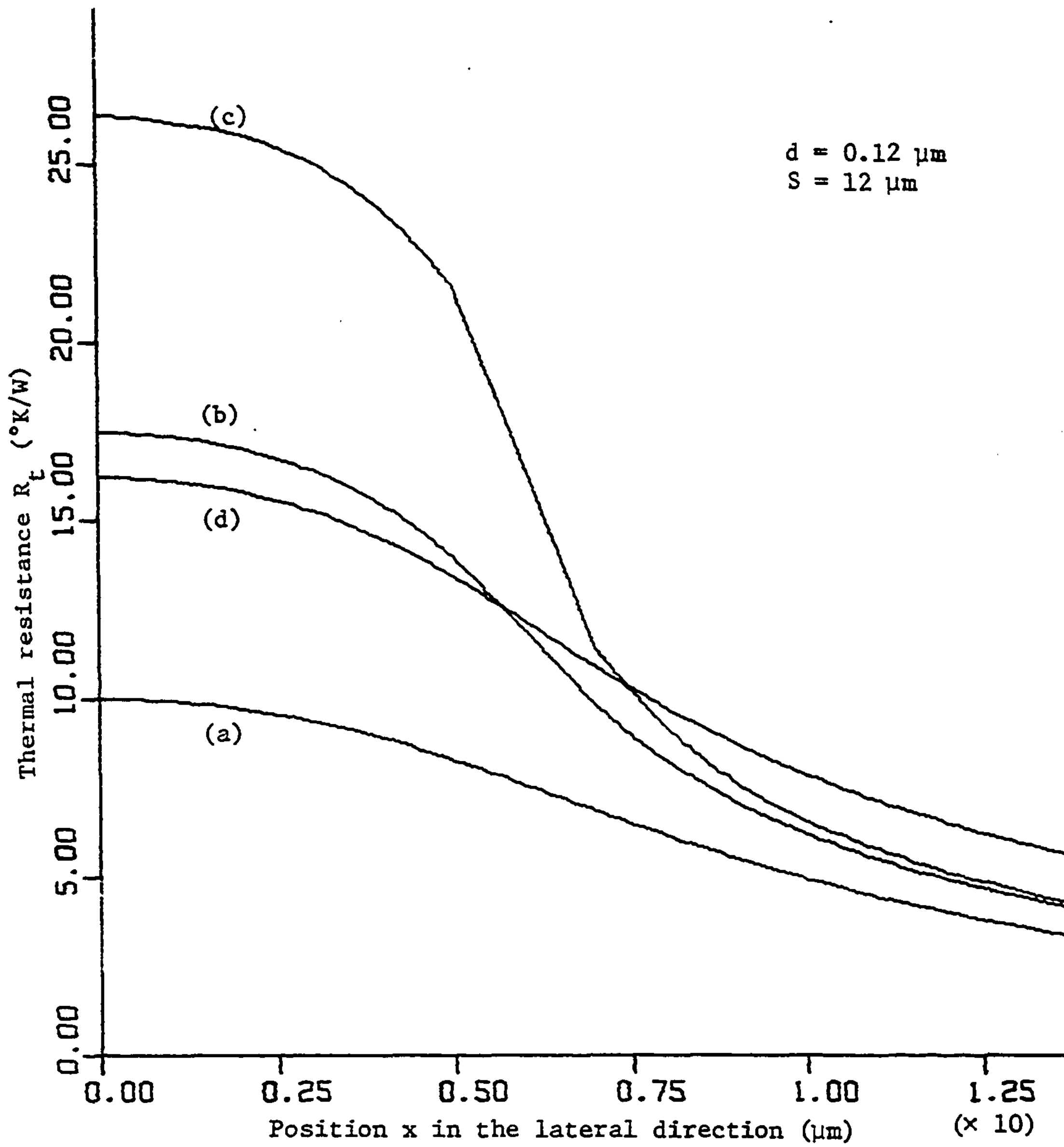

Fig. 2.7. Thermal resistance R_t in various layers. (a) at $y = y_2$ (b) at $y = y_5$ (c) at $y = y_7$ (d) at $y = y_8$

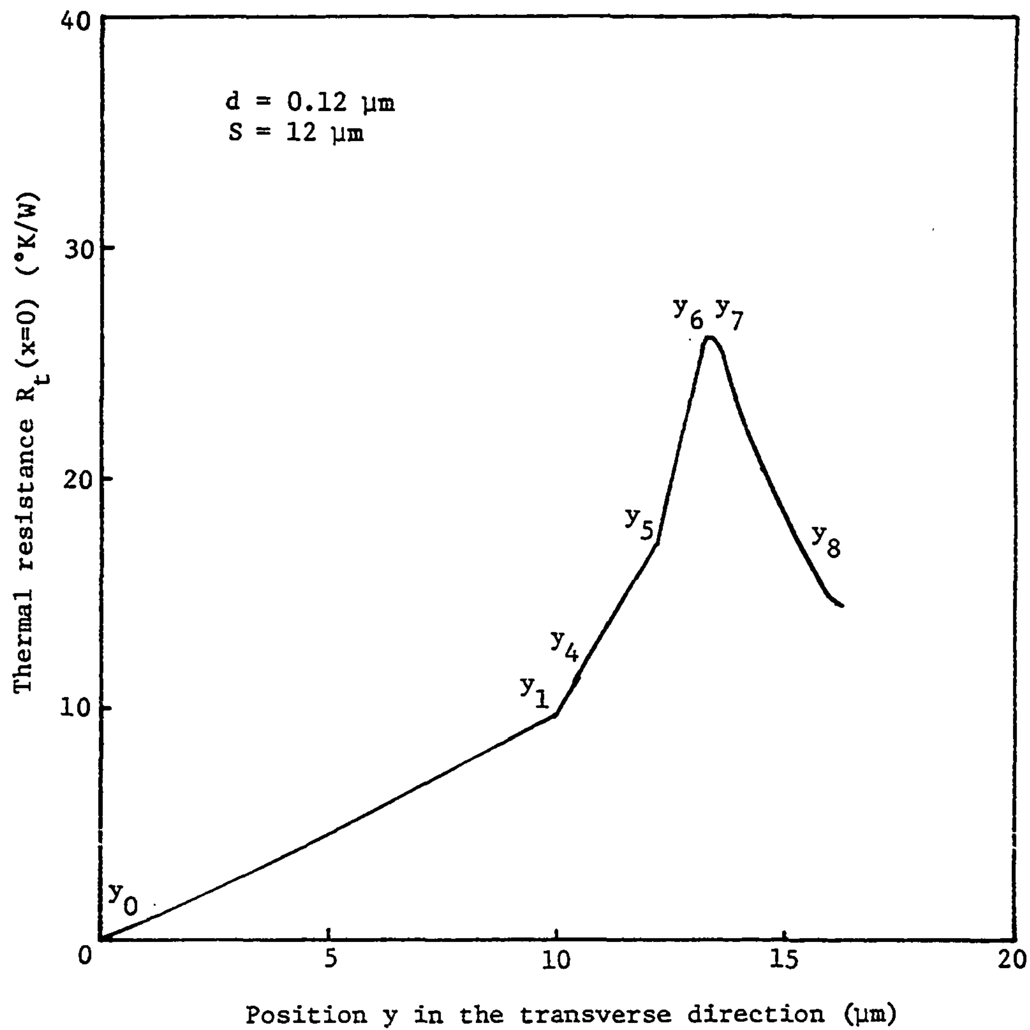

Fig. 2.8. Thermal resistance $R_t(x=0)$ in the transverse direction

where the joule loss term is usually very small in comparison to the first term in (2.69). Since the threshold current I_{th} and thermal resistance R_2 are strongly dependent on the structure, ΔT_j^{th} must be determined by the laser waveguide model along with the thermal distribution model. The results of calculated ΔT_j^{th} will be further discussed in section III.

C. Wave Equation in the Laser Cavity

This section investigates the solution of wave equation in the laser cavity. Optical field distribution in the dielectric slab waveguide is determined by Maxwell's equations [56,57]:

$$\nabla \times \vec{E} = -\frac{\partial \vec{B}}{\partial t} \tag{2.70}$$

and

$$\nabla \times \vec{H} = \frac{\partial \vec{D}}{\partial t} \tag{2.71}$$

Combining Equations (2.70) and (2.71) gives the wave equation

$$\nabla^2 \vec{E} = \mu\varepsilon \frac{\partial^2 \vec{E}}{\partial t^2} \tag{2.72}$$

or

$$\nabla^2 \vec{E} + k^2 \vec{E} = 0 \tag{2.73}$$

$$k^2 = \omega^2 \mu\varepsilon \tag{2.74}$$

for the time-harmonic case. Here, μ, ε, and k are magnetic permeability, dielectric permittivity, and wave number, respectively.

The dielectric constant ε_r in the slab waveguide can be described as

$$\varepsilon_r(x,y) = \begin{cases} \varepsilon_1(x) & \text{y in active layer} \\ \varepsilon_2(x) & \text{y in cladding layers} \end{cases} \quad (2.75)$$

The variation of dielectric constant in y direction is dictated by the refractive index difference between GaAs and AlGaAs. On the other hand, the dependence of ε_r in x direction is believed to stem from the gain and temperature distribution in the x direction.

Many different modes may propagate in such a three-layer dielectric slab waveguide. According to Ikegami [58], transverse electric modes usually dominate since these modes have a larger reflectivity at the cavity mirrors. Also, in a modern DH laser the active region is usually very thin so that the fundamental mode can only exist in the vertical direction. Therefore, only TE fundamental mode in the y direction is considered here.

1. Dielectric constant variation in the lateral direction

The complex index of refraction $\bar{n}_c$ of dielectric material is defined as [51]

$$\bar{n}_c = \bar{n} - j\bar{k} \quad (2.76)$$

where $\bar{n}$ and $\bar{k}$ are the real refractive index and the extinction coefficient, respectively. Consequently, the dielectric constants in each layer can be written as

$$\varepsilon_i(x) = (\bar{n}_i(x) - j\bar{k}_i(x))^2$$

$$\simeq \bar{n}_i^2(x) - 2j\bar{n}_i(x)\bar{k}_i(x) \qquad (2.77)$$

where i = 1 or 2. Also, the extinction coefficient $\bar{k}_i$ is related to the absorption coefficient α_i of the medium as

$$\bar{k}_i(x) = \frac{\lambda_o \alpha_i(x)}{4\pi} \qquad (2.78)$$

or

$$\bar{k}_i(x) = \frac{-\lambda_o g_i(x)}{4\pi} \qquad (2.79)$$

Here the gain coefficient $g_i(x) = -\alpha_i(x)$. Using the relation

$$k_o = \frac{2\pi}{\lambda_o} \qquad (2.80)$$

yields

$$\bar{k}_i(x) = \frac{-g_i(x)}{2k_o} \qquad (2.81)$$

and

$$\varepsilon_i(x) = \bar{n}_i^2(x) + j\bar{n}_i(x)g_i(x)/k_o \qquad (2.82)$$

The gain distribution in the active layer is proportional to the electron distribution [59,60] described earlier. That is,

$$g_1(x) = a_o\, n(x) - b_o \qquad \text{for } n \geq 1.28 \times 10^{18}\ \text{cm}^{-3} \qquad (2.83)$$
$$= c_o \qquad \text{for } n < 1.28 \times 10^{18}\ \text{cm}^{-3}$$

where a and b are empirically known as

$$a_o = 2.54 \times 10^{-16}\ \text{cm}^2$$
$$b_o = 424.0\ \text{cm}^{-1} \qquad (2.84)$$
$$c_o = -100.0\ \text{cm}^{-1}$$

Also in Equation (2.82), $g_2(x)$ represents the absorption in inactive layers.

$$g_2(x) = -\alpha_2 \qquad (2.85)$$

The refractive index $\bar{n}_1(x)$ is affected by both the electron distribution and the temperature gradient [40]. Injected electrons lower the refractive index of the active layer by two separate interactions. The first is the free-carrier-plasma interaction, which can be precisely calculated [51]. The second is a result of the gain process itself. Gain or loss processes with a pronounced spectral variation make a contribution to the refractive index of the material according to the Kramers-Kronig relations.

Paoli [61] and Buus [62] calculated the free-carrier contribution as

$$\delta\bar{n}_{fc} = -\frac{q^2\bar{n}}{2m_n\omega^2\varepsilon_r} \cdot \delta n \qquad (2.86)$$

or

$$\delta\bar{n}_{fc} \simeq -1.26 \times 10^{-21}\ (\mathrm{cm}^{-3}) \cdot \delta n \quad \text{for } \lambda_o = 0.9\ \mu\mathrm{m} \qquad (2.87)$$

Here m_n is the effective mass of the electron. The experimental values for $d\bar{n}/dn$ are in the same order of magnitude [63,64].

The temperature effect on the refractive index is experimentally known as [17,65,66]

$$\frac{d\bar{n}}{dT} \cong 4.9 \times 10^{-4}/°K \qquad (2.88)$$

From (2.87) and (2.88) the following is derived:

$$\bar{n}_1(x) = \bar{n}_1(0) + \frac{d\bar{n}}{dn}\{n(0) - n(x)\} + \frac{d\bar{n}}{dT}\{T(0) - T(x)\} \qquad (2.89)$$

where $\bar{n}_1(0)$ represents the refractive index in the active layer at the center of the strip ($x = 0$). With (2.89), the refractive index variation in the lateral direction may be calculated.

In the inactive layer, there is no electron concentration affecting the refractive index. Therefore, in these layers

$$\bar{n}_2(x) = \bar{n}_2(0) + \frac{d\bar{n}}{dT}\{T(0) - T(x)\} \qquad (2.90)$$

2. Parabolic approximation

The wave equation for a slab waveguide such as the one described in the last section is extremely difficult to solve. Frequently the gain and refractive index distribution are approximated with parabolic functions [67]. It should be pointed out, however, that this approximation method is only valid for the case where the optical intensity is well confined inside the stripe region. This is true for lasers

with a strip width greater than 6 μm. With this in mind, the parabolic approximation will be used in this work. Later, the solution of the wave equation with the approximation will be shown to be Hermite-Gaussian modes which have been experimentally observed [43,50].

It is assumed that the gain and refractive index in each layer can be written as

$$g_1(x) = g_1(0) - b^2x^2 \tag{2.91}$$

$$g_2(x) = -\alpha_2 \tag{2.92}$$

$$\bar{n}_1(x) = \bar{n}_1(0) - c^2x^2 \tag{2.93}$$

$$\bar{n}_2(x) = \bar{n}_2(0) - d^2x^2 \tag{2.94}$$

where g_1, g_2, $\bar{n}_1$, $\bar{n}_2$ represent the gain distribution in active and inactive layers, and the refractive index distribution in active and inactive layers, respectively. Figure 2.9 illustrates the assumed distributions.

3. Effective index approximation

As previously discussed, a common description of the lateral modes of a stripe-geometry laser uses the Hermite-Gaussian functions, while the transverse field dependence is dominated by the large steps of the heterojunctions. Only two methods have been proposed so far to tie together the lateral and transverse field dependencies under the stripe [68]. The first is the effective index method [61,62]; the second is the exact method [69].

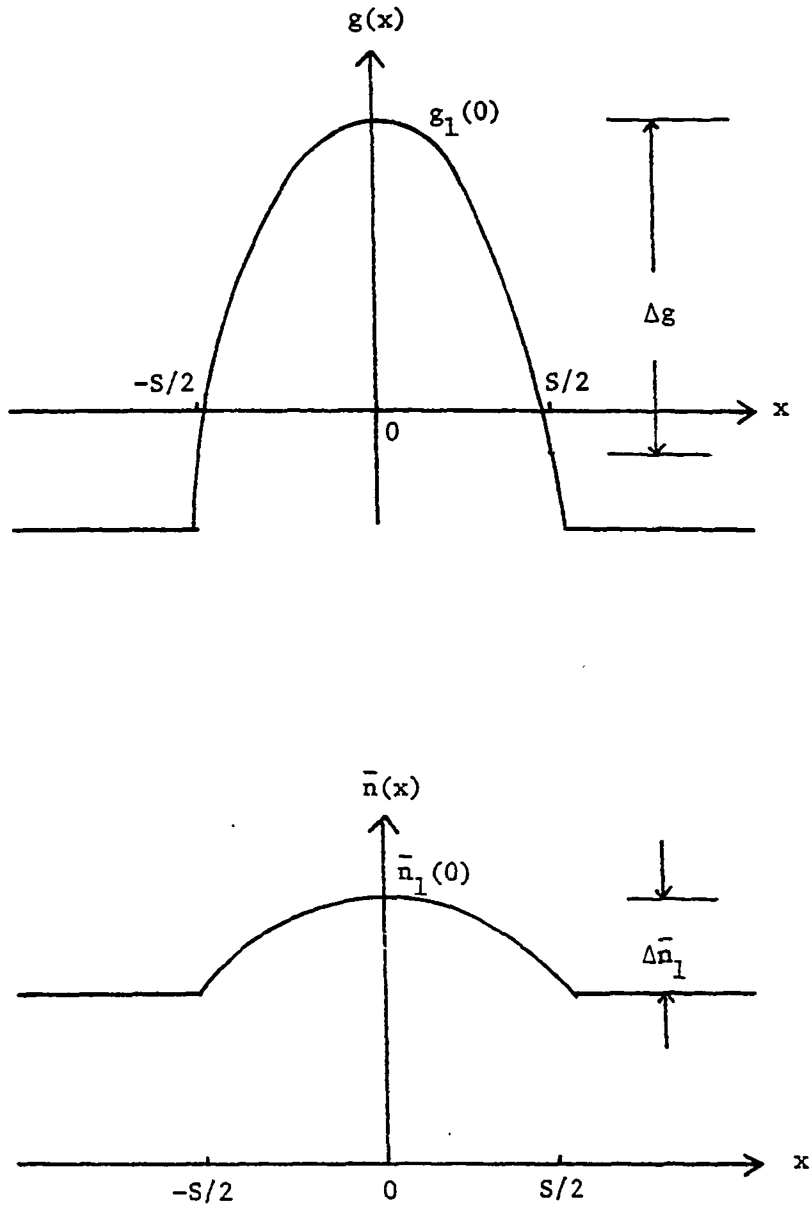

Fig. 2.9. Parabolic approximation of the gain and index variation in the lateral direction

The exact description of the lateral mode takes into account the vertical geometry by matching the field quantities at the hetero-boundaries. The result is a lateral mode description by a linear combination of Hermite-Gaussian functions with appropriate weighting coefficients.

On the other hand, the effective index method results in a single term lateral field description with appropriate "effective" parameters derived to account for the influence of the cladding layers on the lateral mode shape.

The effective index method is used in this model for two reasons. First, the model has already employed other approximations including the parabolic gain and refractive index distribution so that the fine accuracy of the solution is not critical to the waveguide solution. Second, the exact solution is almost identical with the effective solution in thermal guiding situations.

We start with the wave equation (2.73) and the dielectric constant (2.75). That is, for TE modes,

$$\nabla^2 \vec{E}_x(x,y,z) + k^2(x,y)\, \vec{E}_x(x,y,z) = 0 \tag{2.73}$$

$$\begin{aligned} k^2 &= \omega^2 \mu \varepsilon(x,y) \\ &= k_o^{\,2}\, \varepsilon_r(x,y) \end{aligned} \tag{2.74}$$

where, again,

$$\varepsilon_r(x,y) = \begin{cases} \varepsilon_1(x) & \text{y in active layer} \\ \varepsilon_2(x) & \text{y in inactive layer} \end{cases} \tag{2.75}$$

Since a rigorous solution to the wave equation (2.73) is not available, the following approximation is necessary.

Assume that the solution takes the form

$$\vec{E}_x(x,y,z) = \psi(x)\phi(y)\ \exp(-j\beta_z z) \tag{2.95}$$

Also, the dielectric constant varies much more slowly in the x direction compared to the heterojunction steps in the y direction. Therefore, it is assumed that the modal distribution $\phi(y)$ is not appreciably affected by the confinement along x. In this case, $\phi(y)$ satisfies

$$\frac{d^2\phi(y)}{dy^2} + \beta_y{}^2\ \phi(y) = 0 \tag{2.96}$$

Substituting (2.95) into (2.73), gives

$$\frac{d^2\psi(x)}{dx^2}\ \phi(y) + \frac{d^2\phi(y)}{dy^2}\ \psi(x) + \varepsilon_r(x,y)\ k_o{}^2\psi(x)\phi(y) - \beta_z{}^2\psi(x)\phi(y) = 0 \tag{2.97}$$

Again, substituting (2.96) into (2.97) yields

$$\phi(y)\ \frac{d^2\psi(x)}{dx^2} + \{\varepsilon_r(x,y)k_o{}^2 - \beta_z{}^2 - \beta_y{}^2\}\ \psi(x)\phi(y) = 0 \tag{2.98}$$

To accommodate the variation in y, multiply $\phi^*(y)$ to equation (2.98) and integrate over y, using Equation (2.75):

$$\int_{-\infty}^{\infty} \phi\, \phi^* \, dy \, \frac{d^2\psi(x)}{dx^2} + \int_{\substack{\text{active}\\ \text{layer}}} [\varepsilon_1(x)k_o^2 - \beta_y^2 - \beta_z^2]\, \phi\, \phi^* \, dy\, \psi(x)$$

$$+ \int_{\substack{\text{outside}\\ \text{active}\\ \text{layer}}} [\varepsilon_2(x)\, k_o^2 - \beta_y^2 - \beta_z^2]\, \phi\, \phi^* \, dy\, \psi(x) = 0 \qquad (2.99)$$

Dividing both sides of the Equation (2.98) by $\int_{-\infty}^{\infty} \phi\, \phi^* \, dy$, gives

$$\frac{d^2\psi(x)}{dx^2} + [\Gamma\varepsilon_1(x)k_o^2 + (1 - \Gamma)\varepsilon_2(x)k_o^2 - \beta_y^2 - \beta_z^2]\, \psi(x) = 0$$

(2.100)

where the confinement factor Γ is defined as

$$\Gamma = \frac{\int_{o}^{d} \phi(y)\phi^*(y)dy}{\int_{-\infty}^{\infty} \phi(y)\phi^*(y)dy} \qquad (2.101)$$

The values of Γ for transverse fundamental modes are shown in Figure 2.10 for GaAs/$Al_xGa_{1-x}As$ DH lasers [70].

The "Effective dielectric constant" $\varepsilon_{eff}(x)$ is defined as

$$\varepsilon_{eff}(x) = \Gamma\varepsilon_1(x) + (1 - \Gamma)\varepsilon_2(x) \qquad (2.102)$$

Then, Equation (2.100) is equivalent to

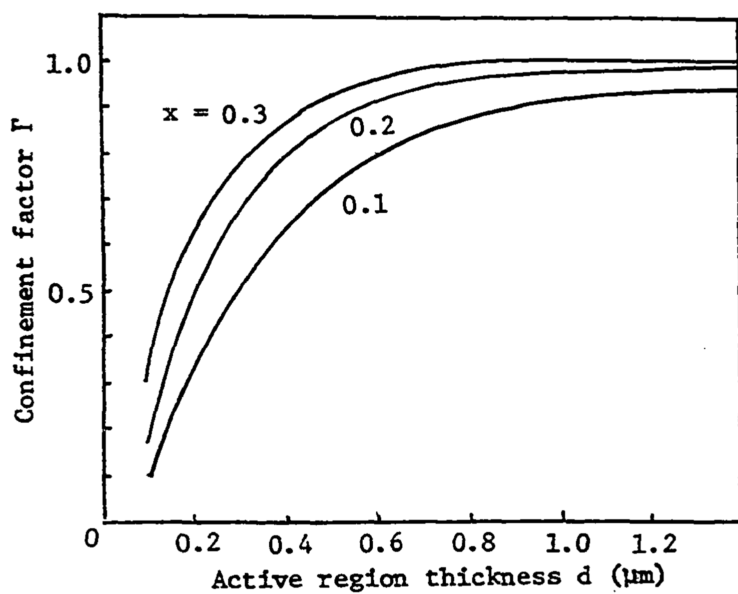

Fig. 2.10. Γ against d for the fundamental mode in the $GaAs/Al_xGa_{1-x}As$ symmetrical DH laser for several values of x [70]

$$\frac{d^2\psi(x)}{dx^2} + [k_o{}^2\varepsilon_{eff}(x) - \beta_y{}^2 - \beta_z{}^2]\ \psi(x) = 0 \qquad (2.103)$$

The effective dielectric constant can be determined by substituting (2.82) and (2.91)-(2.94) into (2.102).

$$\begin{aligned}\varepsilon_{eff} &= \Gamma\varepsilon_1(x) + (1 - \Gamma)\varepsilon_2(x)\\ &= \Gamma[\bar{n}_1(0) - c^2x^2]^2 + \frac{j}{k_o}\Gamma[\bar{n}_1(0) - c^2x^2]\ [g_1(0) - b^2x^2]\\ &\quad + (1 - \Gamma)[\bar{n}_2(0) - d^2x^2]^2 + \frac{j}{k_o}(1 - \Gamma)\ [\bar{n}_2(0) - d^2x^2]\ g_2\\ &= \Gamma\bar{n}_1{}^2(0) + (1 - \Gamma)\bar{n}_2{}^2(0) - x^2[2\Gamma\bar{n}_1(0)c^2 + 2(1 - \Gamma)\bar{n}_2(0)d^2]\\ &\quad + x^4[\Gamma c^4 + (1 - \Gamma)d^4]\\ &\quad + \frac{j}{k_o}[\Gamma\bar{n}_1(0)g_1(0) + (1 - \Gamma)\bar{n}_2(0)g_2(0)]\\ &\quad - \frac{j}{k_o}x^2\ \{\Gamma[c^2g_1(0) + b^2\bar{n}_1(0)] + (1 - \Gamma)g_2d^2\}\\ &\quad + \frac{j}{k_o}x^4\ \Gamma\ b^2\ c^2 \end{aligned} \qquad (2.104)$$

Equation (2.104) can be simplified as

$$\varepsilon_{eff}(x) = \varepsilon_{eff}(0) - a_{eff}^2\ x^2 \qquad (2.105)$$

where $a_{eff} = a_r + i\ a_i$ is a complex parameter determined from (2.104). The terms $O(x^4)$ are discarded because they are negligible when compared to the $O(x^2)$ terms.

For instance, compare the terms in the real part of (2.104):

$$\frac{\Gamma c^4 x^4}{2\Gamma \bar{n}_1(0)\ c^2 x^2} = \frac{c^2 x^2}{2\bar{n}_1(0)} \tag{2.106}$$

From the parabolic approximation, $c^2 = 4\Delta\bar{n}_1/S^2$ or

$$c^2 = \frac{4[\bar{n}_1(0) - \bar{n}_1(S/2)]}{S^2} \tag{2.107}$$

(2.106) becomes,

$$\frac{c^2 x^2}{2\bar{n}_1(0)} = \frac{4[\bar{n}_1(0) - \bar{n}_1(S/2)]x^2}{2\bar{n}_1(0)\ S^2} \tag{2.108}$$

Here, $\bar{n}_1(0) \simeq 3.6$,

$\bar{n}_1(0) - \bar{n}_1(S/2) \simeq 10^{-3}$,

and $x^2 \lesssim S^2$ yield

$$\frac{\Gamma c^4 x^4}{2\Gamma \bar{n}_1(0)\ c^2 x^2} << 1 \tag{2.109}$$

In the same way, it can be shown that

$$\frac{(1 - \Gamma)\ d^4 x^4}{2(1 - \Gamma)\bar{n}_2(0)\ d^2 x^2} << 1 \tag{2.110}$$

Also, for the imaginary part of (2.104)

$$\frac{\Gamma\, b^2\, c^2\, x^4}{\Gamma\, b^2\, \bar{n}_1(0)\, x^2} = \frac{c^2\, x^2}{\bar{n}_1(0)} << 1 \tag{2.111}$$

We now find the parameters a_r and a_i from (2.104) and (2.105).

$$\begin{aligned} a_{eff}^2 &= (a_r + j\, a_i)^2 \\ &= 2[\Gamma \bar{n}_1(0)c^2 + (1 - \Gamma)\bar{n}_2(0)d^2] \\ &\quad + \frac{j}{k_o} \{\Gamma[c^2 g_1(0) + b^2 \bar{n}_1(0)] + (1 - \Gamma)g_2 d^2\} \end{aligned} \tag{2.112}$$

Equating the real and imaginary parts of the left and right hand sides in (2.112) results in

$$a_r{}^2 - a_i{}^2 = 2[\Gamma\, \bar{n}_1(0)c^2 + (1 - \Gamma)\, \bar{n}_2(0)d^2] \tag{2.113}$$

$$2a_r a_i = \frac{1}{k_o} \{\Gamma[c^2 g_1(0) + \bar{n}_1(0)b^2] + (1 - \Gamma)g_2 d^2\} \tag{2.114}$$

Solving (2.113) and (2.114) for a_r gives

$$\begin{aligned} a_r{}^2 &= \Gamma\, \bar{n}_1(0)c^2 + (1 - \Gamma)\, \bar{n}_2(0)d^2 \\ &\quad + \{[\Gamma\, \bar{n}_1(0)c^2 + (1 - \Gamma)\, \bar{n}_2(0)d^2]^2 \\ &\quad + \frac{1}{k_o{}^2} [\Gamma\, c^2 g_1(0) + \Gamma\, \bar{n}_1(0)b^2 + (1 - \Gamma)g_2 d^2]^2\}^{1/2} \end{aligned} \tag{2.115}$$

For CW operation,

$$b^2 = \frac{4\Delta g}{S^2} \tag{2.116}$$

$$c^2 = \frac{4(\Delta\bar{n}_e + \Delta\bar{n}_t)}{S^2} \tag{2.117}$$

and

$$d^2 = \frac{4\Delta\bar{n}_t}{S^2} \tag{2.118}$$

For low duty cycle ($\chi \simeq 0$) pulsed operation,

$$\Delta\bar{n}_t = 0 \tag{2.119}$$

For (2.116)-(2.119),

$$\Delta g = g_1(0) - g_1(S/2) \tag{2.120}$$

$$\Delta\bar{n}_e = \frac{d\bar{n}}{dn}\,[n(0) - n(S/2)] \tag{2.121}$$

$$\Delta\bar{n}_t = \frac{d\bar{n}}{dT}\,[T_j(0) - T_j(S/2)] \tag{2.122}$$

are defined.

The effective dielectric constant can also be represented as

$$\varepsilon_{eff}(x) = \bar{n}^2_{eff}(x) + \frac{j}{k_o}\,\bar{n}_{eff}(x)\,\bar{k}_{eff}(x) \tag{2.123}$$

where

$$\bar{n}_{eff}(x) = \bar{n}_{eff}(0) - \frac{4\Delta\bar{n}_{eff}}{S^2} x^2 \tag{2.124}$$

Equating (2.104) and (2.124) with (2.117) and (2.118),

$$\begin{aligned} \Delta\bar{n}_{eff} &= \Gamma(\Delta\bar{n}_e + \Delta\bar{n}_t) + (1 - \Gamma) \frac{\bar{n}_2(0)}{\bar{n}_1(0)} \Delta n_t \\ &= \Delta\bar{n}_t \left\{ \frac{\bar{n}_2(0)}{\bar{n}_1(0)} + \Gamma \left[1 - \frac{\bar{n}_2(0)}{\bar{n}_1(0)} \right] \right\} + \Gamma \Delta\bar{n}_e \end{aligned} \tag{2.125}$$

It is interesting to note that

$$\Delta\bar{n}_{eff} \simeq \Delta\bar{n}_t + \Gamma \Delta\bar{n}_e \tag{2.126}$$

for the case of $\bar{n}_1(0) \simeq \bar{n}_2(0)$.

4. Solution of the wave equation

The wave equation (2.103) with (2.105) reduces to

$$\frac{d^2\psi(x)}{dx^2} + [k_o{}^2\varepsilon_{eff}(0) - k_o^2 a_{eff}^2 x^2 - \beta_y{}^2 - \beta_z{}^2]\, \psi(x) = 0 \tag{2.127}$$

The solution of (2.127) with the parabolic dielectric constant are known as Hermite-Gaussian functions [61,67]. The Hermite-Gaussian functions are well-known as the eigenfunctions of the time-independent Schrödinger equation for a harmonic oscillator [71,72]. That is,

$$\psi_n(x) = C_n\, H_n(k_o{}^{1/2} a_{eff}^{1/2}\, x) \exp(- \tfrac{1}{2}\, k_o a_{eff}\, x^2) \tag{2.128}$$

where C_n is the normalization constant to be determined yet, and the Hermite polynomial H_n is written as

$$H_n(\xi) = \frac{\partial^n}{\partial s^n}\left[e^{\xi^2-(s-\xi)^2}\right]\Bigg|_{s=0}$$

$$= e^{\xi^2} (-1)^n \frac{d^n}{d\xi^n} e^{-\xi^2} \tag{2.129}$$

Applying (2.129) to generate, as an example, the first three H_n's gives:

$$H_o(\xi) = 1, \tag{2.130}$$

$$H_1(\xi) = 2\xi, \tag{2.131}$$

and

$$H_2(\xi) = 4\xi^2 - 2. \tag{2.132}$$

The derivation of the solution (2.128) is further discussed in Appendix (C).

The wave equation in the y direction is solved from (2.96). The fundamental mode solution takes the form

$$\phi_o(y) = \begin{cases} \cos[p(y - \frac{d}{2})] & \text{for } 0 \le y \le d \\ \cos(p\,\frac{d}{2})\,\exp(-q|y|) & \text{for } y < 0 \\ \cos(p\,\frac{d}{2})\,\exp[-q(y - d)] & \text{for } y > d \end{cases} \tag{2.133}$$

The quantities p and q are the eigenvalues of the slab waveguide boundary value problem.

The mode intensities which are proportional to $|\psi_n|^2$ are illustrated in Figure 2.11.

5. Mode gain, near- and far-field pattern

Since the fundamental mode in both a lateral and transverse direction is of primary interest, the mode gain G_{oo} of such a mode must first be found. Here G_{mn} is defined as the mode gain of mth transverse and nth lateral mode.

$$G_{oo} = \frac{\int_{-\infty}^{\infty} \int_{-\infty}^{\infty} g(x,y) \, |E_x|^2 \, dx \, dy}{\int_{-\infty}^{\infty} \int_{-\infty}^{\infty} |E_x|^2 \, dx \, dy} \tag{2.134}$$

or

$$G_{oo} = \Gamma \frac{\int_{-\infty}^{\infty} g_1(x) \, |\psi_o(x)|^2 \, dx}{\int_{-\infty}^{\infty} |\psi_o(x)|^2 \, dx} - (1 - \Gamma)\alpha_2 \tag{2.135}$$

The threshold condition is that the mode gain matches the optical loss in the cavity [73]. That is,

$$G_{oo} = \frac{1}{L} \ln \frac{1}{R} \tag{2.136}$$

where R is the mode reflectivity at the facet.

Now the lateral mode gain G_n^{ℓ} is also defined as

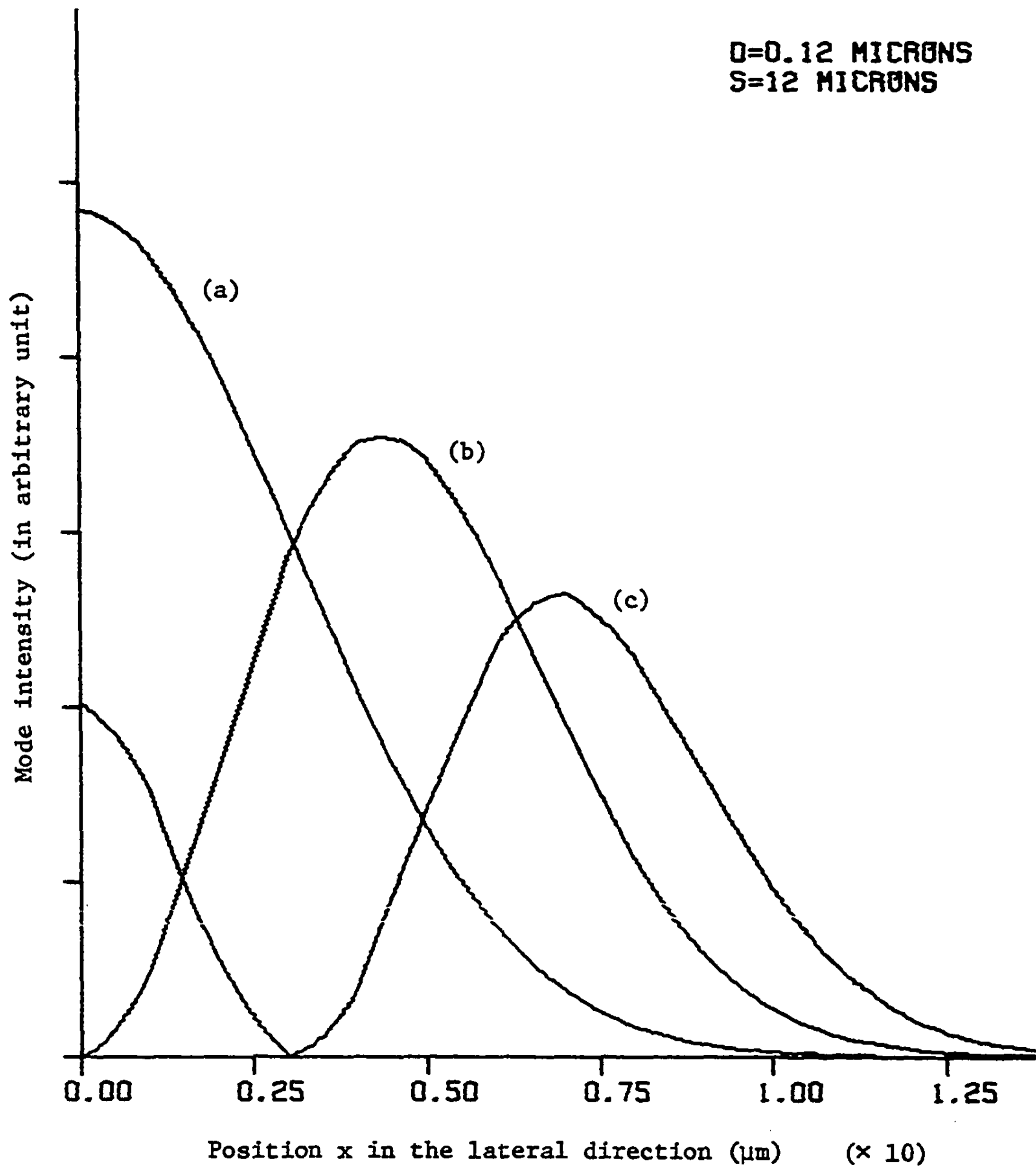

Fig. 2.11. First three lateral mode intensity profiles obtained from Hermite-Gaussian eigenfunctions. (a) zeroth-order (b) first-order (c) second-order

$$G_n^{\ell} = \frac{\int_{-\infty}^{\infty} g_1(x) \, |\psi_n(x)|^2 \, dx}{\int_{-\infty}^{\infty} |\psi_n(x)|^2 \, dx} \tag{2.137}$$

For the fundamental lateral mode,

$$G_o^{\ell} = \frac{\int_{-\infty}^{\infty} g_1(x) \, |\psi_o(x)|^2 \, dx}{\int_{-\infty}^{\infty} |\psi_o(x)|^2 \, dx} \tag{2.138}$$

where the normalized eigenfunction ψ_o is

$$\psi_o = \sqrt{\frac{k_o a_r}{\pi}} \exp(-\tfrac{1}{2} k_o \, a_{eff} \, x^2) \tag{2.139}$$

Substituting (2.139) into (2.138), and using (2.91) and (2.116) for $g_1(x)$,

$$\begin{aligned} G_o^{\ell} &= \int_{-\infty}^{\infty} \left[g_1(0) - \frac{4\Delta g}{S^2} x^2 \right] \frac{k_o a_r}{\pi} \exp(-k_o a_r \, x^2) \, dx \\ &= g_1(0) - \frac{2\Delta g}{S^2 k_o a_r} \end{aligned} \tag{2.140}$$

Similarly,

$$\psi_1(x) = \frac{k_o \, a_{eff}^{1/2} \, a_r^{3/2}}{|a_{eff}| \, \sqrt{\pi}} \, x \exp(-\tfrac{1}{2} k_o \, a_{eff} \, x^2) \tag{2.141}$$

$$G_1^{\ell} = g_1(0) - \frac{6\Delta g}{S^2 \, k_o \, a_r} \tag{2.142}$$

The threshold condition (2.136) can also be expressed, using (2.135) for nth lateral mode, as

$$\Gamma\, G_n^{\ell} - (1 - \Gamma)\alpha_2 = \frac{1}{L}\,\ell n\,\frac{1}{R} \tag{2.143}$$

or

$$G_n^{\ell} = [(1 - \Gamma)\alpha_2 + \frac{1}{L}\,\ell n\,\frac{1}{R}]/\Gamma \tag{2.144}$$

Consequently, the lowest driving current which injects enough electrons to meet the condition (2.144) is the threshold current of the device.

Next, consider the radiation patterns. The lateral optical distribution in the laser A(x) for the fundamental mode is

$$\begin{aligned} A(x) &= A_o \left|\psi_o(x)\right|^2 \\ &= A_o \exp(-\tfrac{1}{2}\, k_o\, a_{eff}\, x^2) \exp(-\tfrac{1}{2}\, k_o\, a_{eff}^{*}\, x^2) \\ &= A_o \exp(-k_o\, a_r\, x^2) \end{aligned} \tag{2.145}$$

The near-field half-power full-width, W_h, is defined as the full width of half power points of the intensity, i.e.,

$$A(\tfrac{1}{2}\, W_h) = \tfrac{1}{2}\, A_o \tag{2.146}$$

For the Gaussian mode,

$$\exp\left[-k_o\, a_r \left(\frac{W_h}{2}\right)^2\right] = \frac{1}{2} \tag{2.147}$$

or

$$W_h = 2 \left(\frac{\ln 2}{k_o\ a_r}\right)^{1/2} \tag{2.148}$$

Also, W_e can be defined as the width of $1/e^2$ intensity points, or

$$\exp\left[-k_o\ a_r \left(\frac{W_e}{2}\right)^2\right] = \exp(-2) \tag{2.149}$$

or

$$W_e = 2 \left(\frac{2}{k_o\ a_r}\right)^{1/2} \tag{2.150}$$

In the case of the Gaussian mode,

$$W_e = 1.7\ W_h \tag{2.151}$$

The far-field intensity pattern $B(\theta)$ can easily be determined by the relation

$$B(\theta) = f(\theta) \left| \int_{-\infty}^{\infty} \psi_o(x) \exp(-ik_o x \sin\theta) dx \right|^2 \tag{2.152}$$

where $f(\theta) \simeq \cos\theta$ is the Huygen's obliquity factor [70], and θ is the angle between the z-axis and the observation direction in the junction plane. For small θ, $f(\theta) \simeq 1$ is valid. Therefore, for small angle θ,

$$B(\theta) \simeq \left| \int_{-\infty}^{\infty} \sqrt{\frac{k_o a_r}{\pi}} \exp(-\tfrac{1}{2}\, k_o\ a_{eff}\ x^2 - ik_o x \sin\theta) dx \right|^2$$

$$= \left| \sqrt{\frac{2a_r}{a_{eff}}} \exp\left(\frac{-k_o \sin^2\theta}{2a_{eff}}\right) \right|^2$$

$$= \frac{2a_r}{|a_{eff}|} \exp\left[- \frac{k_o \sin^2\theta}{2} \left(\frac{1}{a_{eff}} + \frac{1}{a^*_{eff}}\right)\right] \tag{2.153}$$

The full angle at half power, θ_h, is derived from (2.153),

$$\exp\left[- \frac{k_o \sin^2\left(\frac{1}{2}\theta_h\right)}{2} \frac{2a_r}{|a_{eff}|^2}\right] = \frac{1}{2} \tag{2.154}$$

or

$$\theta_h = 2 \sin^{-1}\left(\frac{|a_{eff}|^2 \ln 2}{k_o a_r}\right)^{1/2} \tag{2.155}$$

The results of near- and far-field patterns will be further discussed in the following section.

III. RESULTS AND DISCUSSION

The model discussed in the previous sections was used to investigate nonuniform temperature effects on the performance of the laser. On the basis of the model, a computer program was developed using the WATFIV language. The input data of the program include the dimensions of the laser cavity, stripe width, thickness and thermal conductivity of each layer, and the input driving current. As summarized in Figure 1.7, the output of the model includes the thermal distribution in the laser and the waveguiding parameters.

In this section, some of the results are presented along with the previously reported experimental data.

A. Junction Temperature Effects on the Performance of the Laser

1. Effect on waveguiding

The near-field intensity distribution of a guided mode is determined by the parameter a_r as derived in Equation (2.145). Because the parameter a_r depends on the gain and refractive index distribution, and also on the active region temperature distribution, the near-field intensity differs between CW and pulsed operation. Figure 3.1 illustrates the typical near-field patterns of the lateral fundamental mode at different operating conditions.

Figure 3.1 indicates the index focusing of the lateral modes which results from the thermal gradient in the lateral direction for CW operation. This was experimentally observed by Paoli [61]. Figure 3.1 also shows an index defocusing of the modes for pulsed operation in

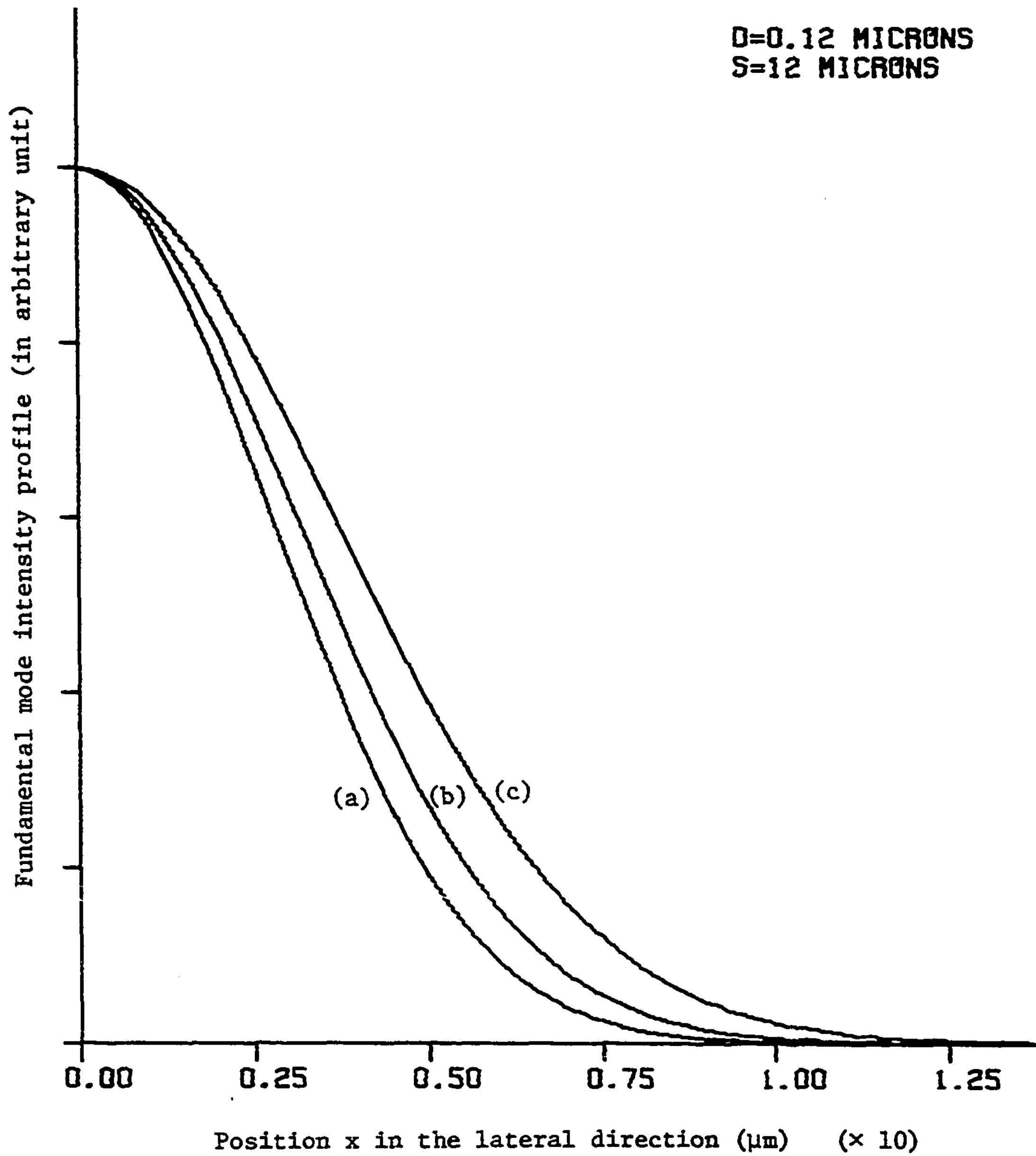

Fig. 3.1. Fundamental mode intensity profiles for different operating conditions. (a) CW operation (b) gain-guiding only (c) low duty cycle pulsed operation

Table 3.1. Parameters used in the model

Parameter	Value
λ_o	0.9 μm
R_s	10^7 Ω
L_a	3.4 μm
τ_n	2.8 ns
$d\bar{n}/dT$	4.9×10^{-4} °K^{-1}
$d\bar{n}/dn$	-1.26×10^{-21} cm^{-3}
$\alpha_2 = -g_2$	20.0 cm^{-1}
R	0.3
V_j	1.6 V

Table 3.2. Default values for laser dimensions. Unless otherwise specified, the following are used for calculation

Layer thickness (in μm)	d_1	10.0
	d_2	0.1
	d_3	0.1
	d_4	0.1
	d_5	2.0
	d_6	1.0
	$d_7 = d$	0.12
	d_8	2.0
	d_9	100.0
	d_{10}	0.2
Dimension (in μm)	S	12.0
	L	380.0
	B	300.0

comparison to the purely gain-guiding case. This is caused by the dip in the refractive index profile which results from the electron concentration distribution. The pulsed-operation index defocusing was originally observed by Cook and Nash [67].

Figure 3.2 shows the effect of the index focusing and defocusing on the near-field half-power full-width, W_h, of the fundamental mode. In calculating Figure 3.2, the hole burning effect was not taken into account. The above threshold property will be further discussed later in this section. According to the calculation, W_h for CW operation is about 2 μm smaller than for pulsed operation. This indicates that the radiation pattern can change significantly depending on the operational condition.

In order to investigate the significance of index-guiding in a gain-guiding laser, the guiding parameter R_g is defined as

$$R_g = \frac{\Delta\bar{n}_{eff}}{\Delta g} \tag{3.1}$$

where $\Delta\bar{n}_{eff}$ and Δg are defined by (2.125) and (2.120), respectively. When the gain at the center of the stripe region is higher than it is at the edge region, or $\Delta g > 0$, a positive R_g represents the refractive index focusing of the guided modes. A negative R_g indicates the refractive index anti-guiding which widens the modal shape, as illustrated in Figure 3.1.

As derived in the previous section, W_h for the lateral fundamental mode is expressed as

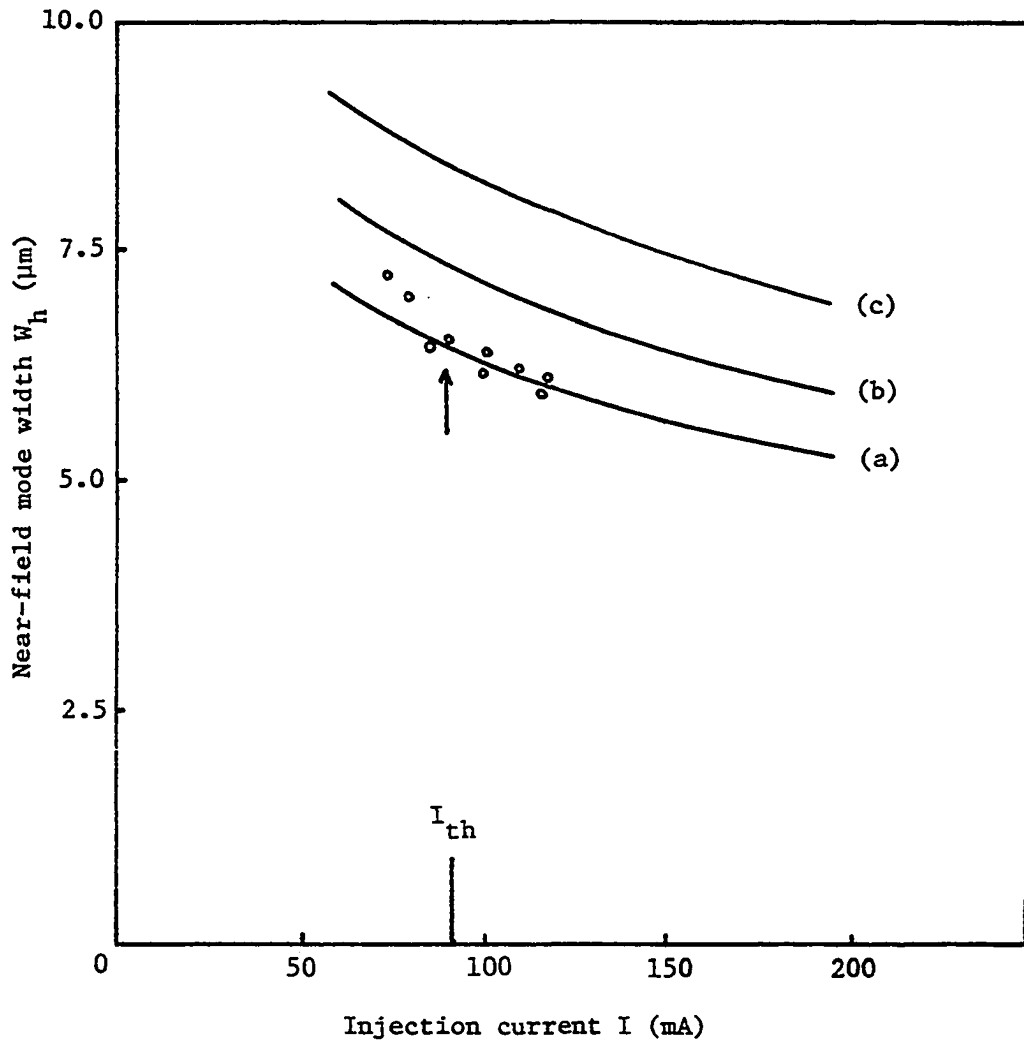

Fig. 3.2. Calculated near-field mode width W_h. (a) CW operation (b) gain-guiding only (c) pulsed operation. Circles represent CW experimental data from [61]

$$W_h = 2\left(\frac{\ell n\ 2}{k_o\ a_r}\right)^{1/2} \tag{2.148}$$

The parameter a_r in Equation (2.115) can easily be reduced, using (2.116)-(2.118) and (2.125), to

$$a_r^{\ 2} = \frac{4\bar{n}_1(0)\Delta g}{S^2}\left\{\frac{\Delta\bar{n}_{eff}}{\Delta g} + \left[\left(\frac{\Delta\bar{n}_{eff}}{\Delta g}\right)^2 + \left(\frac{\Gamma}{k_o}\right)^2\right]^{1/2}\right\} \tag{3.2}$$

or

$$a_r^{\ 2} = \frac{4\bar{n}_1(0)\Delta g}{S^2}\left\{R_g + \left[R_g^{\ 2} + \left(\frac{\Gamma}{k_o}\right)^2\right]^{1/2}\right\} \tag{3.3}$$

For the pure gain-guiding situation, or $R_g = 0$,

$$a_r^{\ 2} = \frac{4\Gamma\bar{n}_1(0)\Delta g}{k_o\ S^2} \tag{3.4}$$

Therefore, the ratio of the half-power width W_h for CW or pulsed operation to that of the pure gain guiding condition is

$$\frac{W_h(R_g \neq 0)}{W_h(R_g = 0)} = \left\{\frac{\Gamma/k_o}{R_g + [R_g^{\ 2} + (\Gamma/k_o)^2]^{1/2}}\right\}^{1/4} \tag{3.5}$$

Figure 3.3 shows the guiding parameters of CW operation for different laser dimensions. For pulsed operation at threshold, R_g is found to be -1.57×10^{-6}, -2.88×10^{-6} and -3.77×10^{-6} when the active layer thickness d is 0.12, 0.2 and 0.3 μm, respectively. As indicated in (3.1), index-guiding becomes significant as R_g becomes larger.

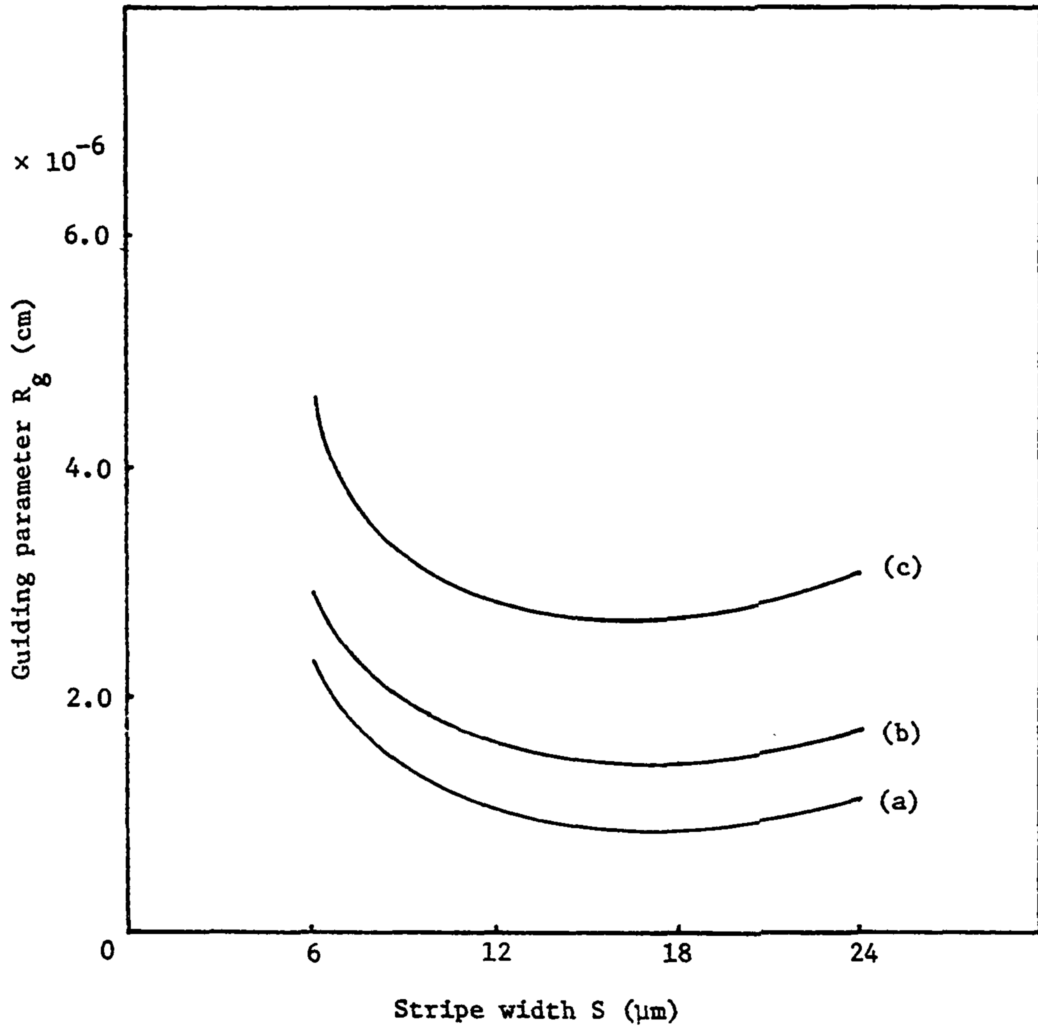

Fig. 3.3. Waveguiding parameter R_g as a parameter of the stripe width S.
(a) d = 0.12 μm (b) d = 0.2 μm (c) d = 0.3 μm

According to Figure 3.3, the index-guiding is relatively important in a narrow-stripe laser or a thick-active-layer laser.

The temperature difference between the center and edge region of the stripe is found to be almost the same at threshold for different stripe widths as long as the active layer thickness remains the same. Hence, the thermal gradient in the active region is greater in a narrow stripe laser.

In a thick-active-layer laser, a higher injection current is needed to achieve the threshold condition. Consequently, temperature rise in the active region is more significant, thus making index-guiding relatively important.

In Figures 3.4 through 3.6, W_h and θ_h at threshold are calculated and compared with the experimental data reported in Paoli [61] and Kirkby et al. [74]. The result, shown as a function of stripe width S, is in good agreement with the experiments for CW operation condition. The calculation shows that the CW W_h can be reduced 1.5 ~ 3.0 μm from the pulsed operation case. Also, θ_h in CW operation is 1.5 ~ 2.5 degrees smaller than it is in pulsed operation. This narrowing of mode size is desirable for efficient coupling into the optical fiber. However, it should be pointed out that this advantage in optical coupling is minimal because most of the optical fibers have numerical apertures greater than 0.16 which corresponds to a full angle of 18.5° within which a fiber accepts light.

In addition, narrowing occurs not only in the fundamental mode, which is of concern here, but also in the higher order mode in the lateral direction. For instance, the mode width of the first order

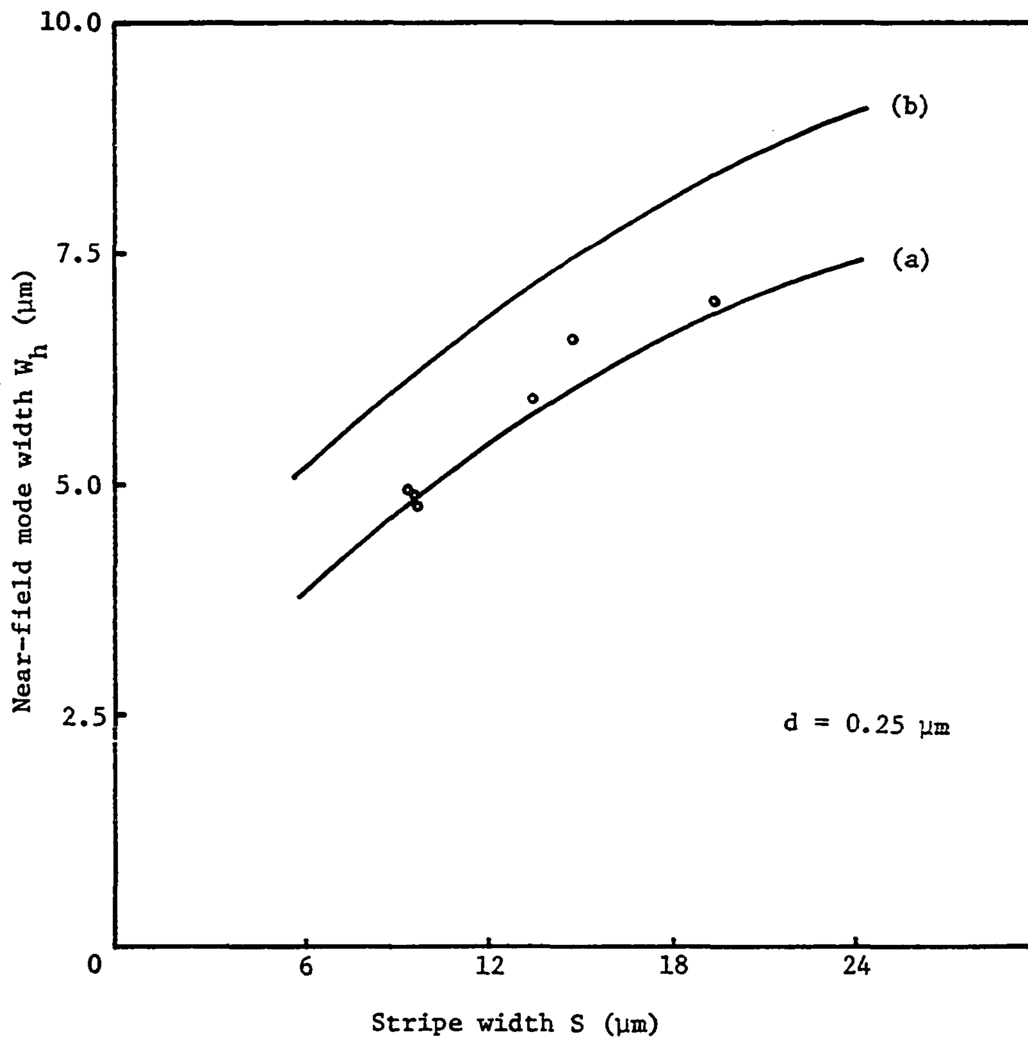

Fig. 3.4. Near-field mode width at threshold as a function of the stripe width. (a) CW operation (b) pulsed operation. Circles represent CW experimental data from [74]

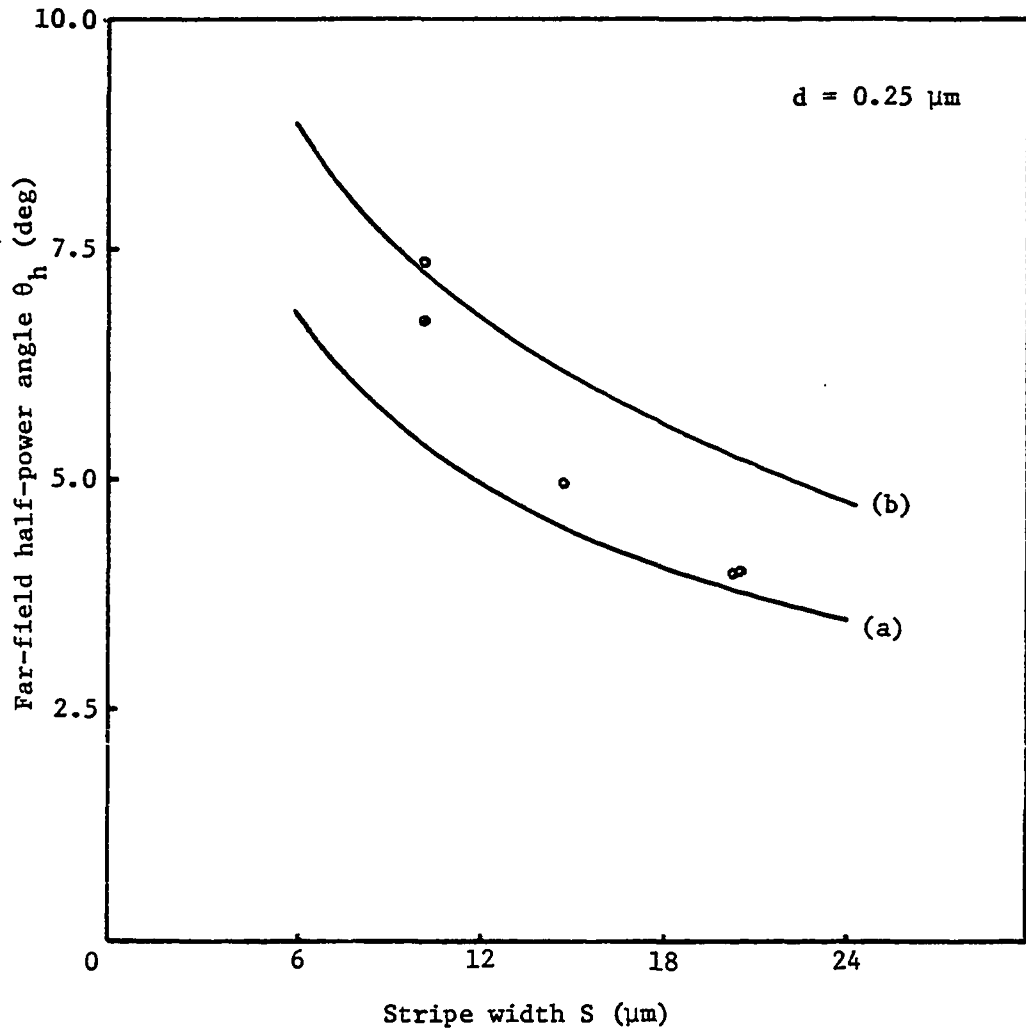

Fig. 3.5. Far-field half-power angle at threshold as a function of the stripe width. (a) CW operation (b) pulsed operation. Circles represent CW experimental data from [74]

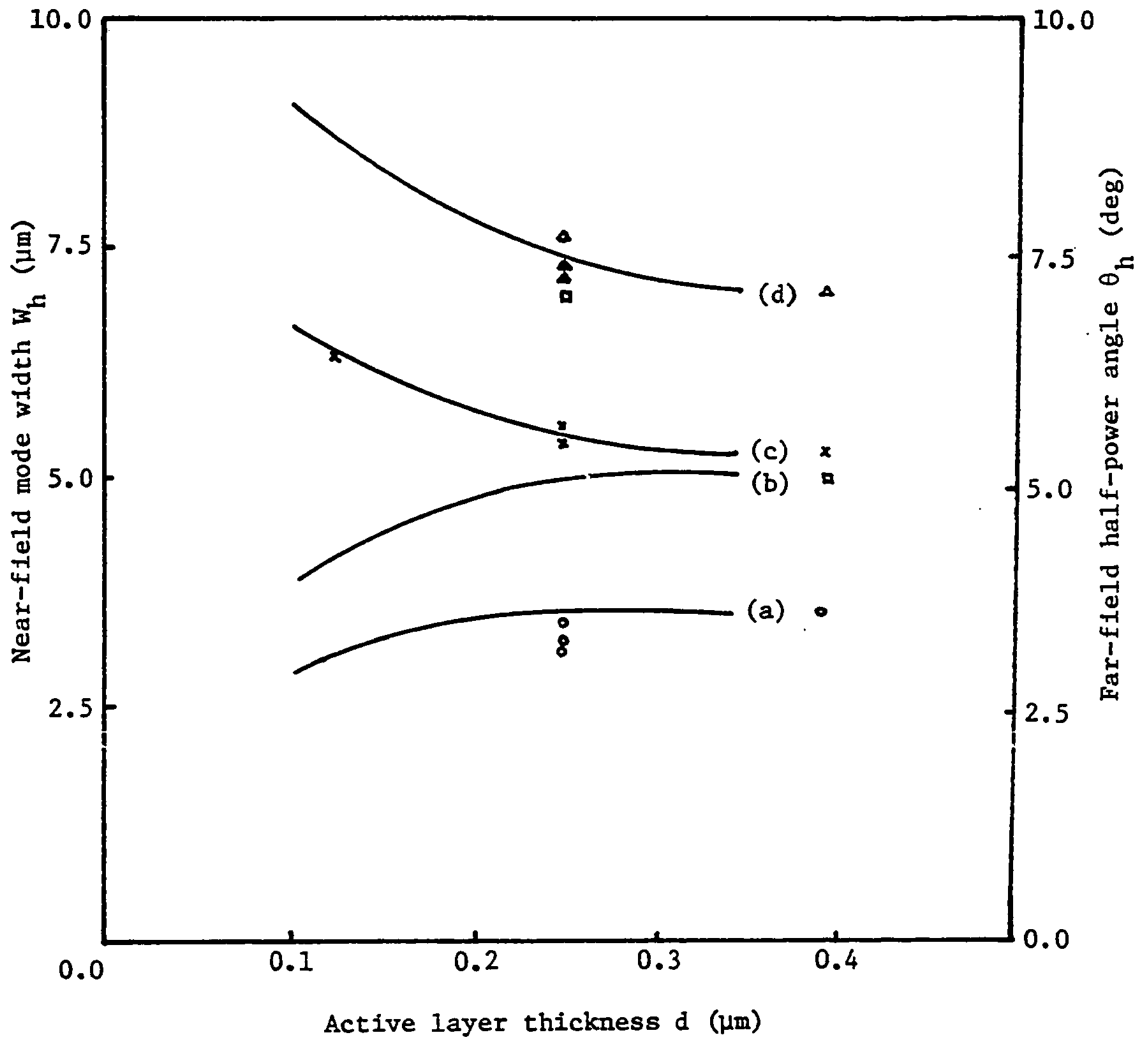

Fig. 3.6. CW near- and far-field mode width at threshold as functions of the active layer thickness. (a) θ_h for S = 24 μm (b) θ_h for S = 12 μm (c) W_h for S = 12 μm (d) W_h for S = 24 μm Symbols represent experimental data from [74]

lateral mode reduces so that the peaks of the optical intensity distribution move inward to the center region of the stripe. It is found that the distance between the two peaks of the first order mode, W_p, is

$$W_p = 2/(k_o\ a_r)^{1/2} \tag{3.6}$$

Therefore, the degree of reduction in W_p caused by the index-focusing effect is identical to that of W_h. Figure 3.7 illustrates the reduction in W_p for CW operation.

The higher gain constant around the center region of the stripe results in an enhancement of mode gain for the higher order mode such that the multimode operation occurs at a lower power output level. To illustrate the effect, ΔG^{ℓ} is defined as the difference between the lateral fundamental and first order mode gains. That is,

$$\Delta G^{\ell} \equiv G_0^{\ell} - G_1^{\ell} \tag{3.7}$$

Using (2.140) and (2.142),

$$\Delta G^{\ell} = \frac{4\Delta g}{k_o\ a_r\ S^2} \tag{3.8}$$

Equation (3.8) indicates that the first order lasing mode can easily be excited in a wide-stripe laser where S is large and Δg is small. Also, increased a_r for CW operation in comparison to that for pulsed operation indicates that CW operation is favorable to the onset of

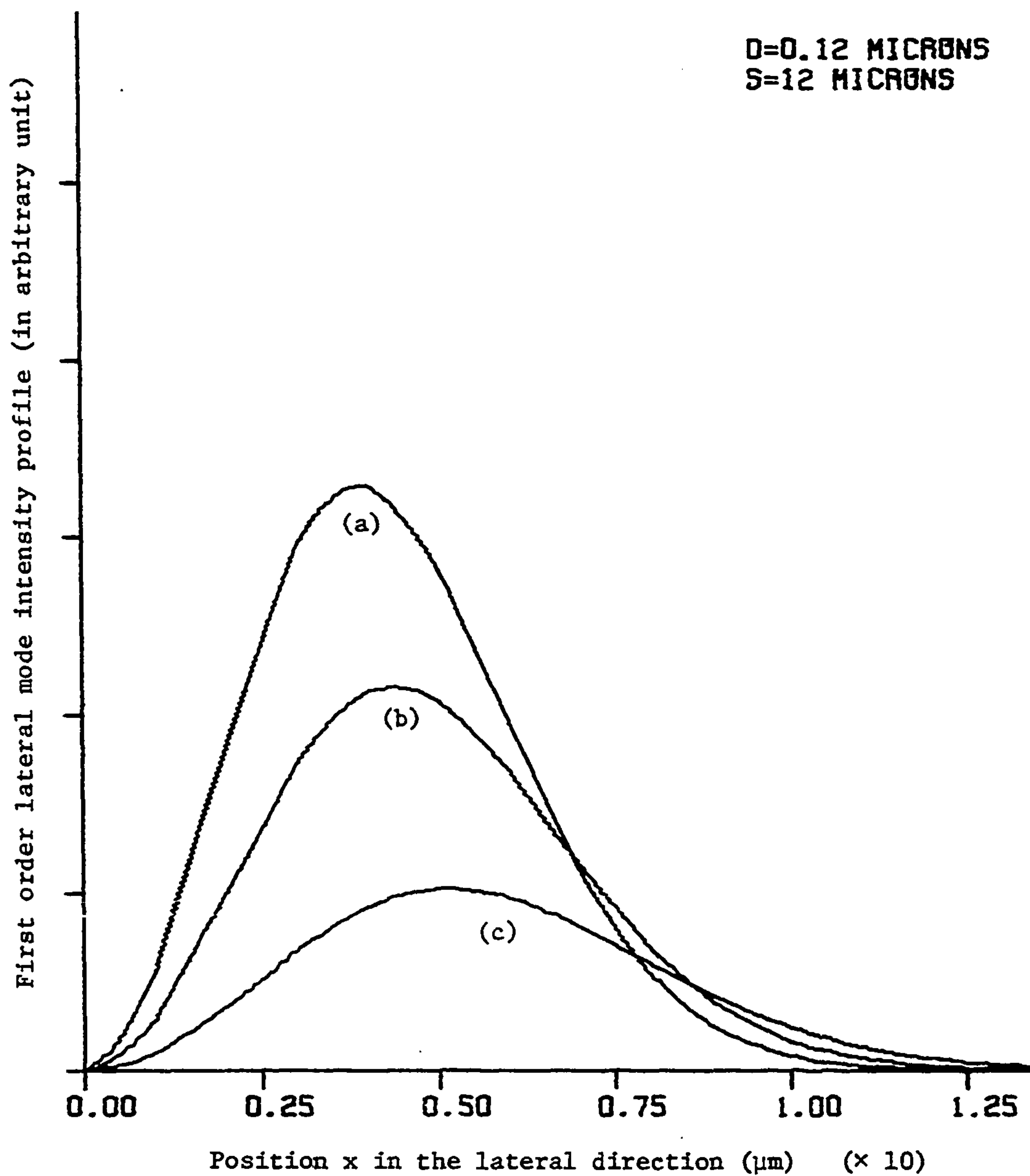

Fig. 3.7. First order mode intensity profiles for different operating conditions. (a) CW operation (b) gain-guiding only (c) pulsed operation

higher order modes. Figure 3.8 illustrates the mode gain difference between the fundamental and first order mode as a function of stripe width S. In many applications small ΔG^{ℓ} is highly undesirable since this results in a kink in light output-current characteristics at a lower optical power level. This nonlinearity is often related to the onset of the higher order mode. The trend shown in Figure 3.8 is consistent with that described in other publications [57,75].

2. Effect on threshold current

The temperature rise in the active region is believed to increase CW threshold current. On the other hand, the thermal guiding mechanism discussed in the previous section slightly reduces threshold current in the range of ~5 mA for a typical laser diode.

Assuming that this reduction is not significant when compared to the increase, the CW threshold current I_{th}^{CW} from Equation (1.1) can be written

$$I_{th}^{CW}(T_h) = I_{th}^{P}(T_h) \exp\left[\frac{\Delta T_j^{th}(T_h)}{T_o}\right] \tag{3.9}$$

and the average junction temperature rise ΔT_j^{th} is determined by (1.3),

$$\Delta T_j^{th}(T_h) = R_2 V_j I_{th}^{CW}(T_h) \tag{3.10}$$

The average thermal resistance R_2 in the active region was defined by (2.67). In (3.10), the joule heating was assumed to be insignificant in (2.69).

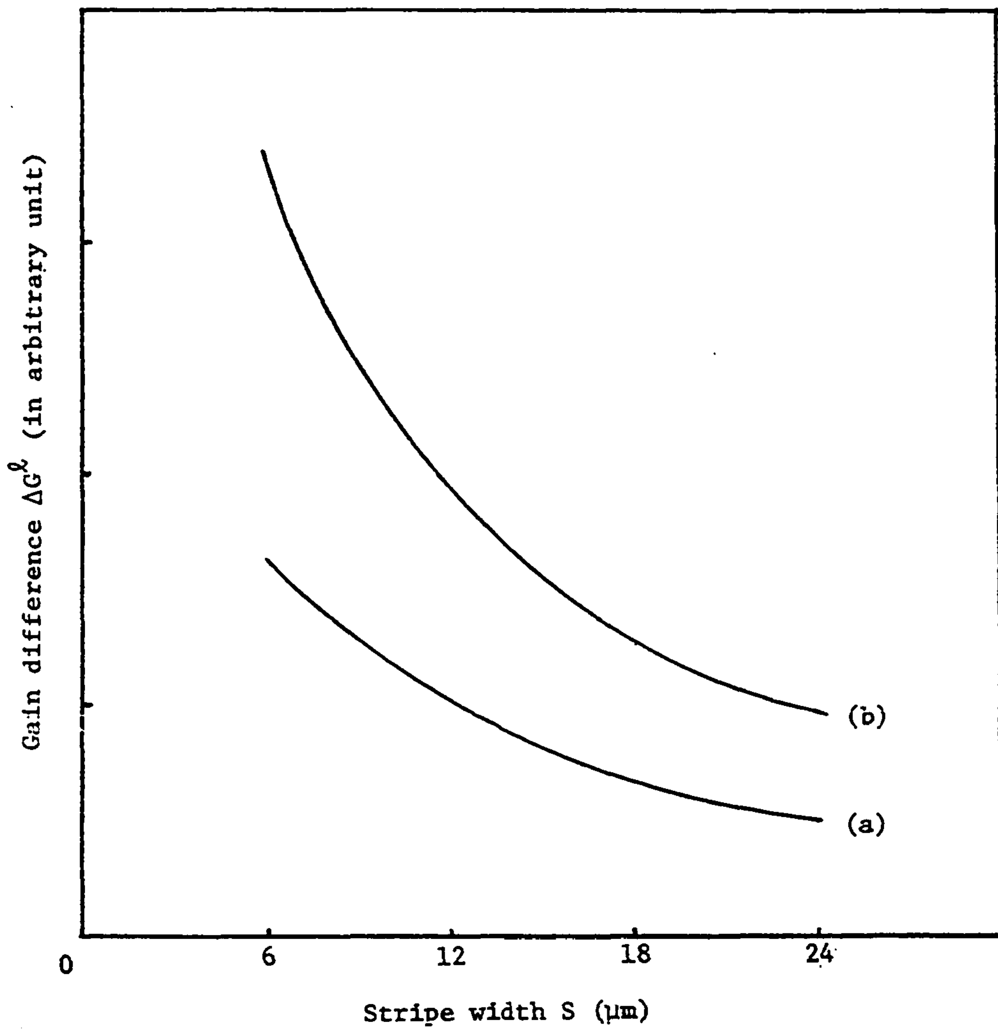

Fig. 3.8. Difference of mode gain ΔG^{ℓ} as a function of the stripe width.
(a) CW operation (b) pulsed operation

Substituting (3.10) into (3.9) yields

$$I_{th}^{CW}(T_h) = I_{th}^{P}(T_h) \exp\left[\frac{R_2 V_j I_{th}^{CW}(T_h)}{T_o}\right] \tag{3.11}$$

where, as stated earlier,

$$I_{th}^{P}(T_h) = I_{th}^{P}(300°K) \exp\left(\frac{T_h - 300°K}{T_o}\right) \tag{1.1}$$

Since the model used in this study calculates the thermal resistance R_2 and pulsed threshold current $I_{th}^{P}(300°K)$, it is possible to determine CW threshold current. Here $V_j = 1.6$ V and $T_o = 125°K$ are used. A typical threshold current with higher heat sink temperature is shown in Figure 3.9.

At a higher ambient temperature, the laser ceases to operate in the CW mode. The maximum temperature for CW operation, T_{max}^{CW}, can be estimated from the condition that Equation (3.11) has a solution for I_{th}^{CW}.

Let F be

$$F(I_{th}^{CW}) = I_{th}^{P}(T_h) \exp\left[\frac{R_2 V_j I_{th}^{CW}(T_h)}{T_o}\right] - I_{th}^{CW}(T_h) \tag{3.12}$$

For convenience, let (3.12) be

$$F = u \exp(vI_{th}^{CW}) - I_{th}^{CW} \tag{3.13}$$

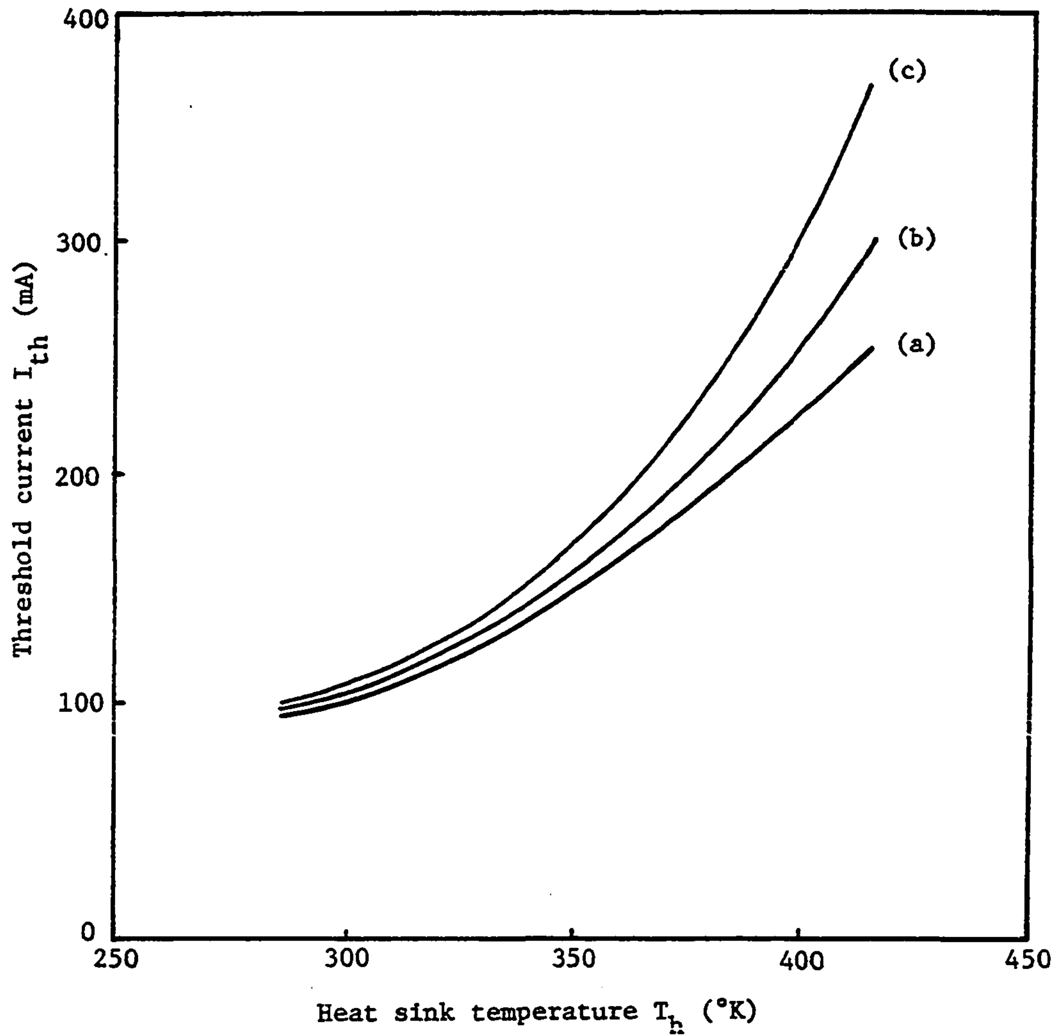

Fig. 3.9. Threshold current increase as a function of heat sink temperature. (a) pulsed operation (b) CW operation with R_2 = 50 °K/W (c) CW operation with R_2 = 100 °K/W

where

$$u = I_{th}^{P}, \tag{3.14}$$

$$v = \frac{R_2 V_j}{T_o} \tag{3.15}$$

The condition that F = 0 has a real positive solution for I_{th}^{CW} is obtained as follows. First,

$$\frac{dF}{dI_{th}^{CW}} = uv \exp(vI_{th}^{CW}) - 1 \tag{3.16}$$

The minimum of F occurs at $dF/dI_{th}^{CW} = 0$, i.e.,

$$I_{th}^{CW} = \frac{1}{v} \ln \frac{1}{uv} \tag{3.17}$$

Next F_{min}, the minimum of F, should be less than zero. That is,

$$F_{min} = \frac{1}{v} - \frac{1}{v} \ln \frac{1}{uv} \leq 0 \tag{3.18}$$

or

$$u \leq \frac{1}{ev} \tag{3.19}$$

Substituting (3.14) and (3.15) back into (3.19) yields

$$I_{th}^{P}(T_h) \leq \frac{T_o}{eR_2 V_j} \tag{3.20}$$

or

$$I_{th}^{P}(300°K)\ \exp\left(\frac{T_h - 300°K}{T_o}\right) \leq \frac{T_o}{eR_2\ V_j} \tag{3.21}$$

Therefore, the maximum temperature for possible CW operation is

$$T_{max}^{CW} = 300°K + T_o\ \ell n\left[\frac{T_o}{eR_2V_j\ I_{th}^{P}(300°K)}\right] \tag{3.22}$$

where e = 2.718.

Since the solution (3.22) is a purely mathematical limit, the actual T_{max}^{CW} should be substantially lower. For instance, a significant amount of temperature rise will result in thermal stress in the lattice structure, which in turn may cause rapid degradation.

Nevertheless, Equation (3.22) deserves some attention. To increase the T_{max}^{CW}, it is necessary to reduce thermal resistance R_2 and threshold current at room temperature $I_{th}^{P}(300°K)$. It should also be pointed out that R_2 and $I_{th}^{P}(300°K)$ ought to be reduced simultaneously to efficiently increase the high temperature operation range. The dependence of T_{max}^{CW} on R_2 and $I_{th}^{P}(300°K)$ is illustrated in Figure 3.10. Since the temperature rise ΔT_j^{th} at room temperature is

$$\begin{aligned} \Delta T_j^{th}(300°K) &= R_2\ V_j\ I_{th}^{CW}(300°K) \\ &\simeq R_2\ V_j\ I_{th}^{P}(300°K) \end{aligned} \tag{3.23}$$

Equation (3.22) can be written as

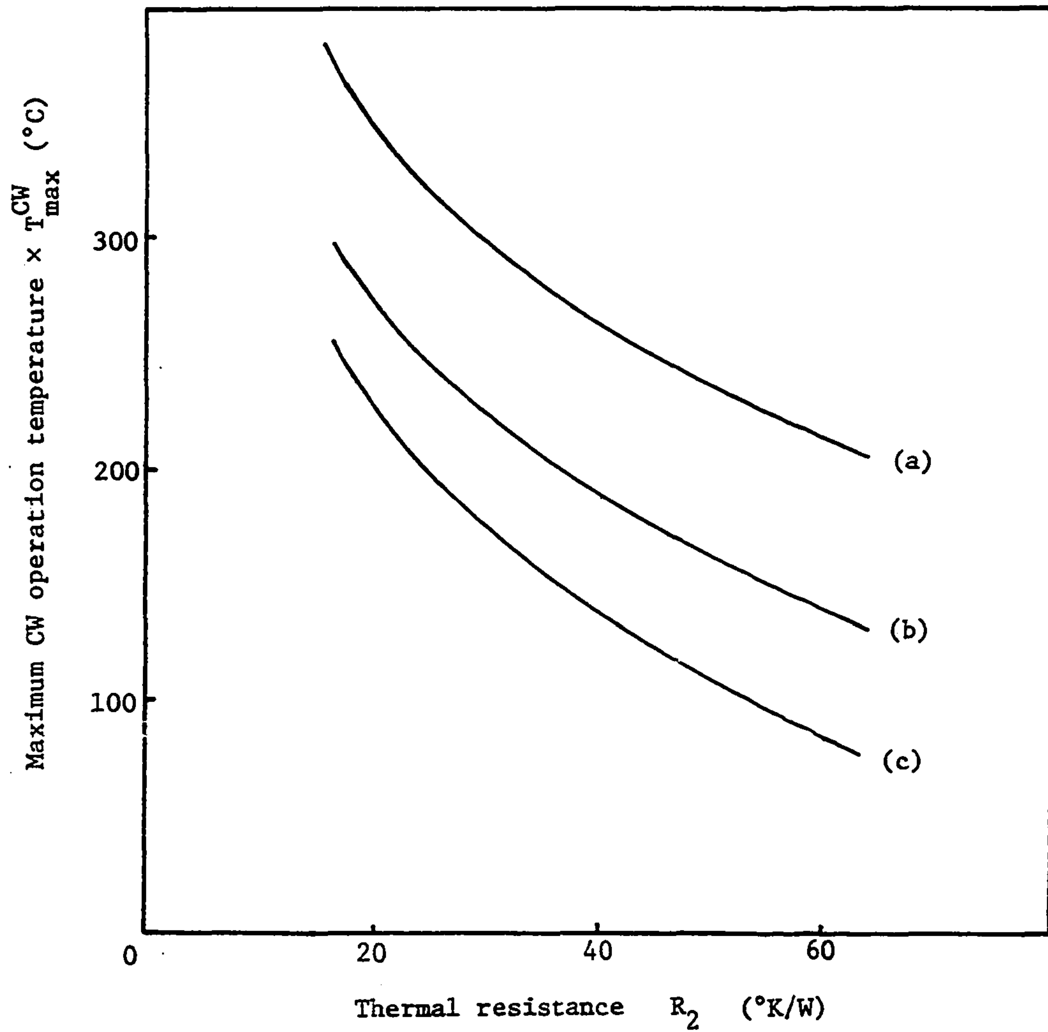

Fig. 3.10. Maximum CW operation temperature as a function of thermal resistance of the laser. (a) I_{th} = 100 mA (b) I_{th} = 200 mA (c) I_{th} = 300 mA

$$T_{max}^{CW} \simeq 300°K + T_o \, \ell n \left[\frac{T_o}{e \, \Delta T_j^{th}(300°K)} \right] \quad (3.24)$$

Equation (3.24) indicates that by reducing ΔT_j^{th} to half, it is possible to increase the maximum CW operation temperature up to 0.69 T_o. Since $T_o \simeq 125°K$ for the well-designed GaAs/AlGaAs laser, the amount is approximately 87°K. The reduction of ΔT_j^{th} will be further discussed later in this section.

An alternate way of increasing T_{max}^{CW} is to increase the characteristic temperature T_o. The correlation between T_o and the device structure has not been investigated rigorously. It has been observed, however, that T_o is higher for a laser diode with high energy barriers at the heterojunctions which offer better confinement of injected carriers. In InGaAsP/InP lasers, T_o is usually 40 ~ 80°K, thus creating an extremely strong temperature dependence for laser performance. The study on how to increase T_o is outside the scope of the present work.

3. Effect on spectrum shift

The output spectrum shift of the laser is mainly the result of a change in the refractive index and energy bandgap of the active region. Since the refractive index is temperature dependent, as reflected in (2.89) and (2.90), the resonant wavelength of each Fabry-Perot mode is affected by the temperature of the active region. Consider the possible lasing wavelength in a Fabry-Perot resonator [51]:

$$\lambda = \frac{2\bar{n}L}{m} \quad (3.25)$$

where m is an integer. The temperature dependence of the wavelength is [17]

$$\frac{d\lambda}{dT} = \frac{2L}{m}\left(\frac{d\bar{n}}{dT}\right)_{\lambda} + \frac{2L}{m}\left(\frac{d\bar{n}}{d\lambda}\right)_{T}\frac{d\lambda}{dT} + \frac{2\bar{n}}{m}\frac{dL}{dT} \tag{3.26}$$

For GaAs, $(1/L)(dL/dT) \ll (1/\bar{n})(d\bar{n}/dT)_{\lambda}$ is valid. Therefore, Equation (3.26) can be rearranged as

$$\frac{d\lambda}{dT} = \frac{\frac{\lambda}{\bar{n}}\left(\frac{d\bar{n}}{dT}\right)_{\lambda}}{1 - \frac{\lambda}{\bar{n}}\left(\frac{d\bar{n}}{d\lambda}\right)_{T}} \tag{3.27}$$

where the refractive index $\bar{n}$ depends on the temperature T as in (2.89) and (2.90). Paoli [15] and Meixner and Unger [18] reported $d\lambda/dT$ for DH lasers as 2.8 Å/°C and 4.3 Å/°C, respectively. The shift of spectrum was observed both under and above the threshold.

The CW spectrum of the laser, therefore, deviates from the pulsed operation as

$$\Delta\lambda = \lambda_{CW} - \lambda_{p} = \frac{d\lambda}{dT}\Delta T_{j} \tag{3.28}$$

where λ_{CW} and λ_{p} represent the wavelength at CW and pulsed operation, respectively. Figures 3.11 and 3.12 illustrate the spectrum shifts resulting from junction heating. The clamping of the junction temperature rise, as shown in Figure 3.11, was experimentally observed by Turley et al. [17]. Also, the linear increase of the temperature rise

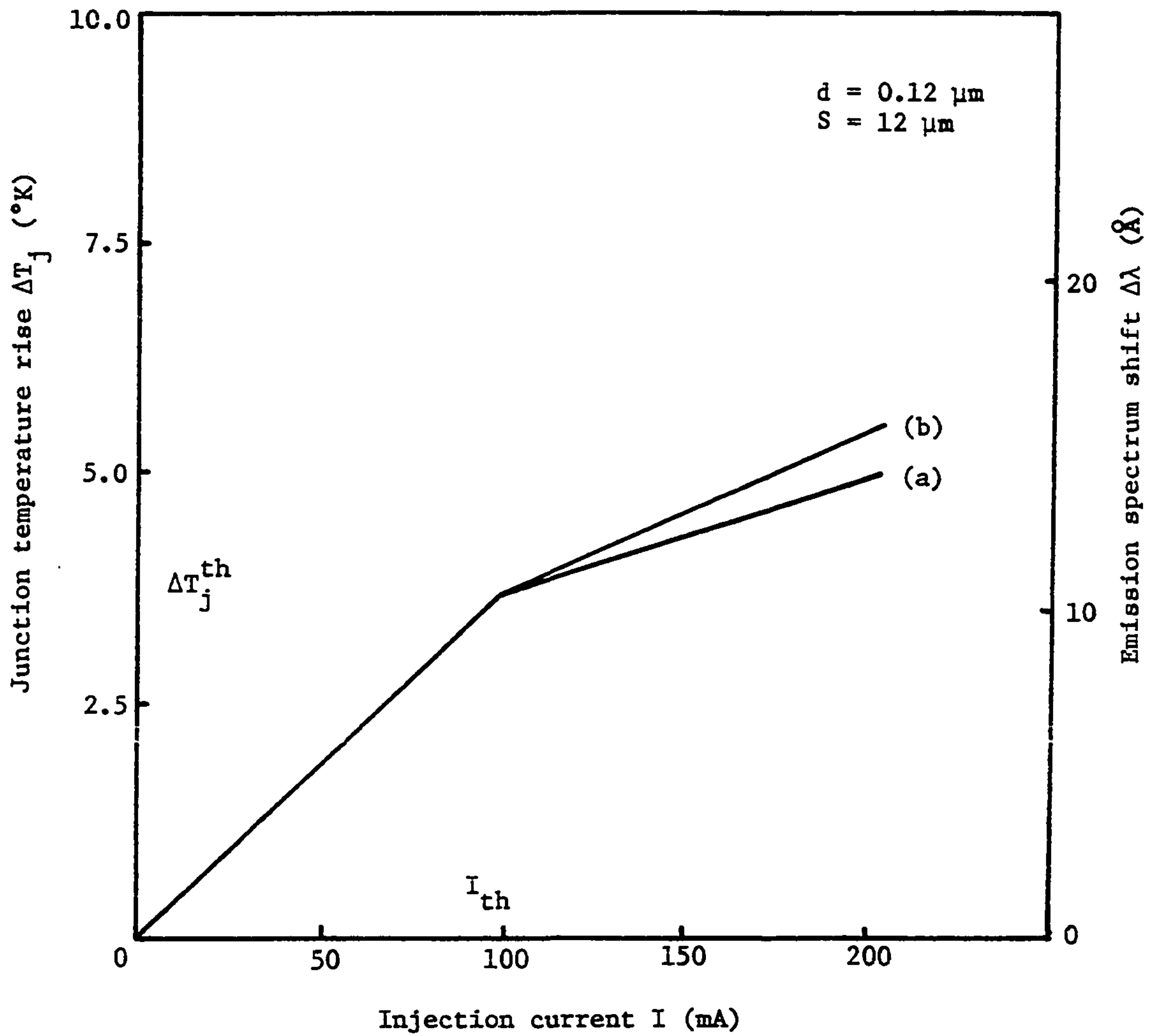

Fig. 3.11. Junction temperature rise and corresponding emission wavelength increase for different injection current level. (a) $\eta_d = 60\%$ (b) $\eta_d = 50\%$

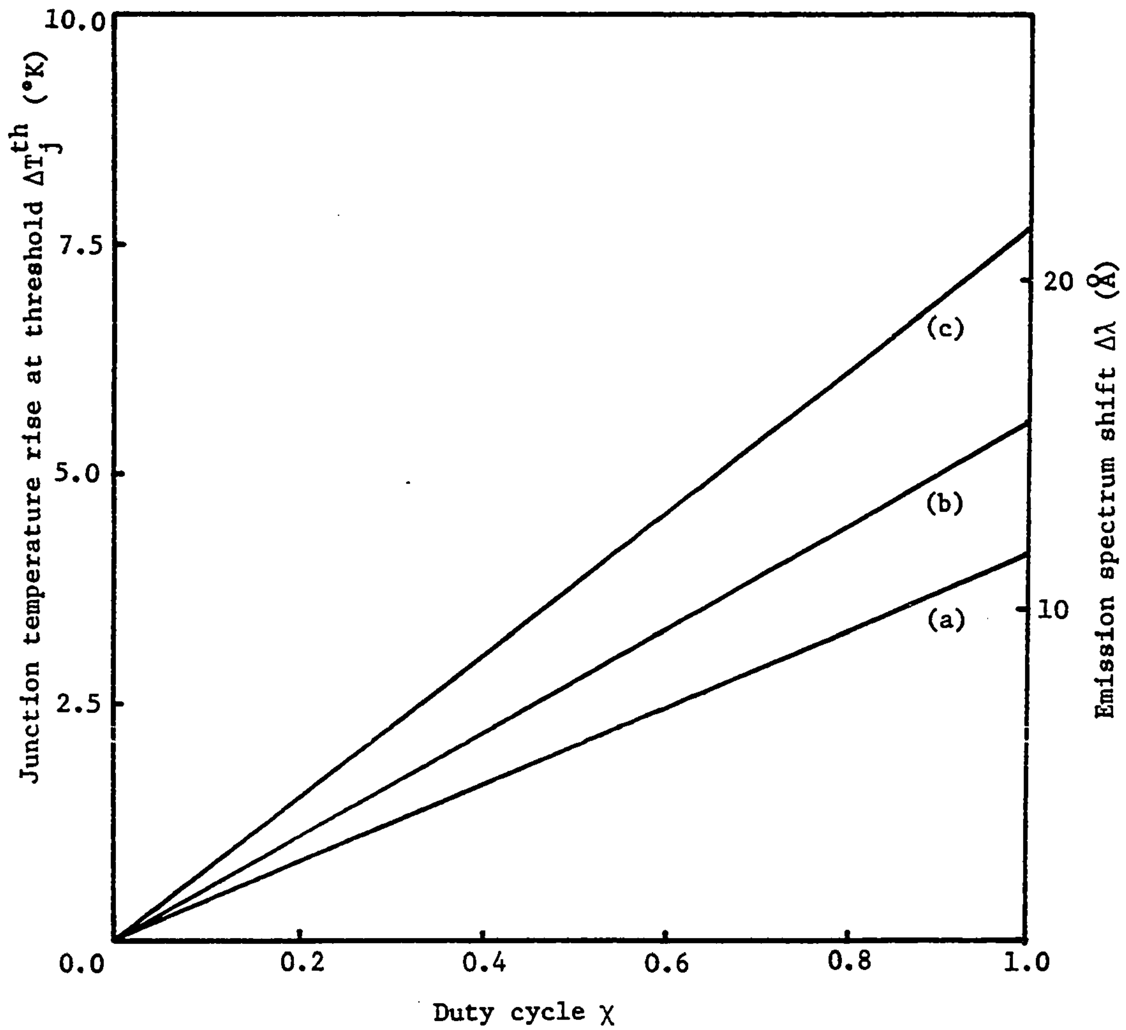

Fig. 3.12. Junction temperature rise and corresponding emission wavelength shift at threshold condition for various duty cycle. (a) d = 0.12 μm (b) d = 0.2 μm (c) d = 0.3 μm

in Figure 3.12 is consistent with the experimental observation by Paoli [15].

In many applications, such as a wavelength multiplexing, spectrum shift is highly undesirable. To reduce the amount of potential spectrum shift, it is again necessary to reduce junction heating in the laser. Design aspects to reduce junction heating are discussed later in this section.

4. Limitation of the model

Because of the steps of approximation employed, there are several shortcomings in the model under discussion.

First, the model is not accurate for a narrow-stripe laser, especially under 10 μm width, because the assumption that the lateral mode intensity is well confined inside the stripe region is not true for a narrow stripe width. For this kind of laser, the mode intensity leaks into the region where the gain distribution cannot be approximated as a parabolic function. A non-Gaussian fundamental mode was experimentally observed by Asbeck et al. [76]. Functions in the form of $\cosh^{-a}(bx)$ were found to be more appropriate for approximating the dielectric constant variation in the active layer. Here the constant a is in the range of 0.1 to 10.

Next, the model does not offer an accurate solution for well-above-threshold behavior of the laser. Because of "hole burning" caused by stimulated emission, the gain profile in the active region is perturbed in cases of higher optical power emission. For instance, the continuity equation in the active region (2.11) becomes [59]

$$D_a \frac{\partial^2 n}{\partial x^2} - \frac{\partial n}{\partial t} + \frac{J_y(x)}{qd} - \frac{n}{\tau_n} - g(x)\ P(x) = 0 \tag{3.29}$$

where g(x) is the gain coefficient and P(x) is the optical flux density. Because of the approximations introduced, the present model was found to be inadequate to accommodate a self-consistent solution of Equation (3.29). A numerical method is desirable for solving the equation accurately.

A qualitative study, based on an approach taken by Kirkby et al. [74] in which that g(x) P(x) was approximated by a box-shaped function at the center region of the stripe, showed a further clamping of the junction temperature rise at and above the threshold level, as was briefly discussed in connection with Figure 3.11.

B. Reduction of Junction Temperature Rise

As shown in the previous section, temperature rise as a result of junction heating significantly affects the device characteristics. In this section, the effects of the various dimensions of the laser are investigated to establish a guideline for optimum thermal design.

1. Effect of each layer thickness

As previously discussed in Equation (3.22), it is important to reduce both the thermal resistance and the threshold current. Generally speaking, reducing the layer thickness between the active region and the heat sink allows more efficient heat dissipation. The junction temperature rise depends strongly on the active layer thickness, as illustrated in Figure 3.13. Reducing the active layer thickness to

the vicinity of 0.1 μm decreases junction heating by lowering the threshold current without substantially changing thermal resistance. Further reduction of the active layer thickness, however, increases threshold current and junction heating because of poor optical confinement.

A reduction in P-$Al_{0.3}Ga_{0.7}As$ layer thickness is very important, especially because of its low thermal conductivity. As shown in Figure 3.14, junction temperature rise and thermal resistance are reduced significantly for a thin P-$Al_{0.3}Ga_{0.7}As$ layer. The optimum thickness of this layer is believed to be ~1 μm since a further reduction results in the penetration of the guided mode into the p-GaAs capping layer, which has a higher absorption constant.

Figure 3.15 illustrates the dependence of temperature rise on the thickness of the p-GaAs capping layer. The capping layer is used for contacting because it is difficult to make a good ohmic contact to the AlGaAs layer. It is apparent that capping layer thickness should be minimized to improve the device's thermal property. At the present stage of development, the minimum thickness without downgrading the quality of the ohmic contact is about 1.0 ~ 1.5 μm.

The p-contact metal layers, Ti and Pt, are usually deposited by evaporation or the sputtering technique. These layers are 0.05 ~ 0.1 μm and 0.1 ~ 0.2 μm thick, respectively. If desirable, a thicker Au contact may be built up by electroplating. This layer also serves as a heat spreader for improved heat sinking. Figure 3.16 shows the effect of such an Au layer on two dimensional heat dissipation. As the Au

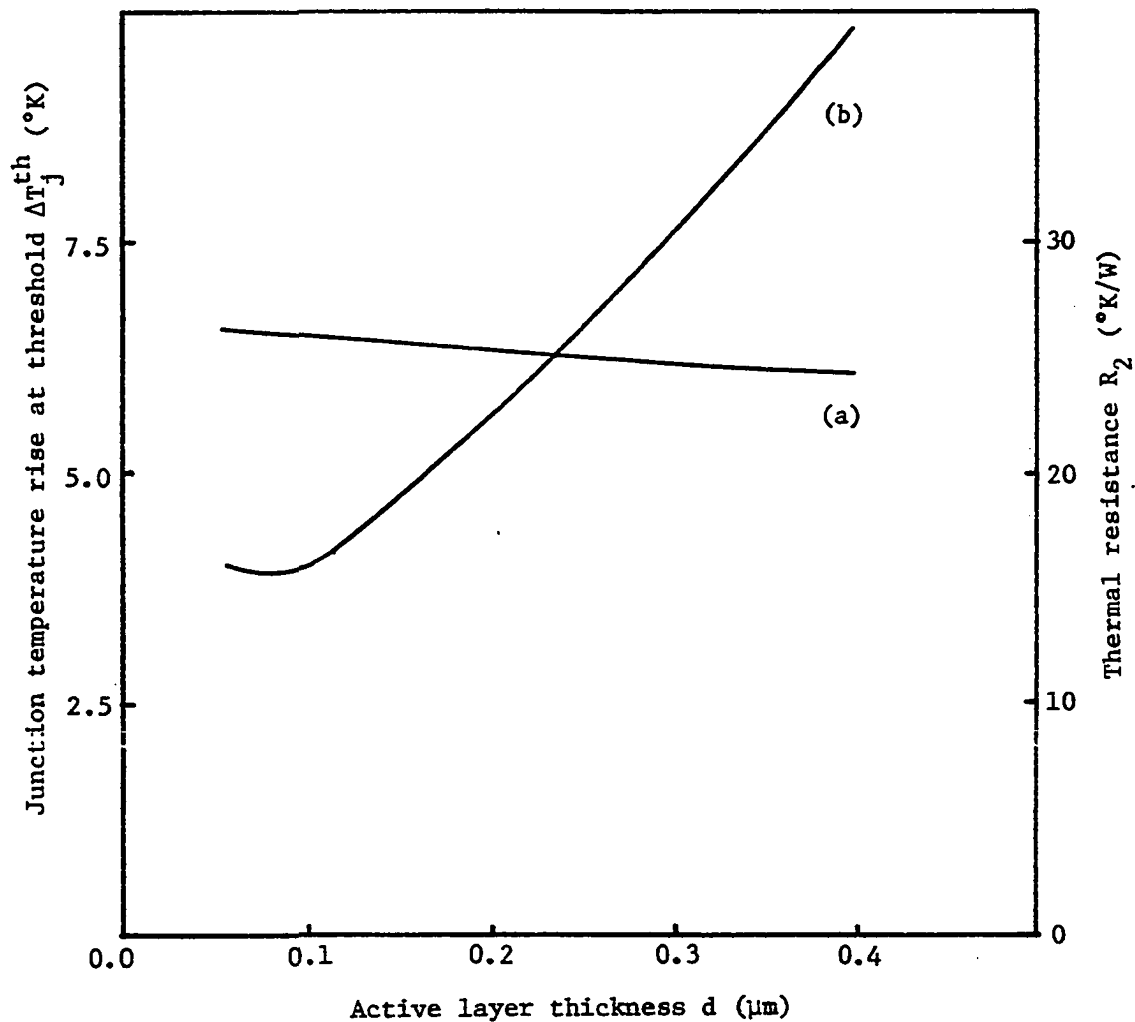

Fig. 3.13. Dependence of thermal resistance and junction temperature rise at threshold on the active layer thickness. (a) thermal resistance (b) junction temperature rise at threshold

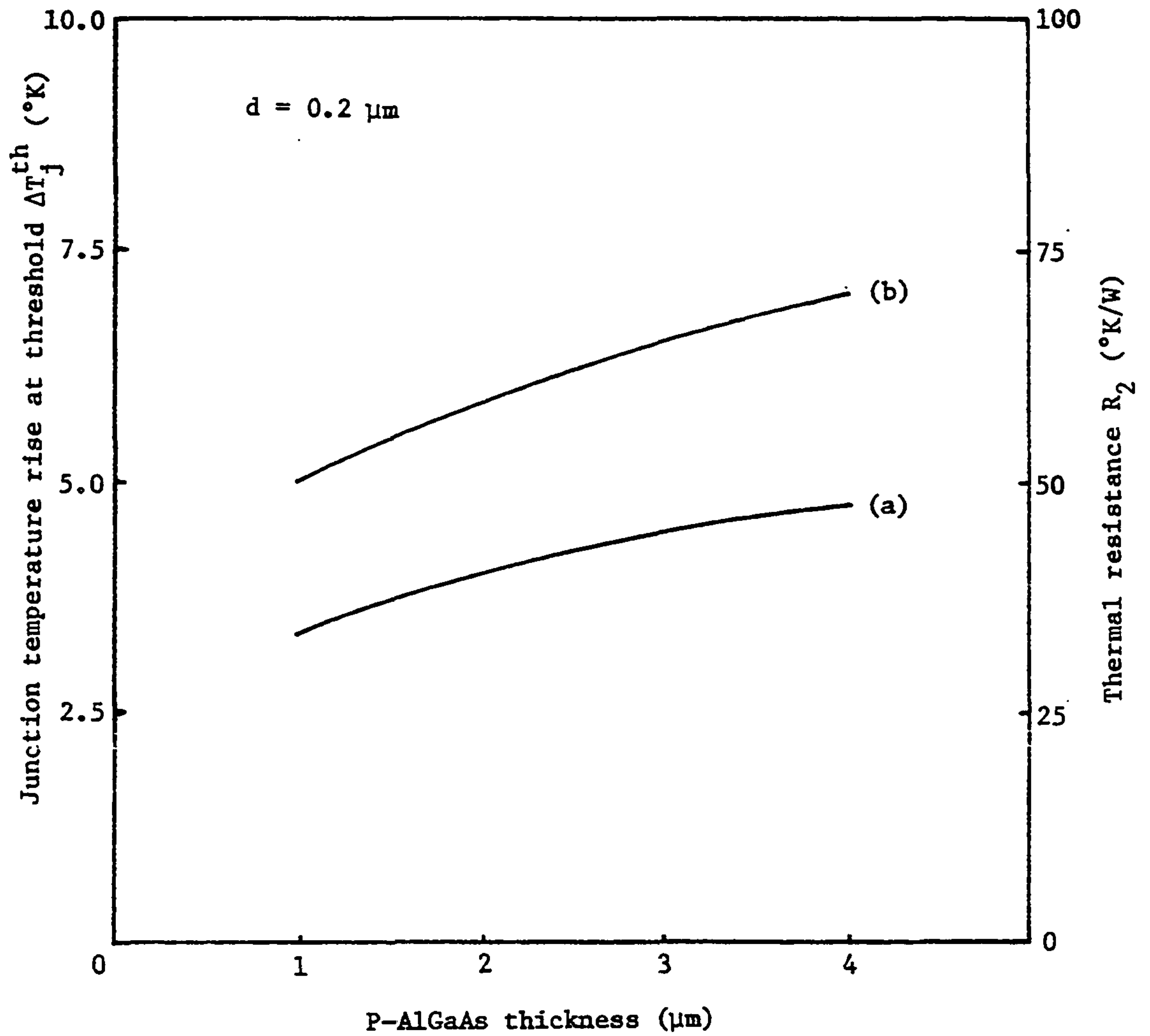

Fig. 3.14. Dependence of thermal resistance and junction temperature rise at threshold on the P-AlGaAs layer thickness.
(a) thermal resistance (b) junction temperature rise at threshold

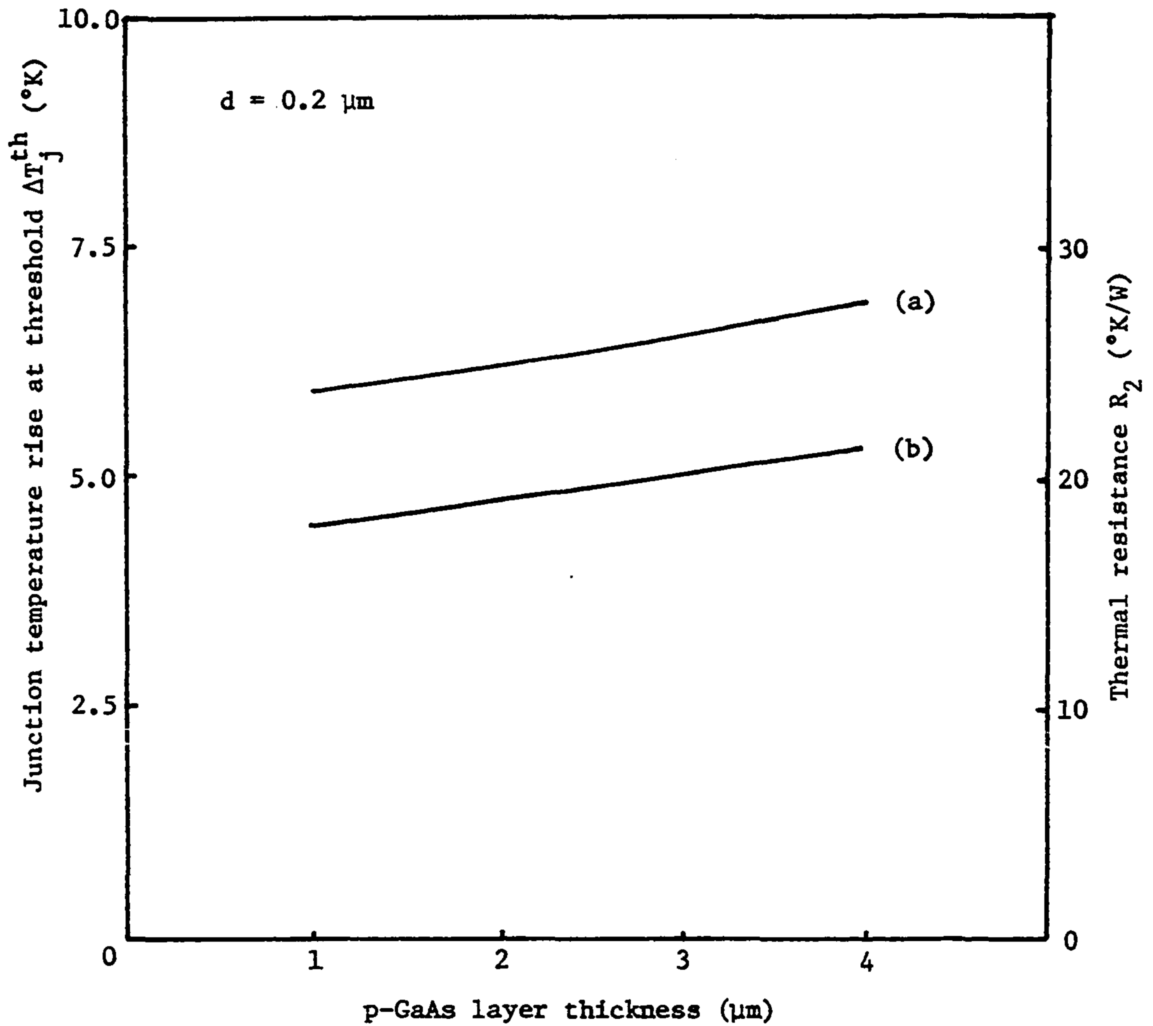

Fig. 3.15. Dependence of thermal resistance and junction temperature rise at threshold on the p-GaAs capping layer thickness. (a) thermal resistance (b) junction temperature rise at threshold

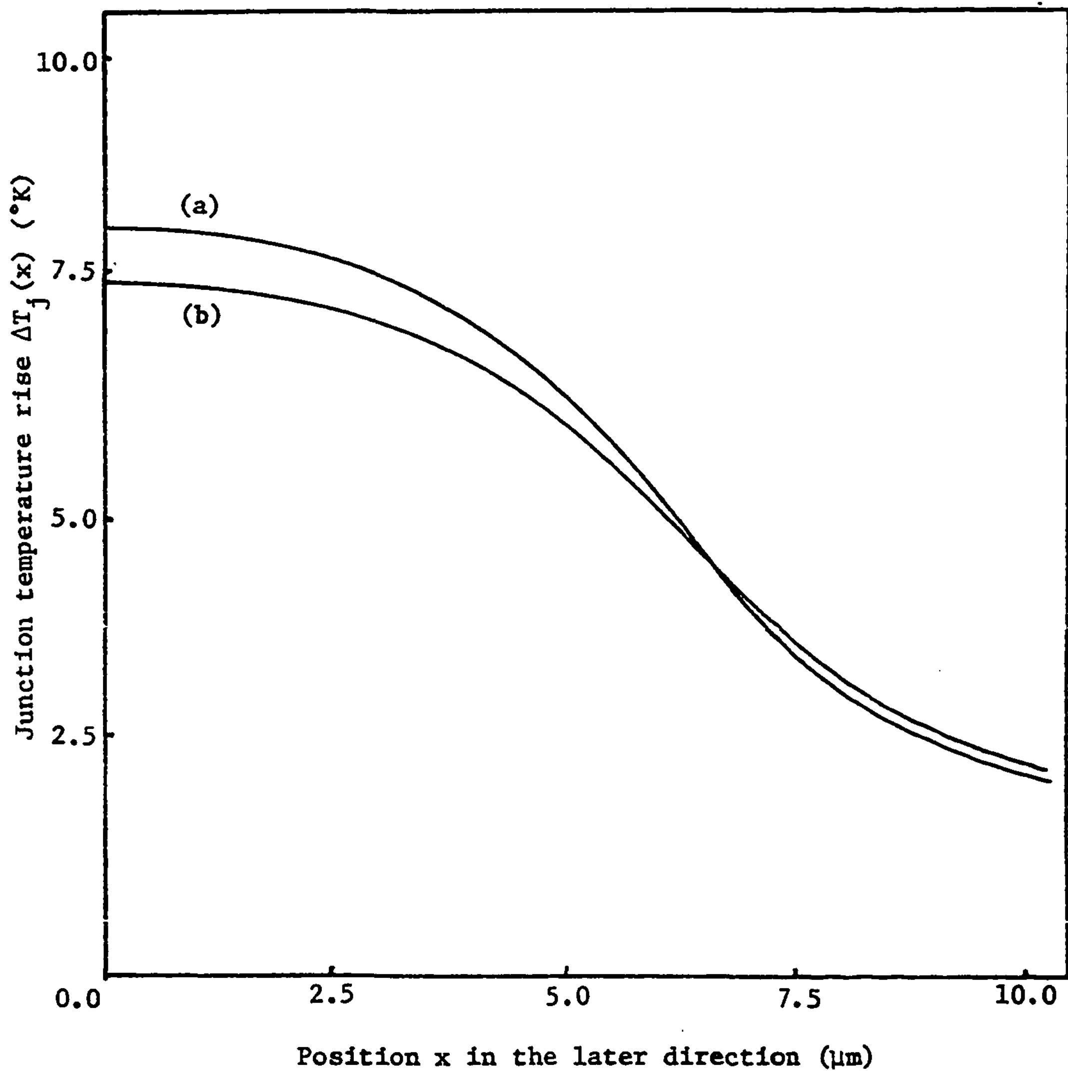

Fig. 3.16. Heat spreading effect by Au layer thickness. (a) Au layer = 10 μm thick (b) Au layer = 0.1 μm thick

thickness is increased from 0.1 μm to 10 μm, the junction temperature decreases about 0.7°K for a moderately thick laser at room temperature.

2. Effect of stripe width and laser cavity length

Increasing stripe width and laser cavity length drastically reduces the thermal resistance of the device. However, because of the proportional increase in threshold current, junction heating is not significantly reduced.

Figures 3.17 and 3.18 illustrate the dependence of thermal resistance and threshold current, respectively, on stripe width S. The resulting junction temperature rise, shown in Fig. 3.19, is found to be minimal at $S \cong 15$ μm. Unfortunately, this value falls into a range where there is severe nonlinearity in the light output vs. current characteristics.

Since the model used here assumes no variation in the z-direction, the threshold condition depends on cavity length only through Equation (2.144). Consequently, it requires a higher current density for small L to achieve a threshold which will result in a slightly higher junction temperature. The thermal resistance and junction temperature rise are illustrated in Figure 3.20.

Even though the thermal property is slightly improved by longer cavity length, the differential quantum efficiency decreases with increasing length. Biard et al. [77] derived the differential quantum efficiency η_d as

$$\eta_d = \eta_i[1 + \alpha L/\ln(\frac{1}{R})]^{-1} \qquad (3.30)$$

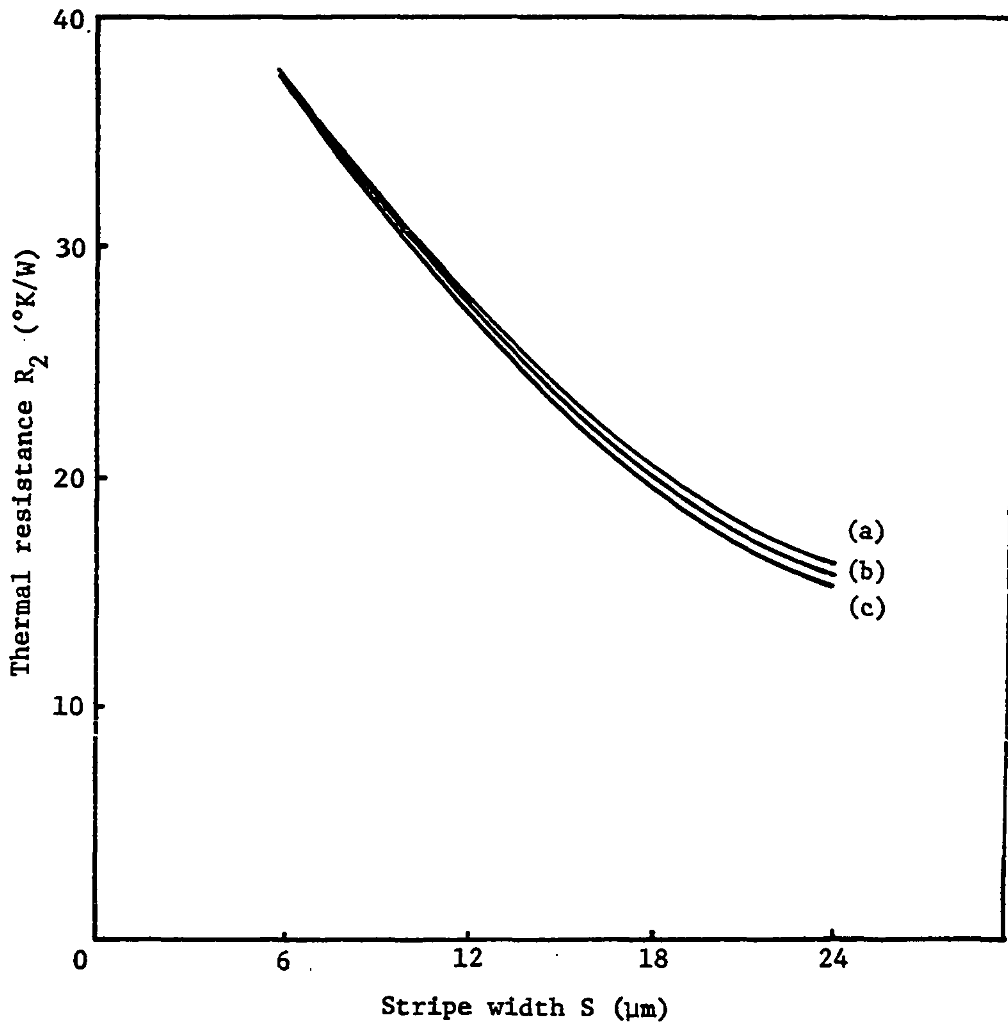

Fig. 3.17. Thermal resistance as a function of stripe width.
(a) d = 0.12 μm (b) d = 0.2 μm (c) d = 0.3 μm

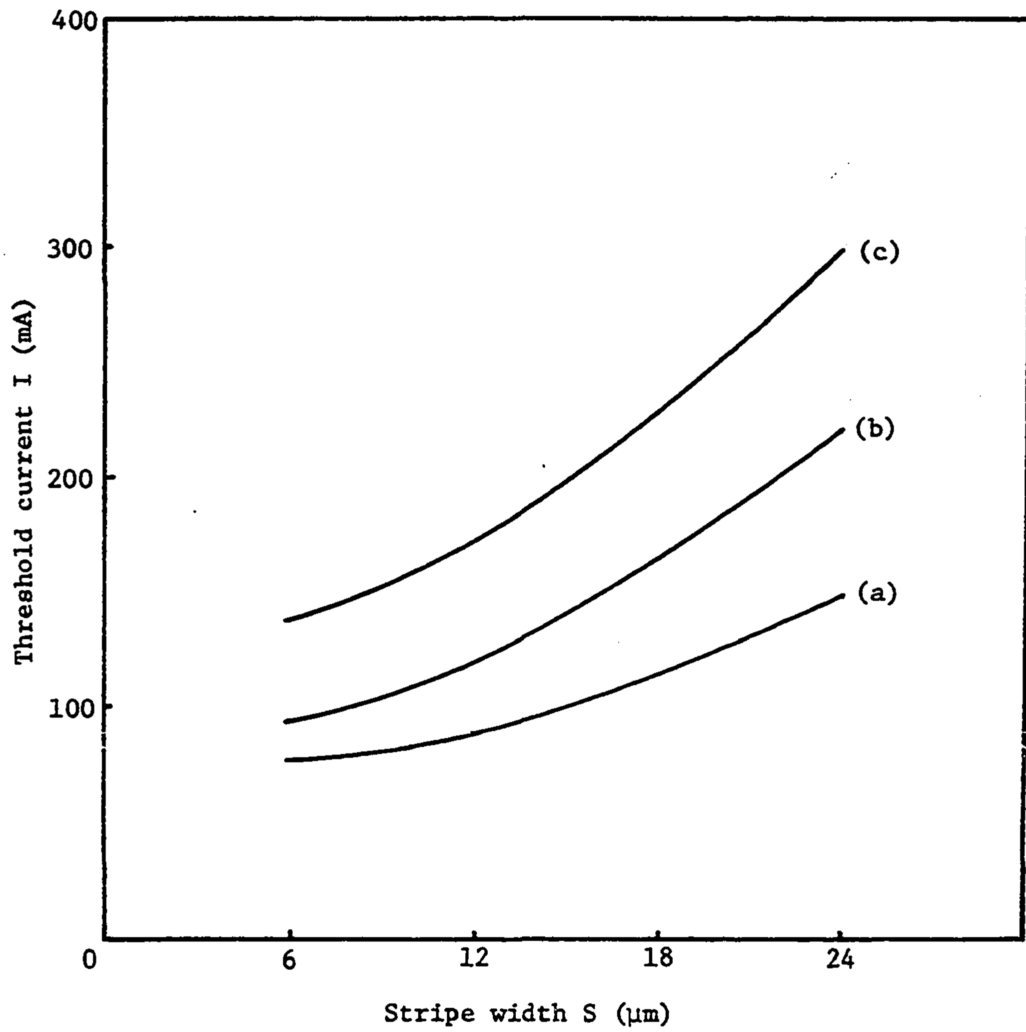

Fig. 3.18. CW threshold current as a function of stripe width.
(a) d = 0.12 μm (b) d = 0.2 μm (c) d = 0.3 μm

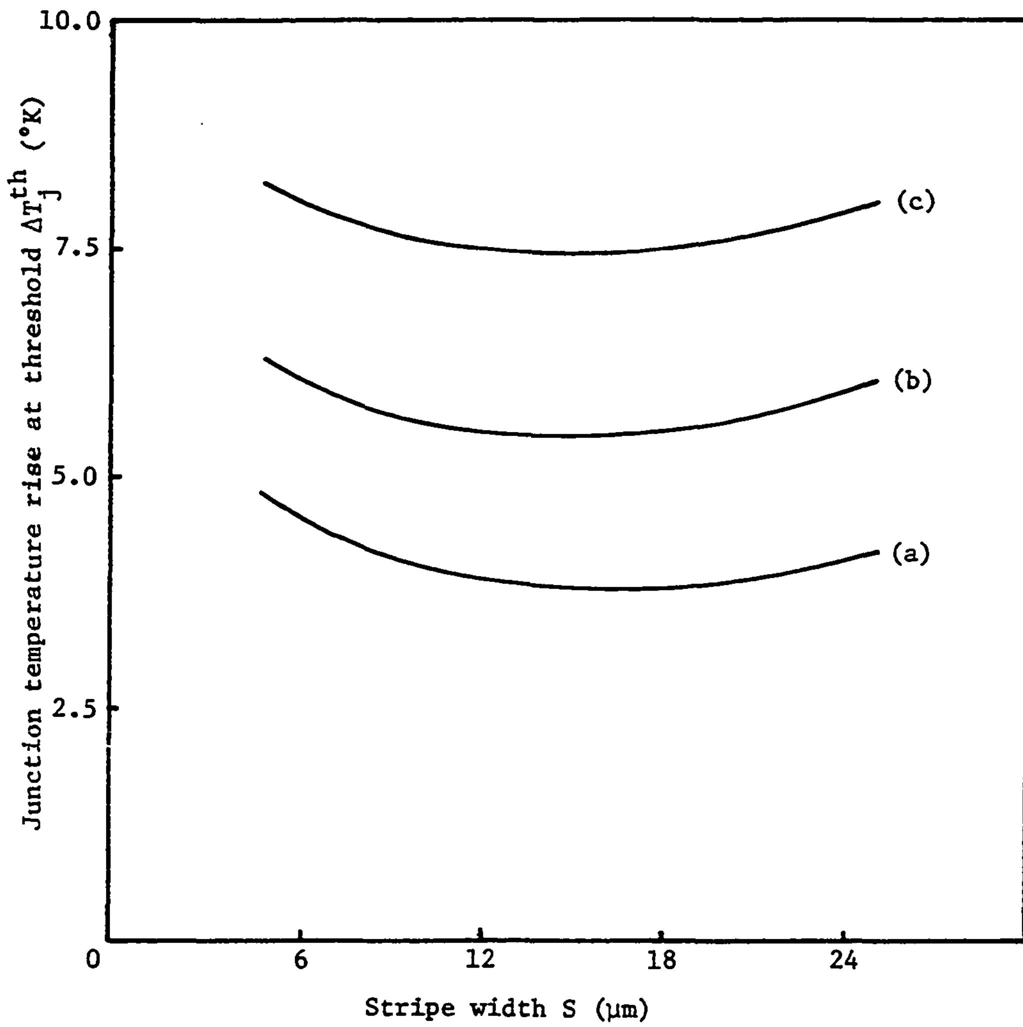

Fig. 3.19. Junction temperature rise at threshold as a function of stripe width. (a) d = 0.12 µm (b) d = 0.2 µm (c) d = 0.3 µm

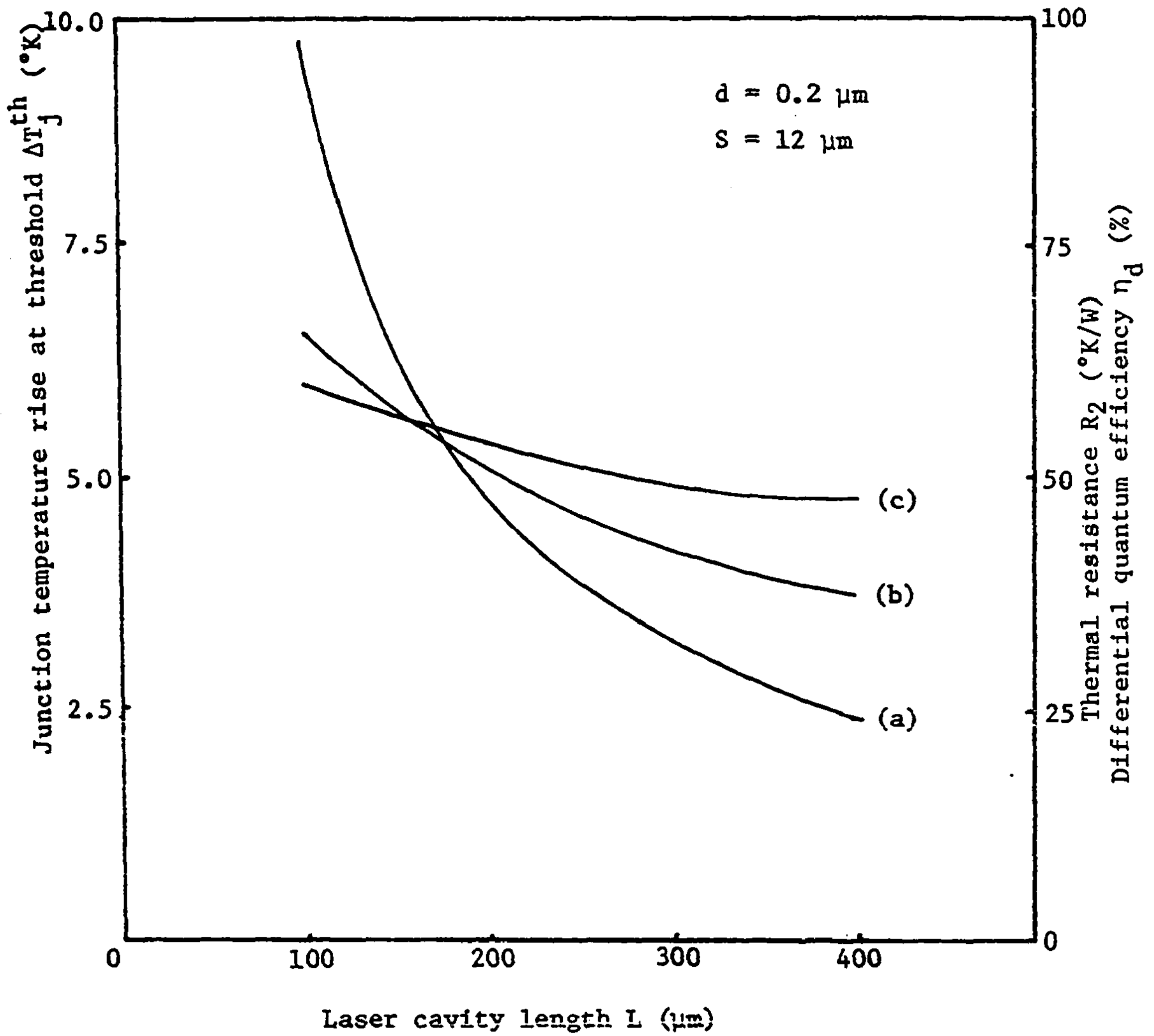

Fig. 3.20. Effect of the cavity length. (a) thermal resistance (b) differential quantum efficiency (c) junction temperature rise at threshold

where η_i is the internal quantum efficiency. Using $\alpha = 35\ cm^{-1}$, $\eta_i \simeq 0.9$, and $R = 0.3$, the differential quantum efficiency is also illustrated as a function of laser cavity length in Figure 3.20.

3. Other thermal design considerations

As indicated in Table 3.1, the results discussed so far have been confined to a proton-bombarded stripe-geometry laser with p-GaAs active layer. In this section, qualitative discussions on material aspects and other stripe-geometry features are presented.

First, the mole fraction x of AlAs for the active layer material $Al_xGa_{1-x}As$ is determined according to the desired emission wavelength. Typically, x is in the range of 0 to 0.1. Since the thermal conductivity of $Al_xGa_{1-x}As$ reduces from 0.45 to 0.19 W/cm-°K as x is increased from 0 to 0.1, junction heating is expected to increase for an active layer with higher x. According to calculations based on the present model, the increase in temperature was insignificant.

Next, consider other stripe-geometry structures such as contact-stripe or planar-stripe lasers. Normally these lasers have substantial current spreading in the lateral direction, as previously discussed in section II(A). Because of spreaded current density distribution, as illustrated in Figure 2.3, the width of the heating region in the active layer is effectively increased. As a result, the thermal gradient, as well as the gradient of electron concentration in the lateral direction, is decreased, thus reducing the thermal focusing effect for CW operation condition. Therefore, a slightly increased lateral mode size exists in these kinds of lasers in comparison to proton-bombarded stripe lasers.

Junction heating is not reduced significantly in these lasers because the threshold current is increased by spreading.

Another aspect that should be considered is the selection of heat sink material. At present, diamond (type IIa), Cu, and Si are the materials generally used for a laser diode heat sink. The thermal conductivities of these materials are 22.0, 4.0, and 1.5 W/cm-°K, respectively. Naturally, diamond offers the best performance of the listed materials [20]. To investigate the effect of thermal conductivity of the heat sink material, it is necessary to employ a more rigorous boundary condition at the heat sink boundary, instead of the ideal condition used in present model.

IV. CONCLUDING REMARKS

In the present study, the subproblems of lateral current spreading, electron concentration, thermal distribution, and waveguiding in the laser cavity were solved and incorporated into a theoretical model for stripe-geometry double-heterostructure injection lasers. To investigate the effects of temperature distribution in the laser on the performance of the device, the model was applied to conventional gain-guiding proton-bombarded stripe-geometry lasers. The effects on guided mode patterns, threshold current, and emission spectrum were quantitatively analyzed and discussed. The results are generally in good agreement with existing experimental data. Significant findings in this work include the following:

(i) Thermal gradient existing in the lateral direction for CW operation condition may result in a reduction of the guided lateral mode widths up to 20% in comparison to those for pulsed operation.

(ii) Thermal index-focusing of higher order lateral modes enhances their mode gains so that the onset of these modes is relatively favorable at lower optical power level for CW operation. It may result in a kink at a lower energy level, which is highly undesirable in many applications.

(iii) Temperature rise in the active region caused by junction heating results in an increase of threshold current and emission wavelength for CW operation in comparison to those for pulsed operation. To improve the performance of the laser at higher ambient temperature, it is necessary

to reduce thermal resistance R_2 and threshold current I_{th} so that the product $R_2 \times I_{th}$ is small. This is equivalent to minimizing the junction heating at room temperature.

(iv) An optimal structure for minimal junction heating was sought with the model. Quantitative results were obtained which pertain to reduction of junction temperature rise at threshold by reducing the thickness of layers in between the active layer and heat sink. Thin active and P-inactive layer structure was found to be most effective in reducing junction heating. The effects of cavity length and stripe width were also investigated with the model.

The model is applicable to different gain-guiding stripe-geometry lasers as well as other III-V compound material lasers such as the InGaAsP/InP device.

A. Suggestion for Further Study

It will be desirable to extend the analysis in order to investigate other aspects of thermal effects on the device characteristics. For instance, the effects on quantum noise or optical nonlinearity above threshold condition are likely subjects for future study.

Although some of the theoretical results reported in the present study are in good agreement with existing experimental data, further experimental verification is desirable. Since the direct measurement of temperature variation is not feasible, some sort of indirect measurement is required. For instance, a careful measurement of near-field width for CW and pulsed operation may lead to information

on lateral thermal gradient. Also, correlation between the device structure and maximum CW operation temperature or threshold spectrum shift may offer additional information on junction heating and thermal resistance.

V. REFERENCES

1. S. E. Miller, "Overview of Telecommunications via Optical Fibers," Proc. IEEE, 68 (1980):1173-1174.

2. N. Markoff, "Technology '82; Fiber Optics," IEEE Spectrum, 19 (Jan. 1982):39-40.

3. A. R. Goodwin, J. R. Peters, M. Pion, G. H. B. Thompson, and J. E. A. Whiteaway, "Threshold Temperature Characteristics of Double Heterostructure $Ga_{1-x}Al_xAs$ Lasers," J. Appl. Phys., 46 (Jul. 1975):3126-3131.

4. C. J. Hwang, N. B. Patel, M. A. Sacilotti, F. C. Prince, and D. J. Bull, "Threshold Behavior of (GaAl)As-GaAs Lasers at Low Temperatures," J. Appl. Phys., 49 (Jan. 1978):29-34.

5. M. Asada, A. R. Adams, K. E. Stubkjaer, Y. Suematsu, Y. Itaya, and J. V. Collins, "The Temperature Dependence of the Threshold Current of GaInAsP/InP Double-Heterostructure Lasers," IEEE J. Quantum Electron., QE-17 (May 1981):611-619.

6. T. Hayakawa, S. Yamamoto, H. Nayashi, T. Sakurai, and T. Hijikata, "Temperature Dependence of Threshold Current in (GaAl)As Double-Heterostructure Lasers with Emission Wavelengths of 0.74-0.9 μm," IEEE J. Quantum Electron., QE-17 (Nov. 1981):2205-2210.

7. R. L. Hartman and R. W. Dixon, "Reliability of DH GaAs Lasers at Elevated Temperatures," Appl. Phys. Lett., 26 (1975):239-241.

8. S. Ritchie, R. F. Godfrey, B. Wakefield, and D. H. Newman, "The Temperature Dependence of Degradation Mechanisms in Long-Lived (GaAl)As DH Lasers," J. Appl. Phys., 49 (June 1978):3127-3132.

9. W. B. Joyce and R. W. Dixon, "Thermal Resistance of Heterostructure Lasers," J. Appl. Phys., 46 (1975):855-862.

10. T. Kobayashi and Y. Furukawa, "Temperature Distribution in the GaAs-AlGaAs Double-Heterostructure Laser Below and Above the Threshold Current," Jpn. J. of Appl. Phys., 14 (1975):1981-1986.

11. T. Kobayashi and G. Iwane, "Three Dimensional Thermal Problems of Double-Heterostructure Semiconductor Laser," Jpn. J. of Appl. Phys., 16 (1977):1403-1408.

12. D. H. Newman, D. J. Bond, and J. Stefani, "Thermal-Resistance Models for Proton-Isolated Double-Heterostructure Lasers," Solid-State and Electron Devices, 2 (1978):41-46.

13. E. Duda, J. C. Carballes, and J. Apruzzese, "Thermal Resistance and Temperature Distribution in Double-Heterostructure Lasers: Calculations and Experimental Results," IEEE J. Quantum Electron., QE-15 (1979):812-817.

14. C. H. Gooch, "The Thermal Properties of Gallium Ansenide Laser Structure," IEEE J. Quantum Electron., QE-4 (Apr. 1968):140-143.

15. T. L. Paoli, "A New Technique for Measuring the Thermal Impedance of Junction Lasers," IEEE J. Quantum Electron., QE-11 (July 1975): 498-503.

16. J. P. van der Ziel, "Spectral Broadening of Pulsating $Al_xGa_{1-x}As$ Double Heterostructure Lasers," IEEE J. Quantum Electron., QE-15 (Nov. 1979):1277-1281.

17. S. E. H. Turley, G. H. B. Thompson, and D. F. Lovelace, "The Dielectric Constant of an Inbuilt Waveguide in Twin-Transverse-Junction Stripe Lasers," Electronics Letters, 15 (Apr. 1979): 256-257.

18. H. Meixner and R. Unger, "Optical Method for Determination of the Thermal Resistivity of Laser Diodes," Siemens Forsch.-u. Entwickl.-Ber., 3 (1974):190-194.

19. S. Ritchie, "Thermal Properties of Semiconductor Lasers and the Interpretation of Thermal-Resistance Measurements," Solid State and Electron Devices, 3 (Nov. 1979):201-205.

20. H. Yonezu, T. Yuasa, T. Shinohara, T. Kamejima, and I. Sakuma, "CW Optical Power from (AlGa)As Double Heterostructure Lasers," Jpn. J. Appl. Phys., 15 (Dec. 1976):2393-2401.

21. P. Garel-Jones and J. C. Dyment, "Calculations of the Continuous-Wave Lasing Range and Light-Output Power for Double-Heterostructure Lasers," IEEE J. Quantum Electron., QE-11 (Jul. 1975):408-413.

22. M. Yano, H. Imai, K.-I. Honi, and M. Takusagawa, "High Temperature Characteristics of Stripe-Geometry InGaAsP/InP Double-Heterostructure Lasers," IEEE J. Quantum Electron., QE-17 (May 1981):619-626.

23. N. G. Basov, O. N. Krokhin, and Y. M. Posov, "Production of Negative-Temperature States in p-n Junctions of Degenerate Semiconductors," Sov. Phys.-JETP, 13 (1961):1320-1321.

24. R. N. Hall, G. E. Fenner, J. D. Kingsley, T. J. Soltys, and R. O. Carlson, "Coherent Light Emission from GaAs Junctions," Phys. Rev. Lett., 9 (1972):366-368.

25. M. I. Nathan, W. P. Dumke, G. Burns, F. H. Dill and G. J. Lasher, "Stimulated Emission of Radiation from GaAs p-n Junctions," Appl. Phys. Lett., 1 (1962):62-64.

26. N. Holonyak, Jr. and S. F. Bevacqua, "Coherent (Visible) Light Emission from $Ga(As_{1-x}P_x)$ Junctions," Appl. Phys. Lett., 1 (1962): 82-83.

27. M. B. Panish, "Heterostructure Injection Laser," Proc. of IEEE, 64 (1976):1512-1540.

28. M. K. Barnoski (Editor), Fundamentals of Optical Fiber Communications, New York: Academic Press Inc., 1976.

29. H. Kressel and J. K. Butler, Semiconductor Lasers and Heterojunction LEDs, New York: Academic Press Inc., 1977.

30. H. C. Casey, Jr., "Room-Temperature Threshold-Current Dependence of $GaAs-Al_xGa_{1-x}As$ DH Lasers on x and Active Layer Thickness," J. Appl. Phys., 49 (1978):3684-3692.

31. B. W. Hakki, "Mode Gain and Junction Current in GaAs Under Lasing Conditions," J. Appl. Phys., 45 (1974):288-294.

32. H. Kroemer, "A Proposed Class of Heterojunction Injection Lasers," Proc. IEEE (corresp.), 51 (1963):1782-1783.

33. I. Hayashi, M. B. Panish, and P. W. Foy, "A Low-Threshold Room Temperature Injection Laser," IEEE J. Quantum Electron. (corresp.), QE-5 (1969):211-212.

34. M. B. Panish, I. Hayashi and S. Sumski, "A Technique for the Preparation of Low-Threshold Room-Temperature GaAs Laser Diode Structures," IEEE J. Quantum Electron. (corresp.), QE-5 (1969):210-211.

35. H. Kressel and H. Nelson, "Close Confinement GaAs PN Junction Lasers with Reduced Optical Loss at Room Temperature," RCA Rev., 30 (1969):106-113.

36. I. Hayashi, M. B. Panish, P. W. Foy and S. Sumski, "Junction Lasers which Operate Continuously at Room Temperature," Appl. Phys. Lett., 17 (1970):109-111.

37. H. C. Casey, Jr. and M. B. Panish, "Composition Dependence of the $Ga_{1-x}Al_xAs$ Direct and Indirect Energy Gaps," J. Appl. Phys., 40 (1969):4910-4912.

38. Special Issue on Quaternary Compound Semiconductor Materials and Devices--Sources and Detectors, IEEE J. Quantum Electron., QE-17 (Feb. 1981):117-288.

39. H. C. Casey, Jr. and M. B. Panish, Heterostructure Lasers, Vol. B, New York: Academic Press Inc., 1978.

40. G. H. B. Thompson, Physics of Semiconductor Laser Devices, New York: John Wiley and Sons, Ltd., 1980.

41. J. C. Dyment, L. A. D'Asaro, J. C. North, B. I. Miller, and J. E. Ripper, "Proton-Bombardment Formation of Stripe-Geometry Heterostructure Lasers for 300°K CW Operation," Proc. IEEE, 60 (June 1972): 726-728.

42. J. M. Blum, J. C. McGroddy, P. G. McMullin, K. K. Shih, A. W. Smith, and J. F. Ziegler, "Oxygen-Implanted Double-Heterojunction GaAs/GaAlAs Injection Lasers," IEEE J. Quantum Electron., QE-11 (July 1975):413-418.

43. J. C. Dyment, "Hermite-Gaussian Mode Patterns in GaAs Junction Lasers," Appl. Phys. Lett., 10 (Feb. 1967):84-86.

44. T. Tsukada, "GaAs-$Ga_{1-x}Al_xAs$ Buried Heterostructure Injection Lasers," J. Appl. Phys., 45 (1974):4899-4906.

45. R. D. Burnham and D. R. Scifres, "Etched Buried Heterostructure GaAs/$Ga_{1-x}Al_xAs$ Injection Lasers," Appl. Phys. Lett., 27 (1975): 510-511.

46. H. Yonezu, Y. Matsumoto, T. Shinohara, I. Sakuma, T. Suzuki, K. Kobayashi, R. Lang, Y. Nannichi, and I. Hayashi, "New Stripe Geometry Laser with High Quality Lasing Characteristics by Horizontal Mode Stabilization--A Refractive Index Guiding with Zn Doping," Jpn. J. Appl. Phys., 16 (1977):209-210.

47. P. A. Kirkby and G. H. B. Thompson, "Channeled Substrate Buried Heterostructure GaAs-(GaAl)As Injection Lasers," J. Appl. Phys., 47 (1976):4578-4589.

48. R. W. Dixon, "Current Directions in GaAs Laser Device Development," Bell Sys. Tech. J., 59 (May 1980):669-722.

49. D. Marcuse, Theory of Dielectric Optical Waveguide, New York: Academic Press Inc., 1974.

50. H. Yonezu, I. Sakuma, K. Kobayashi, T. Kamejima, M. Veno, and Y. Nannichi, "A GaAs-$Al_xGa_{1-x}As$ Double Heterostructure Planar Stripe Laser," Jpn. J. Appl. Phys., 12 (Oct. 1973):1585-1592.

51. J. E. Pankove, Optical Processes in Semiconductors, Englewood Cliffs, N. J.: Prentice-Hall, Inc., 1971.

52. M. Ito and T. Kimura, "Stationary and Transient Thermal Properties of Semiconductor Laser Diodes," IEEE J. Quantum Electron., QE-19 (May 1981):787-795.

53. W. T. Tsang, "The Effect of Lateral Current Spreading, Carrier Out-Diffusion, and Optical Mode Losses on the Threshold Current Density of GaAs-$Al_xGa_{1-x}As$ Stripe-Geometry DH Lasers," J. Appl. Phys., 49 (Mar. 1978):1031-1044.

54. H. C. Hsieh and G. Y. Lee, "Magnetostatic Field Effect on Threshold Current in a GaAs/$Al_yGa_{1-y}As$ Double-Heterostructure Laser," J. Appl. Phys., 52 (July 1981):4414-4417.

55. A. van der Ziel, Solid State Physical Electronics, 3rd Ed., Englewood Cliffs, N.J.: Prentice Hall, Inc., 1976.

56. R. F. Harrington, Time Harmonic Electromagnetic Fields, New York: McGraw-Hill, 1961.

57. S. Ramo, J. R. Whinnery and T. Van Duzer, Fields and Waves in Communication Electronics, New York: John Wiley and Sons, Inc., 1965.

58. T. Ikegami, "Reflectivity of Mode at Facet and Oscillation Modes in Double Heterostructure Injection Lasers," IEEE J. Quantum Electron., QE-8 (June 1972):470-476.

59. N. Chinone, "Nonlinearity in Power-Output-Current Characteristics of Stripe-Geometry Injection Laser," J. Appl. Phys., 48 (Aug. 1977): 3237-3243.

60. B. W. Hakki, "Carrier and Gain Spatial Profiles in GaAs Stripe Geometry Lasers," J. Appl. Phys., 44 (1973):5021-5028.

61. T. Paoli, "Waveguiding in a Stripe-Geometry Junction Laser," IEEE J. Quantum Electron., QE-13 (Aug. 1977):662-668.

62. J. Buus, "Detailed Field Model for DH Stripe Lasers," Opt. Quantum Electronics, 10 (1978):459-474.

63. M. R. Mathews, R. B. Dyott, and W. P. Carling, "Filaments as Optical Waveguides in Gallium-Arsenide Lasers," Electron. Lett., 8 (1972):570-572.

64. P. R. Selway, G. H. B. Thompson, G. D. Henshall, and J. E. A. Whiteaway," Measurement of the Effect of Injected Carriers on the p-n Refractive Index Step in Single Heterostructure Lasers," Electron. Lett., 10 (1974):453-455.

65. B. W. Hakki, "Striped GaAs Lasers: Mode Size and Efficiency," J. Appl. Phys., 46 (June 1975):2723-2730.

66. D. T. F. Marple, "Refractive Index of GaAs," J. Appl. Phys., 35 (1964):1241-1242.

67. D. D. Cook and F. R. Nash, "Gain-Induced Guiding and Astigmatic Output Beam of GaAs Lasers," J. Appl. Phys., 46 (Apr. 1975):1660-1672.

68. J. K. Butler and J. B. Delaney, "Field Solutions for the Lateral Modes of Stripe Geometry Injection Lasers," IEEE J. Quantum Electron., QE-16 (Dec. 1980):1326-1328.

69. J. K. Butler and J. B. Delaney, "A Rigorous Boundary Value Solution for the Lateral Modes of Stripe Geometry Injection Lasers," IEEE J. Quantum Electron., QE-14 (July 1978):507-513.

70. H. C. Casey, Jr. and M. B. Panish, Heterostructure Lasers, Vol. A, New York: Academic Press, 1978.

71. A. Yariv, Quantum Electronics, 2nd Ed., New York: John Wiley and Sons, Inc., 1975.

72. S. Gasiorowicz, Quantum Physics, New York: John Wiley and Sons, Inc., 1974.

73. S. M. Sze, Physics of Semiconductor Devices, New York: John Wiley and Sons, Inc., 1969.

74. P. A. Kirkby, A. R. Goodwin, G. H. B. Thompson, and P. R. Selway, "Observation of Self-Focusing in Stripe Geometry Semiconductor Lasers and the Development of a Comprehensive Model of Their Operation," IEEE J. Quantum Electron., QE-13 (Aug. 1977):705-719.

75. J. Buus, "A Model for the Static Properties of DH Lasers," IEEE J. Quantum Electron., QE-15 (Aug. 1979):734-739.

76. P. M. Asbeck, D. A. Commack, J. J. Daniele, and V. Klebanoff, "Lateral Mode Behavior in Narrow Stripe Lasers," IEEE J. Quantum Electron., QE-15 (Aug. 1979):727-733.

77. J. R. Biard, W. N. Carr and B. S. Reed, "Analysis of a GaAs Laser," Trans. AIME, 230 (1964):286-290.

VI. ACKNOWLEDGMENTS

The author would like to express sincere appreciation to Professor H. C. Hsieh for his guidance and encouragement throughout this work. Thanks are also offered to Dr. J. O. Kopplin, Chairman of the Department of Electrical Engineering, Iowa State University, for financial support during this study.

Finally, the author would especially like to thank his family members for their continuous support and understanding.

VII. APPENDIX

A. Solution for Current Spreading

Equation (2.2) is solved with the formalism used by Yonezu et al. [50]. Voltage drop in the p-GaAs capping layer and the P-AlGaAs inactive layer $-dV_x$ is

$$-dV_x = \left(\frac{d_5}{\rho_5} + \frac{d_6}{\rho_6}\right)^{-1} \frac{1}{L} I_x \, dx \qquad (7.1)$$

where ρ_5, ρ_6, d_5, and d_6 are the sheet resistances and layer thicknesses for the p- and P-layers. For convenience, $R_s = (d_5/\rho_5 + d_6/\rho_6)^{-1}$ is used.

In the condition of $\exp(\beta V_x) \gg 1$, (2.2) and (7.1) combined into

$$\frac{d^2 I_x}{dx^2} = -(\beta R_s/L)\, I_x \frac{dI_x}{dx} \qquad (7.2)$$

The solution of (7.2) is, with $I_x(S/2) = I_o$,

$$I_x = \frac{I_o}{1 + \dfrac{|x| - S/2}{\ell_o}} \qquad \text{for } |x| \geq S/2 \qquad (7.3)$$

where

$$\ell_o = 2L/\beta R_s I_o \qquad (2.7a)$$

Current across the N-p junction between x and x + Δx, $\Delta I_y(x)$ is obtained from (7.3):

$$\Delta I_y(x) = \frac{I_o}{\ell_o\left(1 + \frac{|x| - S/2}{\ell_o}\right)^2}\Delta x \qquad \text{for } |x| \geq S/2 \qquad (7.4)$$

Given the assumption that $I_y(S/2) = I_e$ with the stripe width S,

$$I_e = \frac{\beta R_s\, I_o^{\,2} S}{2L} \qquad (7.5)$$

or

$$I_o = (2LI_e/\beta R_s S)^{1/2} \qquad (2.3)$$

Substituting (7.5) into (2.1) yields

$$\frac{\beta R_s I_o^{\,2} S}{2L} + 2I_o - I = 0 \qquad (7.6)$$

Therefore, if the total current I is known, I_o and I_e can be obtained from (7.5) and (7.6). For the outside stripe region, current density across the junction $J_y(x)$ is, from (7.4),

$$J_y(x) = \frac{I_o}{\ell_o L}\left(1 + \frac{|x| - S/2}{\ell_o}\right)^{-2} \qquad \text{for } |x| \geq S/2 \qquad (2.6)$$

B. Ambipolar Diffusion Constant

The ambipolar diffusion constant D_a is expressed as [55]

$$D_a = \frac{D_n D_p (p + n)}{D_n n + D_p p} \qquad (7.7)$$

for $p \simeq n$

$$D_a \simeq \frac{2D_n D_p}{D_n + D_p} \tag{7.8}$$

Since $D_n >> D_p$, (7.8) reduces to

$$D_a \simeq 2D_p \tag{2.10}$$

C. Hermite-Gaussian Solution

The solution to the wave equation (2.127) is known as Hermite-Gaussian functions [71].

For convenience, substitute

$$E = [k_o^2 \ \varepsilon_{eff}(0) - \beta_y^2 - \beta_z^2]/\delta^2 \tag{7.9}$$

$$\delta^2 = k_o \ a_{eff} \tag{7.10}$$

and change the variable with $\xi = \delta x$ in (2.127) to reduce the equation to

$$\frac{d^2\psi(\xi)}{d\xi^2} + (E - \xi^2)\ \psi(\xi) = 0 \tag{7.11}$$

For $\xi^2 >> E$ the behavior of ψ is dominated by the term

$$\exp(-1/2\ \xi^2),$$

so that it is possible to assume a solution of the form

$$\psi(\xi) = H(\xi) \exp(-1/2\ \xi^2) \tag{7.12}$$

where H(x) is a polynomial of a finite order.

Substituting $\psi(x)$ from (7.12) in (7.11) leads to the equation

$$\frac{d^2H(\xi)}{d\xi^2} - 2\frac{dH(\xi)}{d\xi} + (E - 1)\ H(\xi) = 0 \tag{7.13}$$

It is well-known that the eigenvalues of the equation (7.13) are

$$E = 2n + 1 \tag{7.14}$$

where n is 0, 1, 2, 3... . Putting (7.14), the differential equation for the polynomials $H_n(\xi)$, which are known as the Hermite polynomials, becomes

$$\frac{d^2H_n}{d\xi^2} - 2\xi\frac{dH_n}{d\xi} + 2n\ H_n = 0 \tag{7.15}$$

These polynomials are conveniently derived by means of the power series expansion of the function $e^{-s^2+2s\xi}$ according to

$$G(\xi,s) = e^{\xi^2-(s-\xi)^2} = e^{-s^2+2s\xi} = \sum_{n=0}^{\infty} \frac{H_n(\xi)}{n!}\ s^n \tag{7.16}$$

To generate the Hermite polynomials we use that, according to (7.16), use

$$H_n(\xi) = \frac{\partial^n}{\partial s^n}\ [e^{\xi^2-(s-\xi)^2}]\Big|_{s=0}$$

$$= e^{\xi^2} (-1)^n \frac{d^n}{d\xi^n} e^{-\xi^2} \qquad (2.129)$$

Therefore, the eignefunctions (7.12) become

$$\psi_n(\xi) = H_n(\xi) \exp(-1/2\ \xi^2) \qquad (7.17)$$

or

$$\psi_n(x) = H_n(k_o^{1/2}\ a_{eff}^{1/2}\ x) \exp(-1/2\ k_o\ a_{eff}\ x^2) \qquad (2.128)$$